UNIVERSITÉ DU LUXEMBOURG

PhD-FSTM-2023-070
The Faculty of Science, Technology and Medicine

DISSERTATION

Defence held on 03/07/2023 in Esch-sur-Alzette

to obtain the degree of

DOCTEUR DE L'UNIVERSITÉ DU LUXEMBOURG

EN PHYSIQUE

by

Christina HILL
Born on 01 June 1987 in Trier (Germany)

RESONANT RAMAN SCATTERING AND OTHER NEW COUPLING PHENOMENA IN FERROELASTIC $BiVO_4$

Dissertation defence committee

Prof. Dr. Susanne Siebentritt, Chairman
Professor, Université du Luxembourg, Esch-sur-Alzette, Luxembourg

Prof. Dr. Marin Alexe, Vice Chairman
Professor, University of Warwick, Coventry, UK

Dr. Marie-Aude Méasson
Senior Researcher, Institute Néel, Grenoble, France

Dr. Sven Reichardt
Senior Researcher, Université du Luxembourg, Esch-sur-Alzette, Luxembourg

Prof. Dr. Mael Guennou, dissertation supervisor
Professor, Université du Luxembourg, Esch-sur-Alzette, Luxembourg

DECLARATION

I hereby confirm that the PhD thesis entitled "*Resonant Raman scattering and other new coupling phenomena in ferroelastic $BiVO_4$*" has been written independently and without any other sources than cited.

Luxembourg, _____

Christina Hill

ABSTRACT

With the introduction of ferroic oxides into the research field of photovoltaic and photocatalytic applications, an increasing interest in understanding the coupling mechanisms of light with the electronic bands in this class of materials has been developed over the last years. In many of these examples, reliable band structure calculations are not yet available mostly because of the complexity in the crystal structure which demands for many experimental evidences to verify even basic characteristics of the structure. Also classical experimental techniques based on the optical absorption seem to reach their limits here resulting often in controversial publications on the nature of the band gap.

The goal of this work is to exploit resonant Raman scattering to reveal information on the electronic band structure and thereby create a better understanding of the light-matter coupling mechanisms in ferroic oxides. As a model material, we choose to work on ferroelastic bismuth vanadate $BiVO_4$, which is known for its second-order phase transition from the high-symmetry tetragonal to the low-symmetry monoclinic phase.

On the way to understand resonant Raman scattering in $BiVO_4$, i.e. the coupling of lattice vibrations and electronic transitions, we extensively studied the phonons and optical properties and discovered new coupling phenomena of various kinds. We found a phonon-phonon coupling in the lattice vibrations of the VO_4 tetrahedron that are strongly temperature and polarization dependent. The coupling strength is of opposite sign depending on the polarization conditions and diminishes at the structural phase transition at which one of the phonon modes changes its symmetry.

Additionally, the transmission data evidence the coupling between the spontaneous shear strain and the electronic structure that primarily defines the strong temperature dependence of the optical absorption in monoclinic $BiVO_4$.

Further, we report on resonant Raman scattering effects that allow us to study the coupling between phonons and electrons. We succeeded to measure multiple resonant Raman bands corresponding to not only the band gap at 2.4 eV but also to a polaronic defect level at 2.0 eV. The coupling strength to the electronic states in the conduction band and in the defect level varies between the Raman modes corresponding to different lattice vibrations. By varying the light polarization in the experiment, we could access another band-to-band transition that lies 120 meV above the band gap energy. This energy difference matches the optical anisotropy quantified by transmission measurements. With this work we demonstrate that resonant Raman spectroscopy is a very powerful tool to study not only structural but also electronic properties in ferroic oxides. It has the potential to go deeper in the

analysis on the electronic band structure than classical techniques such as UV/Vis spectroscopy or ellipsometry.

ACKNOWLEDGMENTS

After my university studies of electrical engineering and material sciences, I decided to work in the industry as an engineer. During those years, I felt the increasing desire to return to university and to conduct a PhD research. Today, I am very grateful to everyone that supported me in the decision to finally realize my dream.

In Luxembourg, I found a research environment for my PhD that not only addresses my strong interest in electronics and material sciences, but that is also located close to my home-town and family. Within the last 5 years that I spent on my research work, I had the privilege to work with many excellent colleagues that have become very good friends. To those people I want to express my deep gratitude. In particular would like to address the following persons:

- Prof. Dr. Mael Guennou - thank you very much for your very good and reliable supervision and guidance, for your critical and constructive feedback. I profited immensely from your detailed knowledge and expertise. Thank your for making time for many in-depth discussion, especially in crucial moments when a deadline was approaching. It was a great pleasure to work with you and to discover Raman scattering and the beauty of working with single crystals.

- Dr. Emmanuel Defay - thank your for giving me the opportunity to perform this work in your research group *Ferroic Materials for Transducers* at LIST. Thank you for all your trust and support especially when I decided to take parental leave which required organisational and convincing work not only towards the funding partners.

- Prof. Dr. Susanne Siebentritt - thank you for being president of the thesis committee, but also for following the progress of the work over the full time as a member of the CET and as coordinator of the FNR funding project *Massena*. Thank your for your critical and constructive feedback and for all the in-depth discussions.

- Prof. Dr. Marin Alexe - thank you for being member of the thesis committee, for your guidance over the full time as member of the CET, for giving constructive inputs and raising important questions about the work. Your positive feedback and attitude during the CET meetings have always been very motivating to me.

- Dr. Marie-Aude Méasson and Dr. Sven Reichardt - thank you for being members of the thesis committee and acting as external reviewers. Thank you for the thorough reading of my manuscript and your interest in my research work.

- Dr. Georgy Gordeev - I would like to especially thank you for your help and encouragement to publish the work on the phonon-phonon coupling story. Thank you for your guidance and for sharing your expertise on resonant Raman scattering with me.

- Dr. Constance Toulouse - Thank you for all your guidance and assistance in performing non-standard experiments and for always making time to answer any experimental and theoretical questions, also per Whatsapp if needed. Thank you for staying with me at the laboratory at late hours, especially for all the low-temperatures measurements that we performed together.

- Naveen Aruchamy, Alvar Torello Massana, Cosme Milesi-Brault, Sangita Dutta, Youri Nouchokgwe and all my colleagues from LIST - Thank you for making the time of my PhD research such a great and positive experience. I am very grateful for all the good moments that we spend together not only at conferences but also during many coffee and lunch breaks.

- Pranab Biswas, Mohamad Baker Shoker, Angelina Gudima and all my colleagues from the University - Thank you for the fantastic time that we spend together and for creating such an open and supportive working environment.

- My family - I would like to thank my parents Hildegard and Goswin and my parents-in-law Elfie and Joa that supported me not only in very practical aspects but also gave me emotional support. Thank you to my brothers Andreas and Michael that inspired me to become an engineer and motivated me throughout my whole career.

- My son Clemens and my husband Andi - Thank you for all your love and encouragement. I especially would like to thank you for joining me for two research trips to Berlin, Germany and Villigen in Switzerland. Without your support and willingness to travel with me, these research trips would have been less enjoyable.

Finally, I would like to acknowledge the Fond National de Recherche Luxembourg for their financial support in the frame work of the project PRIDE/15/10935404.

CONTENTS

LIST OF FIGURES

LIST OF TABLES

Part I

THESIS

1 INTRODUCTION

Raman scattering is typically used to study lattice vibrations and lattice dynamics in crystalline semiconducting materials. The characteristic phonon energy and lifetime is independent of the laser energy used for the excitation. However, Raman scattering also contains information on the electronic band structure and the density of states [115]. This information becomes accessible if the laser energy matches the energy of an optically allowed electronic transition in the material. In this case, the scattering efficiency is enhanced and we refer to resonant Raman scattering. The resonant Raman intensity is further enhanced if there is a large density of electronic states available for the optical transition [115].

THE RESONANT RAMAN EFFECTS have been intensively studied for classical diamond and zinc-blende type semiconductors mostly in the 70s. The research group around M. Cardona published several investigations on resonances in the first- and second-order Raman scattering for Germanium [18, 77], Silicon [76], GaP [111], ZnO [15] and GaAs [102]. The crystallographic structure of this class of materials is rather simple so that band structure calculations have been available in many cases. In most of these examples the resonant Raman studies have been published together with a band structure diagram and therefore a direct assignment of the resonant Raman peaks to the electronic transitions was possible. The observed enhancement of the Raman intensity can be several orders of magnitude if a direct electronic transition is involved in the process.

Later, resonant Raman spectroscopy became very popular in the research field of low-dimensional materials. In carbon nanotubes resonant Raman scattering was exploited to reveal characteristic properties such as tube diameter and transition energy [74] or to distinguish metallic from semiconducting nanotubes [14, 72]. Another example is the work of Klar and co-authors on graphene in which they showed that the resonant Raman behaviour depends on the number of layers [56]. The two publications from Ketterer [55] and Kusch [57] on zinc-blende and wurtzite GaAs nanowires nicely demonstrated that resonant Raman scattering contains detailed information on the band structure and on the symmetry of the valence and conduction bands.

However, the transfer to semiconducting oxides has not been done yet. In the literature, there are only a limited number of publications on resonant Raman scattering in oxides. One example is the work of Andreasson et al. from 2007 [5, 6], in which the authors observed resonances in the higher-order Raman scattering of the disordered perovskite oxides $LaFe_{1-x}Cr_xO_3$. In this report, a charge transfer from iron to the chromium ion changes locally the crystal structure and consequently activates an oxygen breathing

mode of A_g symmetry. The strong intensity enhancement at 2.4 eV in the higher-order Raman scattering of this mode is then explained by the Franck Condon mechanism. In 2009, Andreasson and co-workers extended their resonant Raman study to the UV wavelengths and discovered additional resonances caused by charge transfer from the oxygen to the iron ion [6]. In this publication, they match the two resonant peaks with two broad optical absorption bands in the visible and in the UV light range.

Another example is the work of de la Flor et al. [38] on Pb-based perovskite-type relaxor compounds. They observed simultaneous enhancement of the first- and second-order Raman scattering slightly above the band gap energy that is strongly temperature dependent. Another more recent example is the work of Weber et al. [110], in which resonant Raman spectroscopy was explored to study electronic transitions in bismuth ferrite in the first- and second-order Raman scattering. From temperature dependent measurements, the authors could assign the resonance effects to a direct, an indirect and an in-gap electronic transition. However, this work is lacking a complete interpretation of the resonances. The assignment to particular electronic bands is not shown, most likely because of the complex electronic band structure in the case of bismuth ferrite.

BISMUTH VANADATE $BiVO_4$ has been chosen for this research work as a representative of the semiconducting oxide family.

$BiVO_4$ has three common crystal forms; the zircon structure with tetragonal symmetry and two scheelite structures with monoclinic and tetragonal structure [26, 100]. Their stability depends on the synthesis method.[100] Only the monoclinic scheelite $BiVO_4$ possesses optical properties that are suitable for the application in photocatalytic devices [116]. The scheelite structure of $BiVO_4$ exhibits a reversible second-order ferroelastic phase transition at $T_c = 523 \pm 5$ K from a high-temperature tetragonal symmetry (space group $I4_1/a$) to a low-temperature monoclinic symmetry (space group I2/a - C2/c(15) in the standard setting) [10, 29, 71, 92]. In the high-temperature tetragonal phase, the unit cell exhibits a four-fold rotational axis along the [001]-axis that is referred to as principal axis. At the phase transition, a spontaneous shear strain develops in the plane perpendicular to the principal axis that results in a small distortion of the unit cell and reduces the crystal symmetry from tetragonal to monoclinic [9, 27, 28, 32, 45, 113].

The phase transition is driven by a soft acoustic phonon that has been very well characterized by Brillouin spectroscopy [7, 9]. It is also known for a long time that the transition comes with significant softening of the optical mode. The "soft" Raman mode was measured very early in the 1970s [73]. The Raman active modes are known from standard symmetry analysis and they have been successfully assigned [7, 71]. Their frequency shifts with temperature and pressure across the phase transition are known [71].

The ferroelastic domains form at the transition with the emergence of spontaneous strain. The domain boundaries thereby maintain the strain compatibility between neighboring domains. As a result of the structural phase

transition, there are two possible domain types in $BiVO_4$ which are rotated by 90° about the principal axis [31, 114]. The domain wall is parallel to the principal axis. The formation of domains in $BiVO_4$ is temperature dependent and completely reversible. At increasing temperatures, the ferroelastic domains get finer and finer until the domain structure disappears at the phase transition [31].

THE ELECTRONIC AND OPTICAL PROPERTIES of scheelite $BiVO_4$ have recently attracted attention with its introduction in the research field of photocatalysis. While the ferroelastic properties are well understood, the electronic and optical properties are still under discussion. There is agreement on the value of the band gap, around 2.5 eV, but the publications on the nature of the band gap are controversial. On the one hand, the band gap has been classified to be direct by several experimental works [63, 96, 118]. On the other hand, most density functional theory (DFT) studies conclude that the nature of the band gap must be indirect and predict a direct transition just a few hundreds of meV above the indirect band gap [26, 117]. This scenario is difficult to verify by traditional optical methods, such as UV/Vis spectroscopy or ellipsometry. Only recently, Cooper et al. [24] succeeded to show experimentally by resonant inelastic X-ray scattering that the fundamental band gap is indeed indirect and that there is a direct band-to-band transition only 200 meV above it. In addition, strong changes in color with varying temperature have been reported in early single crystal studies, which implies a strong temperature dependence of the optical absorption edge [30]. The exact temperature trends of the direct and indirect band edges are unknown and a comparison of experimental room-temperature data with 0 K-DFT calculations must therefore be treated carefully. Further, strong dichroism is expected because of the monoclinic crystal structure and has been indeed predicted by several groups through DFT calculations [26, 34, 117]. Finally, because of the relatively large band edge energy, intrinsic defects are expected and have been experimentally observed by Cooper et al. [25] through photoluminescence measurements. The nature and the formation mechanism of the intrinsic and impurity defects in $BiVO_4$ are still debated in the literature. Because defects play an important role in the conductivity [81, 83], a better understanding is key to further improve the charge transport and therefore the device performance for photocatalytic applications.

1.1 RESEARCH OBJECTIVES

The goal of this research work is to develop an understanding of resonant Raman effects in ferroic oxides. Raman scattering not only contains information on the lattice vibrations but also information on the electronic band structure and on the density of states in the material. The ultimate goal of this work is to extract this information and use resonant Raman scattering as a technique to probe electronic transitions. We chose to work on $BiVO_4$ for

several reasons. First of all, the band gap energy of $BiVO_4$ lies in the visible and is therefore energetically accessible in Raman spectroscopy in which laser energies in the infrared, in the visible, and up to the high UV are used. Second, the Raman spectrum is very well studied; the Raman modes and their frequencies and symmetries are known. The temperature and pressure dependence across the phase transition is characterized. The existing knowledge on the lattice vibrations in $BiVO_4$ provided us with a good basis to start our investigations. In addition, there is an increasing scientific interests in $BiVO_4$ because the material is proposed as a light absorber for photocatalytic applications [1, 13, 21, 43]. With our findings, we would like to contribute to a better understanding of the fundamental electronic properties of $BiVO_4$, which could be of great importance for the research activities with the goal to optimize $BiVO_4$ for photocatalytic applications.

***Research question 1**: Is the current understanding of the Raman spectrum sufficient to describe intensity variations by resonant Raman effects in $BiVO_4$?*

When we started our investigation, we discovered anomalies in the Raman spectrum of bismuth vanadate that have not been reported in the literature. From these observations, we wondered whether the Raman signal is really that well understood and whether the standard techniques are sufficient to extract information such as phonon frequencies or Raman cross section from the Raman signal.

***Research question 2**: What are the critical parameters in a resonant Raman experiment?*

The second research question that we tackled, was whether we observe resonant Raman effects at all in $BiVO_4$. For this we had to first identify a systematic approach to quantify these effects. In the literature, we found many examples on classical semiconductors and more recently on 2D materials. In all these examples the principle idea is the following, starting with an laser energy below the band gap, the laser energy is stepwise increased while measuring the Raman signal until resonance is achieved and the Raman signal is significantly enhanced. We questioned whether this approach is directly transferable to semiconductor oxides that exhibit much more complexity in the crystal structure. In classical semiconductors an enhancement of the Raman intensity several order of magnitude at resonance conditions has been observed. What is the potential enhancement factor in the case of bismuth vanadate and which material properties define the enhancement?

***Research question 3**: Can we access different electronic transitions by varying the experimental conditions?*

Because of the monoclinic crystal structure, optical anisotropy is expected and has been predicted by DFT calculations. Further research questions that emerge from the optical anisotropy are, first of all, does resonant Raman scattering reflect the optical anisotropy and secondly, can we make use of

the optical anisotropy to probe different electronic transitions? With these questions in mind, we planned an experiment using UV/Vis spectroscopy with the purpose to quantify the optical anisotropy experimentally. With this experiment we discovered the sensitivity of the optical absorption to the spontaneous strain in bismuth vanadate.

***Research question 4**: Do Raman modes of different symmetry couple to different electronic transitions?*

In monoclinic $BiVO_4$, we have Raman modes of different symmetries that can be distinguished experimentally by choosing different light polarization conditions. From this, we formulated the research question whether Raman modes of different symmetry respond differently in a resonant Raman experiment. If yes, can we make use of the different response and retrieve additional information on the electronic transitions involved in the experiment?

***Research question 5**: Do defect states contribute to resonant Raman scattering?*

Because of the relatively high band gap energy, defects states are expected and have been reported in the literature. The last research questions are related to the defects states. Do defect states contribute in a resonant Raman scattering experiment and what are their characteristic features? Could resonant Raman scattering be used as a potential technique to probe for defects states in oxide materials and how sensitive is the technique?

1.2 STRUCTURE OF THE WORK

The purpose of the first part of this manuscript is to provide the reader with all fundamental concepts required to follow the interpretation of our findings. Chapter 2 on the fundamentals is separated in two parts. The first part summarizes physical concepts to explain the electronic and the vibrational properties of a crystalline material. The second part deals with the theories to describe the interaction of light with solids. Here, a strong focus lies on Raman scattering, which is the main technique used in this work.

Then all the instrumental details on the different techniques used in this work are given in Chapter 3. Starting with the experimental techniques to study the optical absorption, to photoluminescence spectroscopy, then the different Raman set-ups are presented and finally, the spectrometer to study lattice vibrations by inelastic neutron scattering is shown.

In Chapter 4, we make a proper assignment of all the Raman modes in the low-temperature monoclinic and in the high-temperature tetragonal phase. Then, we report for the first time on a phonon-to-phonon coupling in $BiVO_4$, which is strongly temperature- and polarization-dependent. The chapter is closed with the presentation of a preliminary study done by inelastic neutron scattering that suggests an additional mode-coupling phenomena.

In Chapter 5, we show the temperature dependence of the optical absorption across the phase transition and quantify the optical anisotropy. In the second part of this chapter, we discuss the origin of the broad PL emission in $BiVO_4$.

In Chapter 6, we present our results from three resonant Raman studies on different samples and on slightly modified set-ups. We discuss the limitations of each study and present the resonant Raman profiles of the different Raman modes in $BiVO_4$. We work out the characteristic features in the resonant Raman profiles and demonstrate that the enhancement of the resonance depends on the particular lattice vibration involved in the scattering process. For the first time in $BiVO_4$, we found experimental proof that defect states contribute to the resonant Raman scattering.

2 FUNDAMENTALS

Because of the optical absorption in the visible light range, bismuth vanadate can be classified as a semiconductor. To study the fundamental material properties, we choose to work on single crystals. The understanding of resonant Raman effects requires a good knowledge of the electronic band structure, the optical properties and lattice dynamics of the material of interest. The purpose of this chapter is to introduce the basic concepts to understand the fundamental material properties of a semiconducting crystal and its interaction with light. The first part of this section concentrates on the concepts describing fundamental material properties; the electronic band structure of a semiconductor and lattice vibrations in a crystal. The second part of this chapter introduces the different optical processes of importance to this work, namely optical absorption, photoluminescence and Raman scattering.

2.1 MATERIAL PROPERTIES OF A SEMICONDUCTING CRYSTAL

2.1.1 *Electronic band structure of a semiconductor*

The arrangement of atoms in a solid results in an overlap of the outer orbitals. As a consequence, the electronic levels broaden into bands in contrast to the discrete levels of free atoms.[69] The lower energy band is called the *valence band*. At 0 K, the valence band is completely filled with electrons. The higher energy band is called the *conduction band* and contains no electrons at 0 K. At finite temperature, the electrons distribute according to the Fermi-Dirac distribution leading to some electrons missing in the valence band and some extra electrons in the conduction band [48]. Electrons in the conduction band can contribute to the conductivity. In a semiconductor the energy bands of allowed states are separated by an energy gap, the so called *band gap*. In an ideal crystal, there are no allowed states in the band gap. However, a variety of allowed states can be introduced by defects and impurities. The concept of the *density of states* results from the band formation in solids and described the continuum of the energies of the electronic levels in a solid. This continuity gives rise to continuous absorption and emission bands in solids.

The interatomic distance in a crystal varies with the crystallographic directions. That is why we must consider the distribution of electronic states not only in energy but also in momentum space. This is typically done in a *band structure diagram* that visualizes the distribution of allowed electronic states in energy and momentum. From quantum mechanics the crystal momentum p is expressed by $p = k\hbar$ where k is the wavevector and $\hbar$ is the reduced Planck constant $= h/2\pi$ with h being the Planck's constant. Figure 2.1(a)

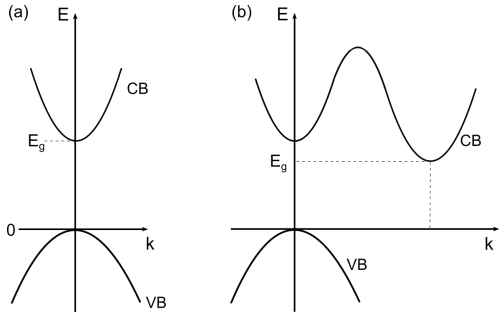

Figure 2.1: Band structure diagram of a (a) direct and an (b) indirect semiconductor. Valence and conduction band are approximated as parabolic bands. The sketches are adapted from Pankove [69].

sketches the band structure diagram of a direct semiconductor. In a direct semiconductor, the valence band maximum and the conduction band minimum are located at the same k vector. Near the valence band minimum and conduction band maximum, the bands are very often approximated as parabolic bands [69]. The valence band $E_v(k)$ and conduction band $E_c(k)$ are then given by

$$E_v(k) = -\frac{k^2\hbar^2}{2m_h^*}$$
$$\text{and} \tag{2.1}$$
$$E_c(k) = E_g + \frac{k^2\hbar^2}{2m_e^*}$$

where m_e^* and m_h^* are the effective electron and the effective hole masses, respectively. E_g is the band gap energy separating the valence band and the conduction band. The minimum in the conduction band may not occur at the same k value as the valence band maximum. In this case, we refer to an indirect band gap semiconductor. Figure 2.1(b) shows the electronic band structure diagram of an indirect semiconductor.

The density of states gives the number of states within a given energy range $E \to E + dE = g(E)dE$ of an electronic band.[39] The density of states $g(E)$ is worked out by first calculating the density of states in momentum space g(k) [84]. With the relationship $g(E) = g(k)\frac{dk}{dE}$ and the assumption of parabolic bands (Equation 2.1) the density of states is calculated to

$$g(E_v) = \frac{1}{2\pi^2}\left(\frac{2m_h^*}{\hbar^2}\right)^{3/2}|E_v|^{1/2}.$$
$$\text{for the valence band and to} \tag{2.2}$$
$$g(E_c) = \frac{1}{2\pi^2}\left(\frac{2m_e^*}{\hbar^2}\right)^{3/2}(E_c - E_g)^{1/2}$$
$$\text{for the conduction band.}$$

The knowledge of the density of states is important for the calculation of the interband absorption in Section 2.2.1.2.

2.1.2 *Phonons and lattice vibrations in a crystal*

Lattice vibrations are the oscillations of atoms in solids around their equilibrium position. In a crystal, the equilibrium position is defined by the crystal lattice and recurs periodically. The atoms are bounded to each other so that the movements are not independent of each other and can be considered as waves propagating through the crystal lattice. Lattice vibrations can be approximated as harmonic oscillators that are coupled to each other.

2.1.2.1 *The infinite linear diatomic chain and its phonon dispersion*

In this section, we we will have a look at the lattice vibrations of an infinite diatomic linear chain. The model is far too simple to describe lattice vibrations in a real crystal but it allows us to have a look at some basic concepts of lattice vibrations in a real crystal. We are following the mathematical derivation described in the classical solid-state physics book of Ibach and Lüth [50].

Figure 2.2 shows the mechanical model of the linear atomic chain with two atoms per unit cell and a lattice constant a. The atom with mass M_1 is placed at the origin and the atom of mass M_2 is placed at $a/2$. The atoms are connected to their neighbours via a spring with the spring constant f. The motion of atoms are parallel to the chain and thus only longitudinal motions of atoms are considered. Only coupling of the nearest neighbours are considered.

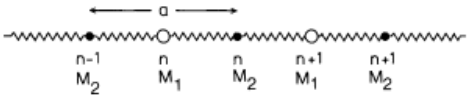

Figure 2.2: Mechanical model of the linear diatomic chain, taken from Ibach and Lüth [50].

The force on each of the two atoms in the unit cell is given by the equation of motion:

$$\begin{aligned} M_1 \frac{d^2 u_{n1}}{dt^2} + f(u_{n1} - u_{n-1,2}) - f(u_{n2} - u_{n1}) = 0, \\ M_2 \frac{d^2 u_{n2}}{dt^2} + f(u_{n2} - u_{n1}) - f(u_{n+1,1} - u_{n2}) = 0. \end{aligned} \tag{2.3}$$

where u_{n1} is the displacement of the atom with M_1 and u_{n2} is the displacement of the atom with M_2 in the n^{th} unit cell. This can be solved by wave-type functions of the following form

$$\begin{aligned} u_{n1}(t) = \frac{1}{\sqrt{M_1}} u_1 \exp\left(i(kan - \omega t)\right), \\ u_{n2}(t) = \frac{1}{\sqrt{M_2}} u_2 \exp\left(i(kan - \omega t)\right), \end{aligned} \tag{2.4}$$

where u_1 and u_2 is the amplitude of the oscillation, ω the angular frequency and $k = 2\pi/\lambda$ the wave vector of the propagating wave with λ being the wavelength. We insert Equation 2.4 into Equation 2.3 and obtain a homogeneous linear system of equations

$$\begin{aligned}(\frac{2f}{M_1} - \omega^2)u_1 - \frac{f}{\sqrt{M_1 M_2}}(1 + e^{-ika})u_2 = 0,\\ -\frac{f}{\sqrt{M_1 M_2}}(1 + e^{ika})u_1 + (\frac{2f}{M_2} - \omega^2)u_2 = 0.\end{aligned} \tag{2.5}$$

A solution exists if the determinant of the coefficient matrix is zero:

$$\begin{vmatrix} \frac{2f}{M_1} - \omega^2 & -\frac{f}{\sqrt{M_1 M_2}}(1 + e^{-ika}) \\ -\frac{f}{\sqrt{M_1 M_2}}(1 + e^{ika}) & \frac{2f}{M_2} - \omega^2 \end{vmatrix} = 0$$

The solutions are given by

$$\omega^2 = f\Big(\frac{1}{M_1} + \frac{1}{M_2}\Big) \pm f\Big[\Big(\frac{1}{M_1} + \frac{1}{M_2}\Big)^2 - \frac{4}{M_1 M_2} sin^2\frac{ka}{2}\Big]^{1/2} \tag{2.6}$$

and visualized in Figure 2.3. The solution has two branches. The solution is periodic in k with a period $k = \frac{2\pi}{a}$. Thus, it is sufficient to plot the phonon dispersion for one period. The period from $k = -\frac{\pi}{a}$ to $k = \frac{\pi}{a}$ is called the *first Brillouin zone*. The solution with $\omega = 0$ at $k = 0$ is called the *acoustic branch*. The solution with finite ω at $k = 0$ is called the *optical branch*.

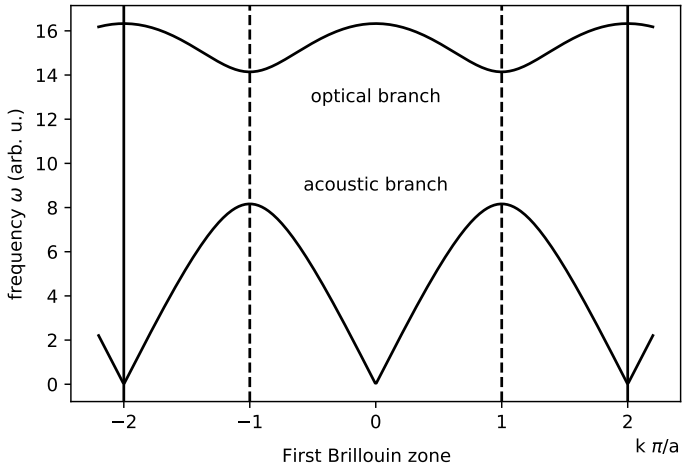

Figure 2.3: Phonon dispersion of a linear diatomic chain calculated from Equation 2.6.

2.1.2.2 *The three-dimensional crystal*

For the linear diatomic chain we considered only longitudinal atomic motions. In three dimensions, motion of atoms is possible in all three directions.

There are two additional transverse waves in which the atoms are displaced perpendicularly to the wave propagation. For a three-dimensional crystal with N atoms with n atoms per unit cell, there will be $3N$ normal modes on $3n$ branches, 3 acoustic branches and $3n - 3$ optical branches. In most cases, the lattice vibrations are neither transverse nor longitudinal. Only in special crystal symmetries and special crystal directions, the lattice vibrations are strictly transverse or longitudinal. One example are the high-symmetry directions [100], [110] and [111] in the face-centered cubic (fcc) crystal. Gallium phosphide (GaP) is a classical semiconductor with a fcc symmetry. Figure 2.4(a) shows the calculated phonon dispersion of bulk GaP in the high symmetry directions. Figure 2.4(b) shows the reciprocal lattice of a fcc lattice with is high-symmetry directions defined; X corresponds to the [001] direction, K to [110] and L to the [111]. GaP has 2 atoms in its unit cell, thus 6 phonon branches are expected; 3 acoustic branches and 3 optical branches. All 6 branches are observed in the L direction. At the Brillouin zone center Γ, the optical branch is degenerate. A classical technique to measure optical phonons at the BZ center is Raman spectroscopy. Figure 2.4(c) shows the Raman spectrum of GaP with the TO and the LO mode that matches the frequencies of the optical phonons at Γ from the calculation of the phonon dispersion shown in Figure 2.4(a).

2.1.2.3 *Phonons - Quantization of lattice vibrations*

The energy of a lattice vibration is quantized by a multiple of $\hbar\omega$ [42]. The quanta is known as phonon, in analogy to the quantum of electromagnetic radiation, a photon. The concept of phonons is used here to explain the excitation of optical vibrations by light, namely Raman scattering.

The number of phonons N_k at energy E_k and a given temperature T is given by the *Bose-Einstein statistics*[50] and given by

$$N_k = \frac{1}{\exp \frac{E_k}{k_B T} - 1} \tag{2.7}$$

where k_B is the Boltzman constant.

2.2 INTERACTION OF LIGHT WITH A SEMICONDUCTING CRYSTAL

The interaction of light with a semiconducting crystal results in many different optical phenomena. In this section, we will first define the optical processes that can occur when light interacts with a semiconductor.

Figure 2.6 shows schematically the optical processes that can occur when a semiconducting material is illuminated by light. At the material surface, part of the light is *reflected* and the rest is *transmitted*. Inside the material, parts of the transmitted light may be *absorbed* or *scattered* while the remaining light propagates through the material. Absorption occurs if the energy of the incident light matches the energy difference of a vibrational or an electronic transition in the material. Some of the absorbed light might be re-emitted at

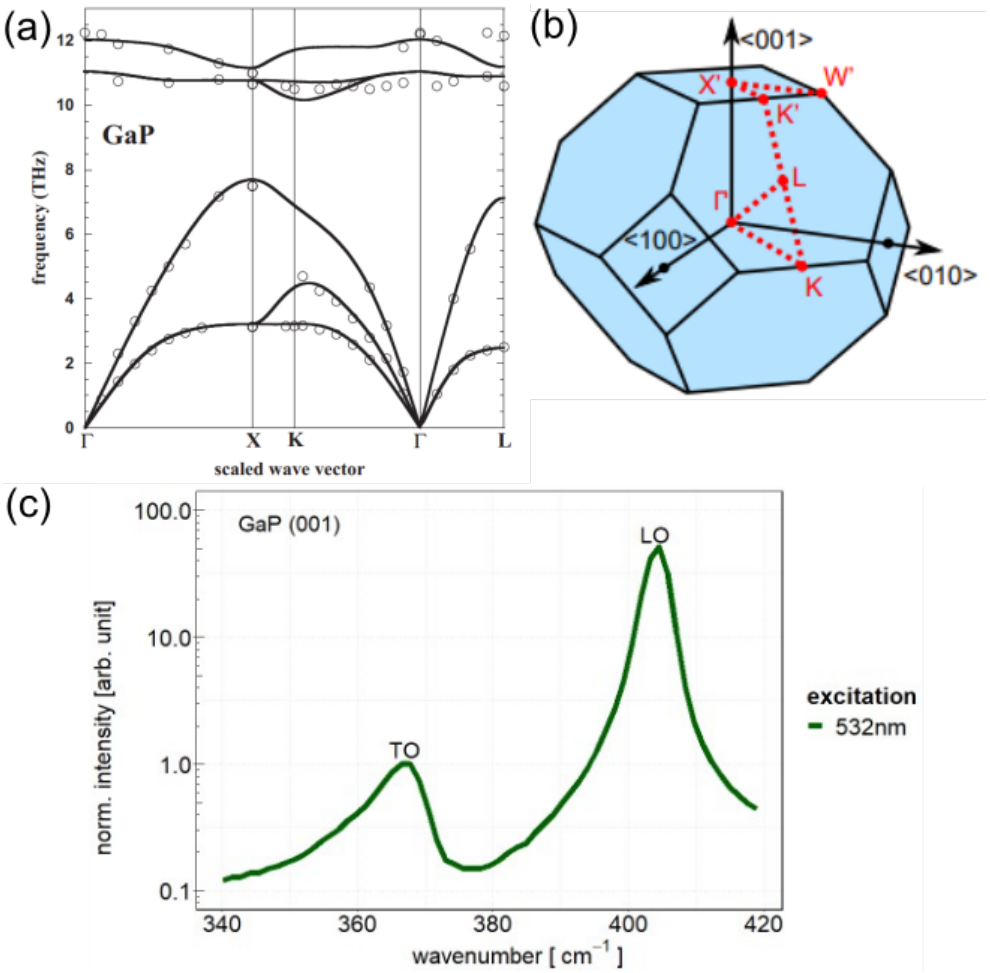

Figure 2.4: (a) Calculated phonon dispersion of bulk GaP in the high symmetry directions, taken from Lindsay et al. [60]. The experimental data are shown with black circle and were measured by inelastic neutron scattering by Borcherds et al. [12]. (b) Reciprocal lattice of face-centered cubic crystal with its high-symmetry directions highlighted in red, taken from Ventura [105] (c) Raman spectrum of single crystal GaP showing two Raman bands corresponding to one longitudinal optical (LO) phonon mode and the two degenerate transverse optical (TO) phonon modes.

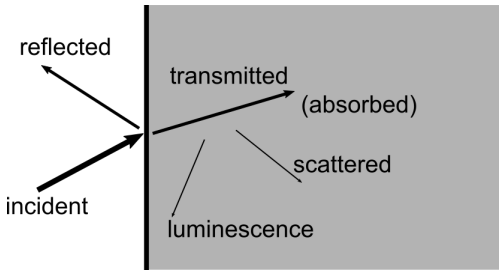

Figure 2.5: Schematic diagram of the optical processes that occur when a sample is illuminated by light, adapted from Yu and Cardona[115].

a different frequency. This process is known as *photoluminescence*. Scattering changes the direction and possibly the energy of the light that propagates through the material. The scattering is said to be *elastic* if the energy of the scattered light is unchanged and *inelastic* if the energy changes during the scattering process. The strongest optical processes are reflection and absorption. The amount of the transmitted light strongly depends on the reflection and the absorption.

2.2.1 *Optical absorption*

In this section, we will have a deeper look at the optical absorption. In an absorption process, a photon excites an electron from a lower energy state to a higher energy state. As a consequence, the absorption spectrum of a semiconductor contains information on the electronic band structure and on the density of states, as we will see later in this section.

2.2.1.1 *Absorption coefficient*

The reflection at the material surface is described by the *coefficient of reflection* or the *reflectance* R and is given by the ratio of the reflected power to the incident power at the surface. The *coefficient of transmission* or *transmittance* T is given by the ratio of transmitted power to incident power I/I_0. The absorption of a material is quantified by its *absorption coefficient* α. The light propagating through an absorbing material loses its intensity according to Beer's law. Assuming the light is propagating in the z direction, Beer's law[39] is written as

$$I(z) = I_0 e^{-\alpha z} \tag{2.8}$$

where $I(z)$ is the light intensity at position z and I_0 is the light intensity at $z = 0$. The absorption coefficient strongly depends on the wavelength of light so that the material might absorb one colour but not the other.

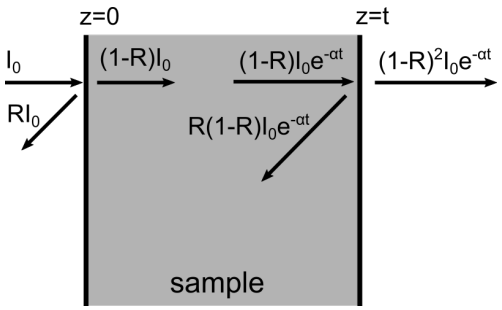

Figure 2.6: Schematic representation of a sample of thickness t with reflection at front and back surface, adopted from Pankove [69].

In a next step, we will calculate the transmittance of a sample of thickness t assuming reflection at the front and the back surface as shown in Figure 2.6. The light passing the first surface is $(1 - R)I_0$, the light reaching the second

surface is $(1-R)I_0e^{-\alpha t}$ and only the fraction $(1-R)(1-R)I_0e^{-\alpha t}$ leaves the sample at the second surface. The transmittance is then given by

$$T = \frac{I}{I_0} = (1-R)^2 e^{-\alpha t}. \tag{2.9}$$

For strong absorbing materials, the reflection at the back surface can be neglected and Equation 2.9 simplifies to

$$\begin{aligned} T &\approx (1-R)e^{-\alpha t} \\ \alpha &= \frac{1}{t}\ln(\frac{1-R}{T}) \end{aligned} \tag{2.10}$$

2.2.1.2 *Theory of interband optical absorption*

The fundamental absorption refers to a band-to-band transition and results in a rapid increase in the absorption as a function of the wavelength of the incident light. The absorption coefficient is proportional to the probability to excite an electron from the initial to the final state, the electron density in the initial state and the density of empty final states.[69] We distinguish a direct from an indirect band-to-band transition. The distinction of direct and indirect transition has strong impacts on the characteristics of the optical absorption and will be discussed in the following. We hereby follow the derivation presented in Pankove [69] and Fox [39].

DIRECT INTERBAND OPTICAL ABSORPTION is observed in materials with a direct band gap and is typically characterized by a very steep increase in the optical absorption coefficient with frequency. The absorption is often orders of magnitude larger than the optical absorption due to an indirect band-to-band transition. The absorption process due to a direct band-to-band transitions is schematically shown in Figure 2.7 (a). As defined in Section 2.1.1, the valence band maximum and the conduction band minimum are located at $k = 0$ in a direct band gap semiconductor. An electron is excited from the valence band to the conduction band by the absorption of a photon. The momentum of a visible photon h/λ (λ is the wavelength of visible light, thousands of angstrom) is very small compared to the crystal momentum hr/a (a is the lattice constant, a few angstroms). That is why the photon absorption alone cannot introduce a change in momentum. In the band structure diagram, the photon absorption is presented as vertical line.

In this case, the transition probability is independent of the photon energy and every initial state at energy E_i is associated to one final state at energy E_f.[69] Energy conversation requires

$$E_f = h\nu - |E_i| \tag{2.11}$$

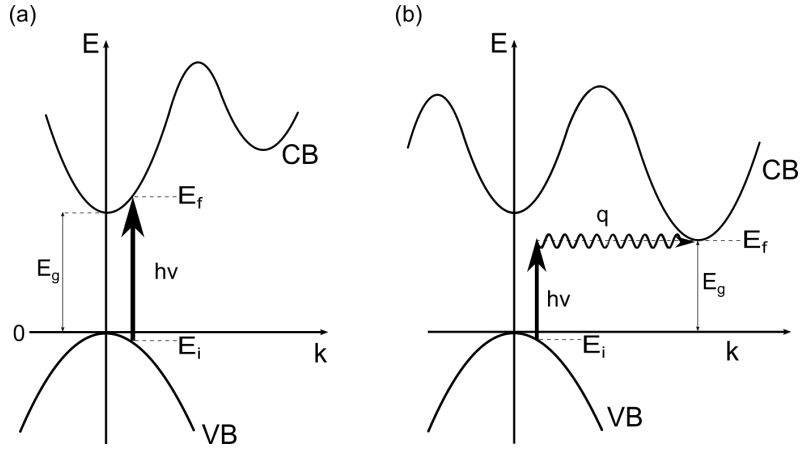

Figure 2.7: Interband transition in a semiconductor (a) with direct band gap and (b) indirect band gap, adopted from Fox [39]. The vertical arrow corresponds to photon absorption. The wiggled arrow in (b) represents phonon absorption or emission.

where $h\nu$ is the energy of the photon. Inserting the Equations 2.1 for parabolic bands in Equation 2.11 gives

$$\hbar\nu = E_g + \frac{\hbar^2 k^2}{2m_e^*} + \frac{\hbar^2 k^2}{2m_h^*}. \tag{2.12}$$

We define the reduced electron-hole mass μ as

$$\frac{1}{\mu} = \frac{1}{m_e^*} + \frac{1}{m_h^*}. \tag{2.13}$$

With this, Equation 2.12 simplifies to

$$\hbar\nu = E_g + \frac{\hbar^2 k^2}{2\mu}. \tag{2.14}$$

The electron-hole density of states or *joint density of states* $g(\hbar\nu)$ is then given by

$$\begin{aligned} &\text{For } h\nu < E_g,\ g(h\nu) = 0 \\ &\text{and} \\ &\text{For } h\nu > E_g,\ g(h\nu) = \frac{1}{2\pi^2}\left(\frac{2\mu}{\hbar^2}\right)^{3/2}(\hbar\nu - E_g)^{1/2} \end{aligned} \tag{2.15}$$

The absorption coefficient is proportional to the joint density of states and therefore given by

$$\begin{aligned} &\text{For } h\nu < E_g,\ \alpha(h\nu) = 0 \\ &\text{and} \\ &\text{For } h\nu > E_g,\ \alpha(h\nu) \approx (h\nu - E_g)^{1/2} \end{aligned} \tag{2.16}$$

Below the band gap if $h\nu < E_g$ there is no absorption and the energy increases with $(h\nu - E_g)^{1/2}$ for photon energies larger than the band gap energy. With a change in temperature, the absorption edge shifts in first approximation with the variation of the band gap as a function of temperature.[39]

INDIRECT INTERBAND OPTICAL ABSORPTION is observed in semiconductors with an indirect band gap and schematically shown in Figure 2.7(b). The minimum of the conduction band is found away from the BZ center, very often at the Brillouin zone edge. In this case, the transition requires not only a change in energy but also a large change in momentum and therefore the transition rate for indirect absorption is much smaller than for direct absorption. The absorption of a visible photon cannot provide the required change in momentum so that the transition must involve a phonon to conserve momentum. Only phonons with the required change in momentum can be used for the transition. These are typically the longitudinal- and the transverse acoustic phonons [69]. The characteristic energy of the phonon is E_q and energy conservation implies

$$E_f = h\nu + E_i \pm E_q \tag{2.17}$$

where E_f is the energy of the final state and E_i is the energy of the initial state. In contrast to a direct transition, all occupied states in the valence band can connect to all empty states in the conduction band in the indirect transition [69]. This implies that the absorption coefficient is proportional to the product of the densities of initial states and the final states integrated over all combinations of possible states. In analogy to Equation 2.2, the density of states in the initial sate at energy E_i are given by

$$g(E_i) = \frac{1}{2\pi^2}\left(\frac{2m_h^*}{\hbar^2}\right)^{3/2}|E_i|^{1/2}. \tag{2.18}$$

The density of states in the final state at energy E_f are given by

$$\begin{aligned} g(E_f) &= \frac{1}{2\pi^2}\left(\frac{2m_e^*}{\hbar^2}\right)^{3/2}(E_f - E_g)^{1/2} \\ &= \frac{1}{2\pi^2}\left(\frac{2m_e^*}{\hbar^2}\right)^{3/2}(\hbar\nu - E_g \pm E_q + E_i)^{1/2}. \end{aligned} \tag{2.19}$$

For an indirect transition, the absorption coefficient not only depends on the densities but also on the probability of the interaction with a phonon which is a function $f(N_q)$ of the number of phonons N_q. The number of phonons is given by the Bose-Einstein statistic given in Equation 2.7. Hence, the absorption coefficient can be calculated by the integration of the following Equation

$$\alpha(h\nu) = Af(N_q)\int_0^{E_q - h\nu \pm E_q} |E_i|^{1/2}(h\nu - E_g \pm E_q + E_i)^{1/2}\mathrm{d}E_i \tag{2.20}$$

where A is a constant. For *phonon absorption*, the absorption coefficient is calculated to

$$\alpha_a(h\nu) = \frac{A(h\nu - E_g + E_q)^2}{\exp \frac{E_q}{k_B T} - 1} \tag{2.21}$$

for $h\nu > E_g - E_q$. For *phonon emission*, the probability is proportional to $N_q + 1$ and the absorption coefficient is calculated to

$$\alpha_e(h\nu) = \frac{A(h\nu - E_g - E_q)^2}{1 - \exp \frac{-E_q}{k_B T}} \tag{2.22}$$

for $h\nu > E_g + E_q$. If the $h\nu > E_g + E_q$, phonon emission and absorption are possible and the absorption coefficient is given by the sum of Equation 2.21 and Equation 2.23

$$\alpha(h\nu) = \alpha_a(h\nu) + \alpha_e(h\nu). \tag{2.23}$$

At low temperatures, the phonon density is small and phonon emission is the dominating process. Figure 2.8 shows experimental data of the absorption in Germanium measured at different temperatures. Germanium has an indirect band gap. At 20 K, phonon emission dominates and the square root of the absorption coefficient $\alpha^{1/2}$ has a linear dependence proportion to $(h\nu - E_g - E_q)$. Extrapolation to $\alpha = 0$ gives $E_g + E_q$. At increasing temperatures, both phonon emission and phonon absorption are possible. The contribution of phonon emission of Equation 2.23 and phonon absorption of Equation 2.21 are clearly visible for the measurements done at temperatures larger than 77 K. In this case, the extrapolation to $\alpha = 0$ gives at values of $E_g + E_q$.

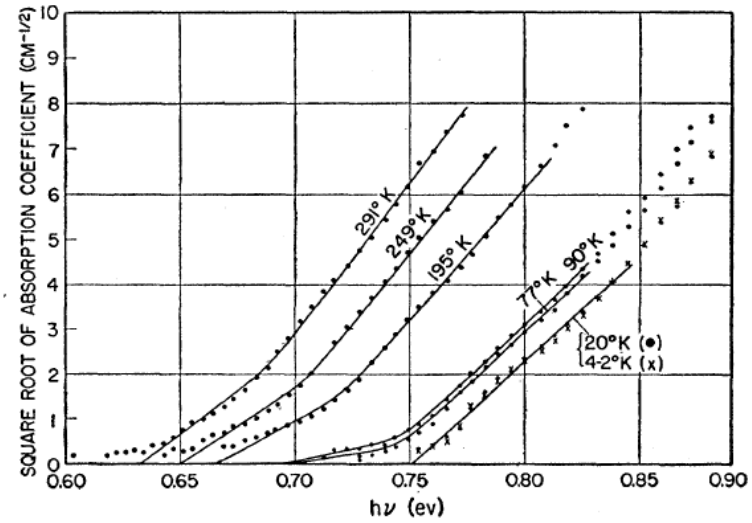

Figure 2.8: Experimental data of the absorption in Germanium measured at different temperatures, taken from Macfarlane and Roberts [64]. The plot shows the square root of the absorption coefficient $\alpha^{1/2}$ as function of photon energy $h\nu$.

THE TAUC METHOD is commonly used in the literature to derive the band gap energy from absorption spectra. The method was developed by Tauc in 1966 to estimate the band gap energy in amorphous germanium using an optical absorption spectrum [99]. Davis and Mott [33, 67] have developed the method further in a more general work on amorphous semiconductors. They showed that the energy dependence of the absorption coefficient can be expressed by the following equation:

$$(\alpha \cdot h\nu) = A(h\nu - E_g)^{1/n} \tag{2.24}$$

where E_g is the band gap energy, n is an exponent that characterizes the nature of the interband transition. We saw that the absorption coefficient depends on the density of state in the initial and in the final state. For parabolic bands, the density of states has a square root dependence on energy $g(E) \approx (E)^{1/2}$. That is the reason why we have $n = 2$ for direct band-to-band transition. In case of an indirect band-to-band transition, all occupied states in the valence band can connect to all empty states in the conduction band. Hence, the absorption coefficient is proportional the product of states in the initial and final states integrated over all possible combinations (Equation 2.20) leading to $n = 1/2$ for indirect band-to-band transition. The basic procedure is to plot $\alpha \cdot h\nu^n$ as a function of $h\nu$ in a so-called *Tauc plot*. In a second step, the data are fitted by linear fit near the absorption edge. If data are described by a straight line for $n = 2$, the dominating process is the direct band-to-band transition. If data are described by a straight line for $n = 1/2$, the dominating process is the indirect band-to-band transition.

2.2.2 *Photoluminescence*

In the previous section, we discussed the optical absorption in a semiconductor. All transitions that might be involved in the absorption mechanism can occur in the opposite direction and create a characteristic emission spectrum [69]. To observe such an emission spectrum, electrons with a higher energy are required. If the electrons are excited via optical absorption prior to the emission, we refer to photoluminescence. In this section, we will discuss the underlying principles of photoluminescence.

In a photoluminescence (PL) experiment, an electron-hole pair is generated by the absorption of an optical photon from the incident light source with an energy above the band gap of the material. On a very short timescale, the generated electrons and holes relax to the band edges (*thermalization*). After the generation of electron-hole pairs and their thermalization, the free electrons and holes recombine via different radiative transitions. Figure 2.9 visualises different radiative transitions that are typically observed in a photoluminescence experiment. Free electrons in the conduction band and free holes in the valence band may recombine via a *band-to-band transitions*, process a) in Figure 2.9. In a direct semiconductor, the band-to-band transitions occur with a very high probability. In an indirect semiconductor, however, electron-hole recombination can only occur via a phonon-assisted transition

for which the transition probability is much lower. When there are defects in the material a so-called *free-to-bound transition* is likely to happen. Depending on their charge in the ionized state, we distinguish acceptors from donors. After ionization an acceptor is negatively charged while a donor is positively charged [4]. In a free-to-bound transition, a free electron from the conduction band recombines with a hole bound to an acceptor state or an electron bound to a donor state recombines with a free hole in the valence band. The free-to-bound transitions are more likely to be observed at low temperatures [4]. If both donor and acceptor states are present in the material, a donor-acceptor pair transition will occur. A donor-acceptor pair transition gets more likely than free-to-bound transition if the temperature is even further decreased. At increasing temperatures, defects states are thermally ionized and the emission from band-to-band transitions gains importance.[4]

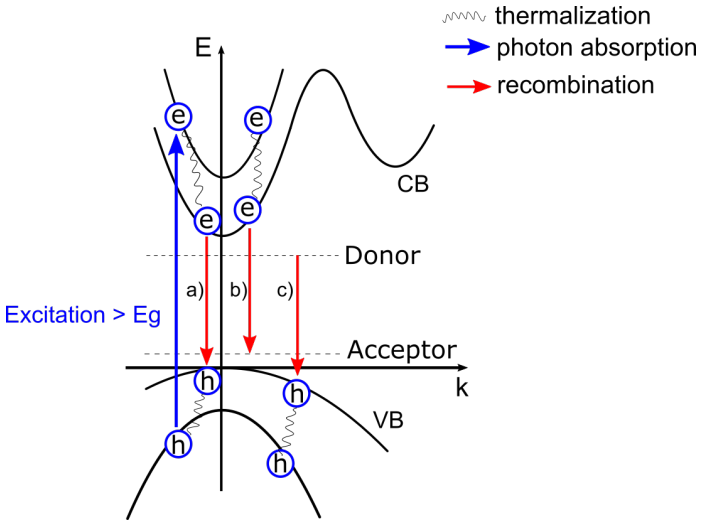

Figure 2.9: Typical radiative transitions in a photoluminescence experiment a) band-to-band transition b) free electron from the conduction band recombines with bound hole in an acceptor state c) bound electron in a donor state recombines with free hole in the valance band.

2.2.2.1 *Distinguish Band-to-band transitions from defect related transitions*

As shown in Figure 2.9, PL emission can originate from different transitions in the material. The different transitions can be distinguished by their transition energy and by the change of the transition energy and luminescence yield with varying excitation intensity and temperature [2]. In first approximation, the transition energy $\hbar\omega_{max}$ of a PL line can be obtained by a Gaussian fit to the data.

$$I_{PL} \sim \exp\left(-\frac{(\hbar\omega - \hbar\omega_{max})^2}{2\sigma^2}\right) \tag{2.25}$$

with $\hbar\omega$ being the photon energy and σ being the linewidth (FWHM= $\sqrt{8\ln 2}\sigma$). The assignment of PL lines by the transition energy requires basic knowl-

edge of the band structure of the investigated material. The luminescence yield of a transition line follows a simple power law

$$Y_{PL}(\Phi) \sim \Phi_{ex}^{k} \tag{2.26}$$

with Φ being the excitation intensity and k is a characteristic parameter that is typically between 0.5 and 2 [2, 69]. For band-to-band transitions k is typically 1 or larger than 1 [89]. A k smaller than 1 indicates an emission originated from a defect level [89].

2.2.2.2 *Photoluminescence due to band-to-band transitions*

At room temperature, defect levels are generally emptied by thermal ionization and therefore photoluminescence mainly occurs due to the radiative band-to-band transitions. In a direct semiconductor with a band gap energy E_g, the shape of the PL band is given by the joint density of states (Equation 2.15) and their occupation which is given by the Boltzmann distribution [115]:

$$\begin{aligned} &\text{For } h\omega < E_g,\ I_{PL} \propto 0 \\ &\text{and} \\ &\text{For } h\omega > E_g,\ I_{PL} \propto (\hbar\omega - E_g)^{1/2} \exp\left[-\frac{\hbar\omega - E_g}{k_B T}\right] \end{aligned} \tag{2.27}$$

where $\hbar\omega$ is the emitted photon energy and $k_B T$ is the product of the Boltzmann constant and the temperature. Calculating the first derivative of Equation 2.27, the peak maximum is at $E_g + k_B T/2$. At room temperature $k_B T$ is only about 26 meV and therefore the band gap energy can be directly determined from the peak maximum. The full width half maximum (FWHM) is equal to 1.8 $k_B T$ [94].

In an indirect semiconductor, the radiative recombination of electron-hole pairs can only occur via phonon-assisted transitions. The probability of these transitions is generally smaller compared to a direct transition. The phonon population increases with increasing temperature so the photoluminescence due to an indirect band-to-band transition is expected to be stronger at higher temperatures.

2.2.2.3 *Deep defects level and electron-phonon coupling*

If deep defects are involved in the photoluminescence process, electron-phonon interaction might cause deviation from Gaussian-like PL bands (typically broad PL bands). In contrast to shallow defects, deep defects are unlikely to be ionized at room temperature. An alternative classification of defects is based on the degree of localization of the wave function of an electron. The wave function of a deep defect is typically localized on the length scale of an atomic bond, meaning the electron density is very high at the

defect [4]. For these highly localized defects, electron-phonon interaction is typically observed.

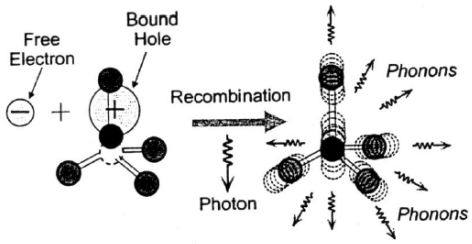

Figure 2.10: Schematic illustration of the recombination of a bound hole in an acceptor state and an electron, resulting in the emission of a photon and several phonons. The figure is taken from Reshchikov [80].

The mechanism is illustrated in the following example assuming an acceptor-like deep defect state. The hole wave function is localized at one of the bonds and causes the atoms to shift from their ideal atomic positions, see Figure 2.10. After recombination of a free electron with the bound hole at the acceptor state, the atoms would move back to their original site. The atomic relaxation causes lattice vibrations, in other words emission of multiple phonons. The radiative emission energy (energy of the photon) is reduced by the energy released by the emission of phonons. The number of emitted phonons changes from one recombination process to the other resulting in a broad PL band. The strength of the electron-phonon coupling is described by the Huang-Rhys factor S and represents the average number of phonons involved in an optical transition.[80] The larger S, the stronger the electron-phonon coupling and the broader the PL band. The configuration coordination (CC) diagram is often used to explain the phonon-emission process that accompanies the radiative recombination involving a highly localized defect [69, 80]. Figure 2.11 shows a simple one-dimensional CC diagram of an acceptor-like deep defect. In the excited state the defect is neutral, in the ground state the defect is charged negatively. The adiabatic potentials represent the total potential energy of the defect in its ground and excited state. The frequencies of the dominant phonon mode in the ground and excited state might be different and are distinguished by $\hbar\omega_0^g$ and $\hbar\omega_0^e$. This is also true for the Huang-Rhys factor that can be different for the excited and the ground state. The equilibrium position of the ground and excited state are displaced according to the coupling strength. At low temperatures, the optical transitions take place from the zero vibrational level in the excited state to the n^{th} vibrational level of the ground state (transition AB in Figure 2.11). After the emission of a photon, the system relaxes to the zero vibrational level in the ground state by the emission of several phonons with energies $\hbar\omega_0^g$ (transition BC).

THE ZERO-PHONON-LINE E_0 is the energy difference between the ground state and the excited state of the deep defect. It is the energy of the actual electronic transition involved in the PL emission. In case of strong electron-

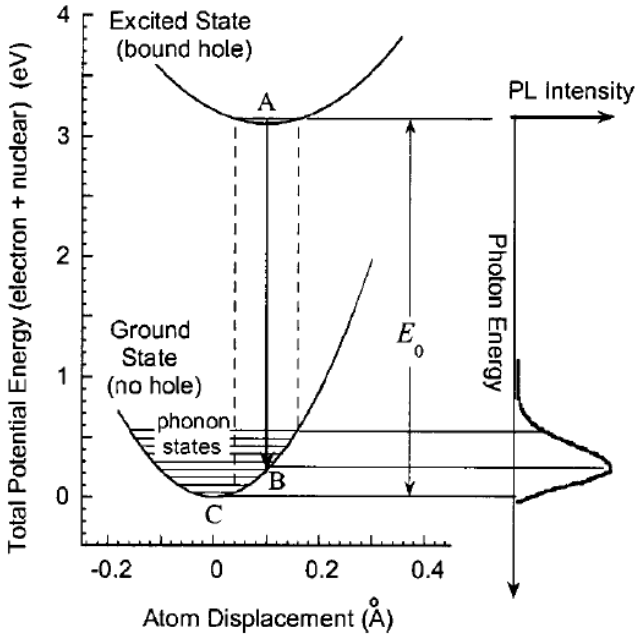

Figure 2.11: Simple one-dimensional configuration coordination diagram describing the recombination process involving a localized carrier. The figure is taken from Reshchikov [80].

phonon coupling the zero phonon line can strongly deviate from the position of the PL maximum. In this case, the defects level cannot be extracted by just measuring the PL maximum at low temperatures. Data have to be careful analysed and accurate fitting of the peak shape is important.

THE RESHCHIKOV MODEL accounts for the slight asymmetry of the PL peak due to electron-phonon coupling which is typical for deep defects. The derivation of the following equation can be found in Ref. [78].

$$I_{PL} \sim \exp\left[-2S_e\left(\sqrt{\frac{E_0 + 0.5\hbar\Omega_e - \hbar\omega}{E_0 + 0.5\hbar\Omega_e - \hbar\omega_{max}}} - 1\right)^2\right] \tag{2.28}$$

The Huang-Rhy factor S_e of the excited state, is a measure of the electron-phonon coupling strength. E_0 is the zero-phonon-line, $\hbar\Omega_e$ is the energy of the effective phonon mode in the excited state, $\hbar\omega_{max}$ is the position of the PL intensity maximum and $\hbar\omega$ is the PL photon energy.

Defining $E_0^* = E_0 + 0.5\ \hbar\Omega$ and the relaxation energy of the ground state $\Delta E = E_0^* - \hbar\omega_{max}$, Equation 2.28 can be rewritten in the following form

$$I_{PL} = I_{PL}^{max} \exp\left[-2S_e\left(\sqrt{\frac{E_0^* - \hbar\omega}{\Delta E}} - 1\right)^2\right] \tag{2.29}$$

with I_{PL}^{max} being the intensity at the PL band maximum. The shape of the PL band is uniquely described by the parameters S_e and ΔE [79].

2.2.3 *Raman scattering*

This section aims to introduce the basic concepts of Raman scattering in crystals. After a short introduction, the basic features of light scattering are explained by the classical approach. Then a more general expression is derived by the quantum mechanical approach followed by a discussion on resonant Raman scattering.

2.2.3.1 *Introduction*

As discussed in Section 2.2, if light interacts with matter it might be scattered inelastically. In this case, the incident and the scattered light have a frequency difference and this frequency difference is related to the properties of the investigated material. Inelastic scattering of light is also referred to as Raman scattering in honor to its discoverer C.V. Raman, an Indian scientist. C.V. Raman was awarded the Nobel Price in 1930 for his discovery. In a Raman experiment, an incident photon with energy E_i and momentum k_i reaches the sample and is scattered, resulting in a photon with a different energy E_s and momentum k_s. Energy and momentum must be conserved in the overall scattering process

$$\begin{aligned} &E_s = E_i \pm E_q \\ &\text{and} \\ &k_s = k_i \pm q \end{aligned} \tag{2.30}$$

where E_q and q are the energy and momentum of the involved excitation. In most cases the excitations are lattice vibrations, i.e. phonons. In this case E_q and q are the energy and momentum of the phonon that is created or annihilated in the Raman scattering event. Other sources for excitations are magnons or plasmons. The energy difference between incident and scattered light is very small. The spectral distribution of the scattered light is typically analyzed relative to the spectrum of the incident light. The energy difference between incident and scattered light is referred to as *Raman shift* and typically given in units of wavenumbers.

In a scattering experiment, the incident photon distorts the electron cloud around the atomic nuclei. The ability to distort the electron cloud is measured by the change in the polarizability for molecules or by the change in the susceptibility for crystals. In this work, we focus on the Raman scattering in crystals. Therefore, we use the susceptibility in Section 2.2.3.2 to derive the basic features of Raman scattering. If only electron cloud distortion is involved, the scattered photon has the same energy as the incident photon. We refer to *elastic* or *Rayleigh scattering*. If nuclear motion is involved in the scattering process, energy will be transferred from the incident photon to the crystal lattice or from the lattice to the scattered photon. In this case, we refer to *inelastic* or *Raman scattering*. The characteristic lattice vibrations of a crystal are called *normal modes* and are related to the structural properties of the material. Every material has a unique set of normal modes,

so Raman spectroscopy can be used to probe materials properties in detail. However, Raman scattering not only contains information on the characteristic normal modes but also on the electronic states as it will be discussed in Section 2.2.3.2 and Section 2.2.3.9.

2.2.3.2 *Classical description of Raman Scattering*

We follow the classical approach described, for example, in Kuzmany [58] or Yu and Cardona [115]. In a crystal, Raman scattering originates from the change in susceptibility induced by an electromagnetic field of the incident radiation. For an applied electric field $\mathbf{E} = E_0 \cos(\omega_1 t)$ oscillating at frequency ω_1, a dielectric polarization density is induced

$$P_j = \epsilon_0 \chi_{jl} E_l \tag{2.31}$$

where ϵ_0 is the vacuum permittivity, χ_{jl} is the susceptibility and the indices j and l run from 1 to 3. In the linear approximation the susceptibility is given by

$$\begin{aligned} \chi_{jl} &= (\chi_{jl})_0 + \sum_k (\frac{\partial \chi_{jl}}{\partial Q_k})_0 Q_k \\ &\text{or} \\ \chi_{jl} &= (\chi_{jl})_0 + (\chi'_{jl,k})_0 Q_k \end{aligned} \tag{2.32}$$

The displacement of the atoms is represented by the normal coordinates Q_k of the oscillations. The indices j and l run from 1 to 3 and k runs over $3n-3$ normal coordinates for the vibrations, where n is the number of atoms in the unit cell. In other words, k runs over all optical phonon modes at the BZ center. $\partial\chi_{jl}/\partial Q_k$ is called the *Raman tensor* and often written as $(\chi'_{jl})_k$ or $\chi'_{jl,k}$. For one individual mode, the Raman tensor is a $3x3$ matrix. The oscillation of atoms for the normal mode k is given by

$$Q_k = Q_{k0} \cdot \cos(\omega_k t) \tag{2.33}$$

where Q_{k0} is the amplitude and ω_k is the frequency of the oscillation. Inserting Equation 2.32 and Equation 2.33 into Equation 2.31, the total polarization density is given by

$$P_j = \epsilon_0 (\chi_{jl})_0 E_0 \cos(\omega_1 t) + \epsilon_0 \cdot (\chi'_{jl,k})_0 \cdot Q_{k0} \cdot \cos(\omega_k t) \cdot E_0 \cos(\omega_1 t) \tag{2.34}$$

Applying the trigonometric sum rule $\cos(a)\cos(b) = 1/2[\cos(a-b) + \cos(a+b)]$ gives

$$P_j(\omega) = \epsilon_0 (\chi_{jl})_0 E_0 \cos(\omega_1 t) + \frac{\epsilon_0 (\chi'_{jl,k})_0 Q_{k0}}{2} [\cos(\omega_1 - \omega_k)t + \cos(\omega_1 + \omega_k)t] E_0 \tag{2.35}$$

From Equation 2.35 we see that the light is scattered elastically at frequency ω_1 (Rayleigh) but also inelastically at sidebands with frequencies

$\omega_1 \pm \omega_k$. The part of the inelastically scattered light with a frequency shift $\omega_1 - \omega_k$ is the Stokes Raman scattering while the part with frequency shift $\omega_1 + \omega_k$ is the anti-Stokes Raman scattering. Figure 2.12 shows a schematics of a typical spectrum with Rayleigh at $0\,\mathrm{cm}^{-1}$ and Stokes and anti-Stokes sidebands. The Rayleigh intensity is always much stronger compared to the Raman intensity. Only one in 10^6-10^8 photons which is scattered, is Raman scattered. The Stokes intensity at positive frequencies is stronger than the anti-Stokes intensity at negative intensities. Because the spectrum is symmetric and the Stokes intensity is stronger, we only consider Stokes scattering in the presented work.

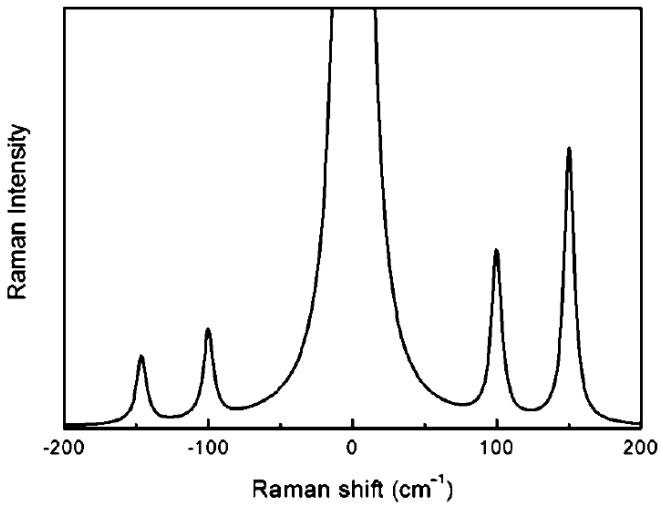

Figure 2.12: Schematic representation showing the Rayleigh (at $0\,\mathrm{cm}^{-1}$) and Stokes and anti-Stokes Raman sidebands, taken from Jorio [52].

The intensities of Stokes and anti-Stokes scattering depend on the number of phonons in the ground and in the excited state which is given by the Bose-Einstein distribution function given in Equation 2.7. The probabilities for Stokes and Anti-Stokes are different. In the Stokes process, the system goes from $n \to n+1$ while in anti-Stokes the system goes from $n+1 \to n$. The intensity ratio of the Stokes band to the anti-Stokes band is therefore expressed by

$$I_S / I_{aS} \propto \frac{n+1}{n} = \exp\left(\hbar\omega_k / k_B T\right) \tag{2.36}$$

where $\hbar\omega_k$ is the energy of the phonon of the normal mode k and I_S and I_{aS} is the intensity of the Stokes band and the anti-Stokes band, respectively. The intensity of the Stokes band is always stronger than the intensity of a anti-Stoke band but the anti-Stokes scattering gains importance at increasing temperature.

2.2.3.3 *Raman cross section*

The Raman intensity is often expressed in terms of the Raman cross section that relates the intensity of the scattered light to the intensity of the incident

light. Since the intensity of the Stokes and anti-Stokes scattering are related by the Equation 2.36, it is sufficient to derive the Raman cross section for the Stokes component. Experimentally, we measure the intensity of the scattered light into a solid angle $d\Omega$ with a frequency ω_s with respect to the light intensity of the incident light, the so-called *spectral differential cross section* $\frac{d^2\sigma}{d\Omega d\omega_s}$. According to Hayes and Loudon [44], the spectral differential cross section for Stokes scattering is proportional to

$$\frac{d^2\sigma}{d\Omega d\omega_s} \propto V\omega_1\omega_s^3\frac{n_s}{n_1}\left|\epsilon_0\sum_{j,l}e_j^s\chi'_{jl,k}e_l^1\right|^2\{n(\omega_k)+1\}g_k(\omega_k) \tag{2.37}$$

in which V is the scattering volume, ω_s and n_s are the frequency and the refractive index of the scattered light and ω_1 and n_1 are frequency and the refractive index of the incident light. An important feature of the spectral differential cross section is the $\omega_1\omega_s^3$ dependence which is often referred to as the ω_1^4 dependence under the approximation $\omega_1 \approx \omega_s$. Because of the ω_1^4 dependence, working in the UV can be beneficial in some cases to improve the Raman sensitivity. $n(\omega_k)$ is the Bose-Einstein statistics and $g_k(\omega)$ is the lineshape of the Raman band, in which k labels the different Raman modes. Because the spectral differential cross section depends on the Bose-Einstein statistics, a correction of the Bose-Einstein function $n(\omega)+1$ is necessary when comparing Raman intensities measured at different temperatures. e_j^s and e_l^1 are the unit vectors of the polarization of the scattered and incident light in which j and l run from 1 to 3. $\chi'_{jl,k}$ is the derivative of the susceptibility or the Raman tensor. The *differential cross section* $\frac{d\sigma}{d\Omega}$ is obtained by integrating the spectral differential cross section over the line-width of a Raman band in the scattered spectrum and the *cross section* σ is obtained by the integration of the differential cross section over all directions in space.[44] The cross section defines the total scattering in all directions and therefore requires measurements of the scattered intensity at a large number of scattering angles. These kind of experiments are rarely made. One example is the measurement of the absolute Raman cross section of benzene by Skinner and Nilsen [91]. In many cases, the determination of the differential cross section is sufficient because the frequency of the Raman modes and the lifetimes of the corresponding excited states are independent of the scattering angle. In this work, we use the differential cross section as a measure for the scattered light intensity and simply refer to it as Raman cross section *Rcs*.

2.2.3.4 *Raman selection rules*

In Section 2.2.3.2 we defined the Raman tensor as the derivative of the susceptibility $\chi'_{jl,k}$. A vibration is *Raman active* if its Raman tensor has non-vanishing components:

$$\frac{\partial\chi_{jl}}{\partial Q_k} \neq (0), \forall j,l = 1,2,3 \text{ and } k = 3n-3 \tag{2.38}$$

Based on symmetry analysis, Group theory can predict which components are zero and which are finite for the various point groups. The Raman tensors of many point groups are listed in many books[51] or on the Bilbao server[11]. An important quantity of the Raman cross section is the following quadratic term

$$|\sum_{j,l} e_j^s \chi'_{jl,k} e_l^1|^2. \tag{2.39}$$

Hence, the Raman cross section depends on the polarization of the scattered and the incident radiation. By measuring the dependence of the scattered intensity on the incident and scattered polarization, one can retrieve the symmetry of the Raman tensor and thus the symmetry of the corresponding phonon mode.[115] For certain polarization directions of the incident and scattered light, the scattered light vanishes depending on the symmetry of the Raman tensor. This ability to suppress bands of certain symmetries is called *Raman selection rule*.

2.2.3.5 *Characteristic lineshape of a Raman band*

The lineshape of a Raman band $g_k(\omega)$ in Equation 2.37 is typically modeled by the imaginary part of the damped harmonic oscillator function [44]

$$g_k(\omega) = \frac{\omega\Gamma_k}{(\omega_k^2 - \omega^2)^2 + \omega^2\Gamma_k^2}\,, \tag{2.40}$$

in which damping is given by Γ_k, ω_k is the eigen-frequency and ω the external field. The damping is a measure of the phonon lifetime. For $\omega_k \gg \Gamma_k$ the solution of the damped harmonic oscillator approaches a Lorentzian curve. In a Raman experiment, the scattered intensity is typically measured as a function of the Raman shift which is the energy of the incident photon $\hbar\omega_1$ minus the energy of the scattered photon $\hbar\omega_s$ given in units of cm^{-1}. A Raman spectrum shows a peak at a phonon energy $\pm\hbar\omega_k$ in which positive energies are Stokes process and negative energies are anti-Stokes. The scattered intensity is then modeled by a Lorentzian curve

$$I(\omega) = \frac{I_0}{\pi}\frac{\Gamma_k}{(\omega - \omega_k)^2 + \Gamma_k^2}\,, \tag{2.41}$$

in which I_0 is the integrated intensity and therefore correspond to the Raman cross section of the Raman band. The full width at half maximum is given by $2\,\Gamma_k$. A Raman spectrum with n Raman bands is then modelled by the sum n Lorentzian functions.

2.2.3.6 *Phonon-phonon coupling and its deviations from a Lorentzian lineshape*

In practice, there are many phenomena that lead to deviations from a Lorentzian-like lineshape. One phenomena that is of relevance to this work is the coupling between two phonons of the same symmetry. Phonon-phonon coupling leads to an asymmetric lineshape that is typically modelled by the *coupled damped harmonic oscillators (coupled oscillators) model*. This model has been

first presented by Barker and Hopfield [8]. The basic theory is presented in the following. Figure 2.13 shows the mechanical model for a system of two coupled phonons. Each phonon is described as a damped harmonic oscillator with an effective mass m, spring constant k and damping coefficient Γ. The two masses m_α and m_β are mechanically connected by an additional spring $k_{\alpha\beta}$ and dashpot $\Gamma_{\alpha\beta}$ which models the coupling of the two oscillators.

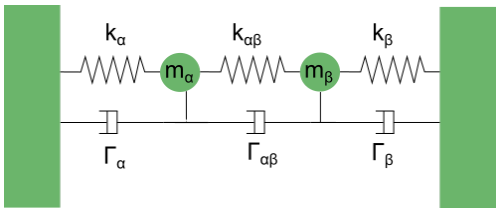

Figure 2.13: Mechanical model of two damped harmonic oscillators a and b described by the spring constants k_α, k_β and the damping coefficients Γ_α,Γ_β. The coupling is complex and given by the coupling spring constant $k_{\alpha\beta}$ and the damping coefficient $\Gamma_{\alpha\beta}$.

The Green's function formalism provides a more generalized form to model a system of coupled oscillators. The Green's function may be written as $G^{-1} = g = -\omega^2\mathbf{1} + i\omega\mathbf{\Gamma} + \boldsymbol{K}$ in which $\mathbf{1}$ is the unit matrix and $\boldsymbol{K}$ and $\mathbf{\Gamma}$ are the restoring force and the damping matrices [65]. Using the Green's function formalism, a system of two coupled damped harmonic oscillators [53, 88] may be written

$$\begin{bmatrix} \omega_\alpha^2 - \omega^2 + i\omega\Gamma_\alpha & \Delta^2 + i\omega\Gamma_{\alpha\beta} \\ \Delta^2 + i\omega\Gamma_{\alpha\beta} & \omega_\beta^2 - \omega^2 + i\omega\Gamma_\beta \end{bmatrix} \begin{bmatrix} G_{\alpha\alpha} & G_{\alpha\beta} \\ G_{\alpha\beta} & G_{\beta\beta} \end{bmatrix} = \begin{bmatrix} 1 & 0 \\ 0 & 1 \end{bmatrix} \tag{2.42}$$

in which the parameters Δ, Γ_α, Γ_β and $\Gamma_{\alpha\beta}$ are assumed to be frequency independent and the effective mass m is set to unity. The two oscillators are characterized by their eigen-frequencies ω_α and ω_β and their damping coefficients Γ_α and Γ_β. The eigen-frequency squared is equal to the spring constant divided by the effective mass, $\omega_i^2 = k_i/m_i$ in which i can be α or β. The frequencies ω_α, ω_β and the damping Γ_α and Γ_β correspond to the eigen-frequencies and the damping of the uncoupled phonons α and β. The coupling is described by Δ which is the force constant of the spring connecting the two oscillators and $\Gamma_{\alpha\beta}$ which is the dashpots connecting the two modes. Δ and $\Gamma_{\alpha\beta}$ must be constraint by $detK \geqslant 0$ and $det\Gamma \geqslant 0$ [98]. This means that the coupling cannot be arbitrary large. Equation 2.42 is solved to give the following Green's functions coefficients:

$$G_{\alpha\alpha} = (\omega_\beta^2 - \omega^2 + i\omega\Gamma_\beta)/D \tag{2.43}$$

$$G_{\alpha\beta} = -(\Delta^2 + i\omega\Gamma_{\alpha\beta})/D \tag{2.44}$$

$$G_{\beta\beta} = (\omega_\alpha^2 - \omega^2 + i\omega\Gamma_\alpha)/D \tag{2.45}$$

where $D = (\omega_\alpha^2 - \omega^2 + i\omega\Gamma_\alpha)(\omega_\beta^2 - \omega^2 + i\omega\Gamma_\beta) - (\Delta^2 + i\omega\Gamma_{\alpha\beta})^2$.

The Equation 2.42 is overdetermined allowing an arbitrary choice of diagonalization and therefore produces an infinite number of solutions [62]. Some reasonable assumptions have to be made. Many authors [65, 98] proposed to make the assumptions on the complex coupling of modes in which the two limiting cases occur for only real coupling ($\Gamma_{ab} = 0$) and only imaginary coupling ($\Delta = 0$). The parameters obtained in the two cases are entirely different as well as the physical interpretation. Because of the overparametrization, verification of the model parameters is necessary. One possibility is the verification of the model parameter at multiple temperatures as it has been done for example by Scarparo et al. [87] or Scalabrin et al. [86]. All model parameters should show constant or simple temperature dependence.

The Raman (Stokes) scattering intensity is correlated with the imaginary part of the susceptibility χ''

$$S(\omega) = R\chi''(\omega)[n(\omega) + 1] \,, \tag{2.46}$$

where n is the phonon population factor given by the Bose-Einstein statistics, R is an experimental constant and T is the absolute temperature of the sample. Using matrix notation, the complex susceptibility $\chi(\omega)$ for the coupled oscillator model is given by $\chi(\omega) = \tilde{P} \cdot G \cdot P$ in which P and $\tilde{P}$ are one column and one row vectors. The imaginary part of the complex susceptibility $\chi''(\omega)$ is then given by

$$\chi''(\omega) = -Im[P_\alpha^2 G_{\alpha\alpha}(\omega) + 2P_\alpha P_\beta G_{\alpha\beta}(\omega) + P_\beta^2 G_{\beta\beta}(\omega)], \tag{2.47}$$

P_α, P_β being the oscillator strengths of the vibration mode α and β.

2.2.3.7 *First- and higher-order Raman processes*

So far we discussed scattering events in which the photon energy exchange creates only one phonon (first-order Raman processes). In this case, the momentum transfer can be neglected so that $k_s - k_1 = q \approx 0$ is valid. Since we use visible light in the Raman experiment, the momentum of the incident light is much smaller compared to the crystal momentum, see discussion in Section 2.2.1.2. That is why only excitations close to the Brillouin zone center Γ are accessible in the first-order Raman process. If two, three or more scattering events occur in the Raman process we refer to a second-, third- or higher-order Raman process. In this case the restriction $q \approx 0$ is relaxed. For a scattering process involving two phonons, the energy and momentum conservation is given by

$$\begin{aligned} \omega_1 - \omega_s &= \omega_k + \omega_{k'} \\ k_1 + k_s &= q + q' \approx 0 \end{aligned} \tag{2.48}$$

where q and q' are two excitations but not necessarily the same ones. In comparison to the first-order Raman process, higher-order Raman processes are not limited to the Γ-point and can originate from different points of the Brillouin zone. If the higher order Raman process originates from

the same phonon we refer to an *overtone*. The Raman signal appears at $nE_k(n = 1, 2, 3...)$. In case of a combination of phonon modes, the Raman signal appears at sum of different phonon energies $(E_{k1} + E_{k2} + ..)$.

2.2.3.8 *Quantum mechanical description of Raman Scattering*

The classical description developed in Section 2.2.3.2 describes the main features of Raman scattering. The observed Raman lines are shifted in energy from the incident laser line depending on the phonons involved in the process with the restriction on energy and momentum conservation. The quantum mechanical description is required to explain Raman intensities and the resonant Raman effects. Here, we are following the description of Yu and Cardona [115]. In the quantum mechanical description, the Raman scattering process is described in three steps which are depicted in Figure 2.14. Here, only electronic levels are shown. However, the excited energy levels n and n' do not have to be real electronic levels. At the beginning of the process, the electron is in its initial state. Step1: The incident light excites the electron to the intermediate state n by the absorption of a photon. Here, we assume n to be a real electronic state. In this case the process is resonant and we draw the electronic level with a solid line. Step 2. The electron is scattered into a so called virtual state n' by emitting a phonon by the electron phonon interaction. Virtual states are represented by dashed lines. Step 3: The electron radiatively recombines with the emission of the scattered photon. The electron remains unchanged after the scattering process, final and initial state of the electron are identical.

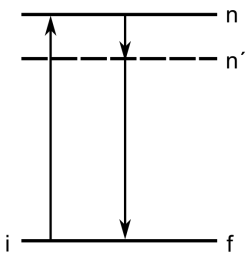

Figure 2.14: Schematic representation of the Raman process in a crystal, adopted from Jorio [52]. Transition $i \rightarrow n$ and $n' \rightarrow i$ correspond to photon absorption and emission. The small downward arrow from $n \rightarrow n'$ symbolized the electron losing energy to the lattice by electron phonon interaction (emission by a phonon). The electron remains unchanged after the Raman scattering process, so initial and final state are identical.

The scattering probability of phonons can be calculated by the third-order perturbation theory. This is often done by the use of Feynman diagrams to keep track of the various processes that may occur in the scattering process. The basic notation uses propagators for electrons, phonon and photons and vertices to highlight a point at which interaction occurs. In total, there are six scattering processes that contribute to the first-order Raman scattering. The Feynman diagram of all six scattering processes are shown in Figure 2.15,

taken from Yu and Cardona [115]. The interaction presented in a Feynman diagram proceed from left to right as a function of time. The basic Raman process described in the beginning of this section is shown in Figure 2.15(a). The other Feynman diagrams are obtained by a different order of the vertices.

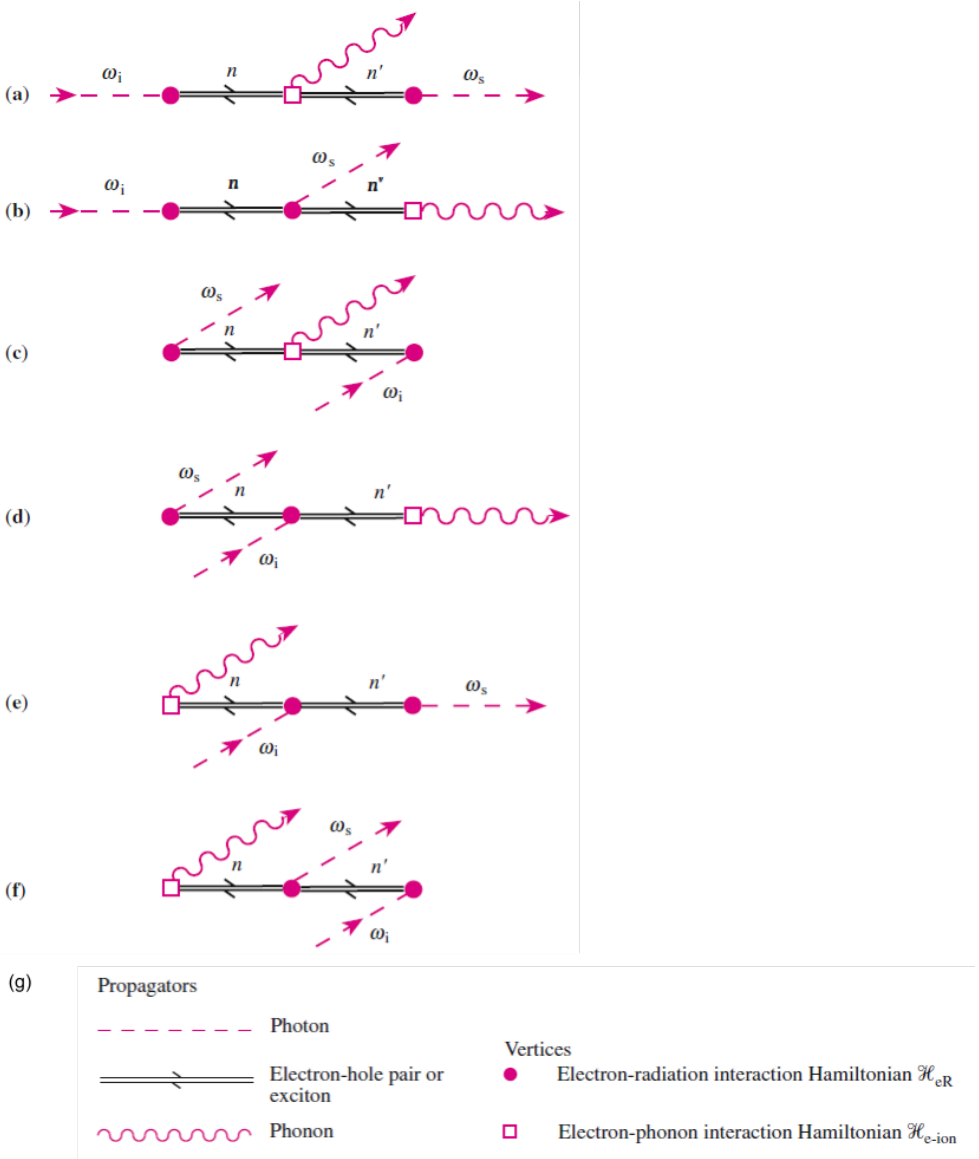

Figure 2.15: (a-f) Feynman diagrams for the six scattering processes that contribute to the first-order Raman (Stokes) scattering, taken from Yu and Cardona [115]. (g) Legend of symbols used in the Feynman diagrams.

We will first discuss the Feynman diagram shown in Figure 2.15(a). The first vertex in the diagram introduces the following term in the scattering probability

$$\sum_n \frac{\langle n|\mathcal{H}_{eR}|i\rangle}{[\hbar\omega_1 - (E_n - E_i)]} \tag{2.49}$$

in which $|i\rangle$ is the initial state with the energy E_i and $\langle n|$ is the intermediate state with the energy E_n. The interaction between the electron and the incident radiation is described by the Hamiltonian $\mathcal{H}_{eR}$. The energy of the incident photon is $\hbar\omega_1$. The sign of $\hbar\omega_1$ depends on whether the energy quantum is absorbed (+ sign) or emitted (- sign). The term is summed over all intermediate states $\langle n|$. The second vertex introduces a second term that is multiplied

$$\begin{aligned}\sum_{n,n'} \frac{\langle n|\mathcal{H}_{eR}|i\rangle \langle n'|\mathcal{H}_{e-ion}|n\rangle}{[\hbar\omega_1 - (E_n - E_i)][\hbar\omega_1 - (E_n - E_i) - \hbar\omega_q - (E_{n'} - E_n)]} \\ = \sum_{n,n'} \frac{\langle n|\mathcal{H}_{eR}|i\rangle \langle n'|\mathcal{H}_{e-ion}|n\rangle}{[\hbar\omega_1 - (E_n - E_i)][\hbar\omega_1 - \hbar\omega_q - (E_{n'} - E_i)]}\end{aligned} \tag{2.50}$$

in which $|n'\rangle$ is the virtual state and the interaction energy $\mathcal{H}_{e-ion}$ is between the electron and the lattice. The sign of $\hbar\omega_q$ is negative because the phonon is emitted. Each vertex introduces a term with a matrix element of the interaction Hamiltonian in the numerator and an energy term in the denominator. The last energy denominator is converted into a delta function because of its representation of the overall energy conservation. The last energy term in the denominator is written

$$\begin{aligned}[\hbar\omega_1 - (E_n - E_i) - \hbar\omega_q - (E_{n'} - E_n) - \hbar\omega_s - (E_f - E_{n'})] \\ = [\hbar\omega_1 - \hbar\omega_q - \hbar\omega_s - (E_i - E_f)]\end{aligned} \tag{2.51}$$

The electrons are unchanged after the scattering process so the final electronic state $|f\rangle$ is identical to the initial state $\langle i|$. The last denominator is simplified to

$$[\hbar\omega_1 - \hbar\omega_q - \hbar\omega_s]. \tag{2.52}$$

With this the scattering probability of the scattering process in Figure 2.15(a) is given by

$$\begin{aligned}P_{ph}(\omega_s) = \frac{2\pi}{\hbar}\Big|\sum_{n,n'} \frac{\langle i|\mathcal{H}_{eR}(\omega_s)|n'\rangle \langle n'|\mathcal{H}_{e-ion}|n\rangle \langle n|\mathcal{H}_{eR}(\omega_i)|i\rangle}{[\hbar\omega_1 - (E_n - E_i)][\hbar\omega_1 - \hbar\omega_q - (E_{n'} - E_i)]}\Big|^2 \\ \times\delta[\hbar\omega_i - \hbar\omega_q - \hbar\omega_s].\end{aligned} \tag{2.53}$$

Following the same procedure for all six Feynman diagrams in Figure 2.15 the scattering probability is then given by

$$
\begin{aligned}
P_{ph}(\omega_s) = \frac{2\pi}{\hbar}\Big| \sum_{n,n'} & \frac{\langle i|\mathcal{H}_{eR}(\omega_s)|n'\rangle \langle n'|\mathcal{H}_{e-ion}|n\rangle \langle n|\mathcal{H}_{eR}(\omega_i)|i\rangle}{[\hbar\omega_1 - (E_n - E_i)][\hbar\omega_1 - \hbar\omega_q - (E_{n'} - E_i)]} \\
& + \frac{\langle i|\mathcal{H}_{e-ion}|n'\rangle \langle n'|\mathcal{H}_{eR}(\omega_s)|n\rangle \langle n|\mathcal{H}_{eR}(\omega_i)|i\rangle}{[\hbar\omega_1 - (E_n - E_i)][\hbar\omega_1 - \hbar\omega_s - (E_{n'} - E_i)]} \\
& + \frac{\langle i|\mathcal{H}_{eR}(\omega_i)|n'\rangle \langle n'|\mathcal{H}_{e-ion}|n\rangle \langle n|\mathcal{H}_{eR}(\omega_s)|i\rangle}{[-\hbar\omega_s - (E_n - E_i)][-\hbar\omega_s - \hbar\omega_q - (E_{n'} - E_i)]} \\
& + \frac{\langle i|\mathcal{H}_{e-ion}|n'\rangle \langle n'|\mathcal{H}_{eR}(\omega_i)|n\rangle \langle n|\mathcal{H}_{eR}(\omega_s)|i\rangle}{[-\hbar\omega_s - (E_n - E_i)][-\hbar\omega_s + \hbar\omega_1 - (E_{n'} - E_i)]} \\
& + \frac{\langle i|\mathcal{H}_{eR}(\omega_s)|n'\rangle \langle n'|\mathcal{H}_{eR}(\omega_i)|n\rangle \langle n|\mathcal{H}_{e-ion}|i\rangle}{[-\hbar\omega_q - (E_n - E_i)][-\hbar\omega_q + \hbar\omega_1 - (E_{n'} - E_i)]} \\
& + \frac{\langle i|\mathcal{H}_{eR}(\omega_i)|n'\rangle \langle n'|\mathcal{H}_{eR}(\omega_s)|n\rangle \langle n|\mathcal{H}_{e-ion}|i\rangle}{[-\hbar\omega_q - (E_n - E_i)][-\hbar\omega_q - \hbar\omega_s - (E_{n'} - E_i)]}\Big|^2 \\
& \times \delta[\hbar\omega_1 - \hbar\omega_q - \hbar\omega_s].
\end{aligned}
\tag{2.54}
$$

Equation 2.54 shows that Raman scattering contains much more information then the pure phonon energies. In principle, the Raman scattering probability contains information on the electron-phonon interaction, electron-radiation interaction and on the electronic band structure. Because of the many unknown parameters, it is usually impossible to extract the information from Equation 2.54. This becomes feasible if there is one dominant state that contributes to the scattering probability. This can be achieved by tuning the incident photon energy to an electronic transition. The enhancement of the Raman cross section near an electronic transition is called *resonant Raman scattering*. At resonant condition, only the first term of Equation 2.54 will dominate.

2.2.3.9 *Resonant Raman scattering*

In the previous section, we discussed that Raman scattering not only contains information on the phonon energies but also information on the electron-phonon, electron-radiation interaction and on the electronic band structure. At resonance condition, the non-resonance terms in the scattering probability (Equation 2.54) can be approximated as a constant. From the six Feynman diagrams, the first Feynman diagram shown in Figure 2.15(a) has the strongest contribution. The initial electronic state E_i is assumed to be the ground state of the crystals and its energy is assumed to be zero. We assign the resonant intermediate state $|a\rangle$ with energy E_a. When either the incident $\hbar\omega_i$ or the scattered photon energy $\hbar\omega_s$ is resonant with E_a, the energy denominator vanishes. To avoid the unphysical situation, E_a is replaced by a complex energy $E_a - i\gamma$ where γ is a damping constant. The damping constant is related to the finite lifetime τ of the intermediate state $|a\rangle$ by $\gamma = \hbar/\tau$. The depen-

dence of the Raman cross section on the incident photon energy is called a *resonant Raman profile*. The resonant Raman profile is then given by [52, 115]

$$I(\hbar\omega_i) = \left| \frac{A}{(\hbar\omega_1 - E_a - i\gamma)(\hbar\omega_s - E_a - i\gamma)} \right|^2 \quad \text{with} \quad \hbar\omega_s = \hbar\omega_i - \hbar\omega_q \tag{2.55}$$

in which A is a constant and $\hbar\omega_1$, $\hbar\omega_s$ and $\hbar\omega_q$ is the incident photon, scattered photon and the phonon energy, respectively. We distinguish *incoming resonance* for which $\hbar\omega_1 = E_a$ from *outgoing resonance* for which $\hbar\omega_s = E_a$. The phonon energy $\hbar\omega_q$ is small in comparison to the photon energies $\hbar\omega_i$ and $\hbar\omega_s$. That is why, incoming and outgoing resonance are difficult to observe experimentally. Only if the phonon energy and the lifetime of the excited state are large, incoming and outgoing resonance can be distinguished experimentally. One example is the resonant Raman profile of the G phonon in single-walled carbon nanotubes [40] shown in Figure 2.16.

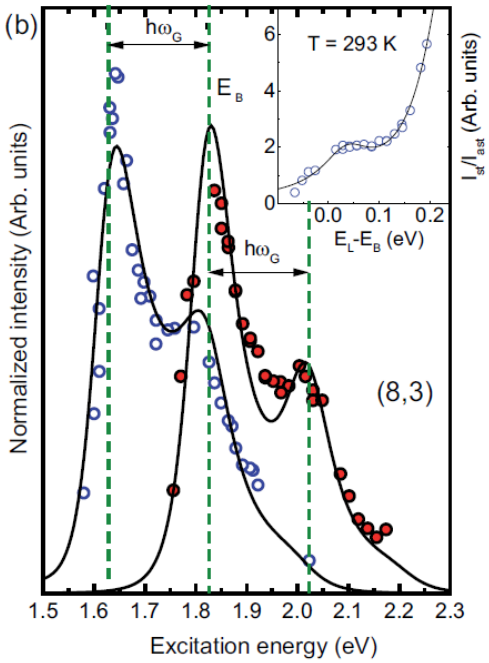

Figure 2.16: Resonant Raman profile of the Stokes G phonon (1584 cm^{-1}) and the anti-Stokes G phonon (1540 cm^{-1}) in single-walled carbon nanotubes showing incoming and outgoing resonance, taken from Gordeev et al. [40]. Stokes is shown with filled circles while anti-Stokes in shown with open circles.

3 INSTRUMENTAL ASPECTS

In this chapter, the main characterization methods used to study the structural and electronic properties of $BiVO_4$ will be presented. First UV/Vis spectroscopy and photoluminescence spectroscopy are introduced. Both techniques are commonly used to study electronic transitions in semiconducting materials. The second part of this chapter focuses on vibrational spectroscopies based on Raman scattering and on inelastic neutron scattering. In this work, Raman scattering and inelastic neutron scattering were used to study lattice dynamics in $BiVO_4$. Further, we discuss the instrumentals requirements for resonant Raman studies.

3.1 UV/VIS SPECTROSCOPY

The most direct and maybe the most simple method to study the electronic structure of a semiconductor is to measure the absorption spectrum. In the absorption process, a photon of known energy excites an electron from a lower- to a higher energy state. Placing a semiconductor sample at the output of a monochromator and studying the change of the transmitted and reflected radiation can reveal all the possible electronic transitions involved in the absorption process. In the following sections, the instrumental set-ups to study transmittance and reflectance are described as well as the way to compute the absorption from these two quantities.

3.1.1 *PerkinElmer Lambda 1050 UV/Vis/NIR spectrophotometer*

Figure 3.1 shows a sketch of the UV/Vis/NIR spectrophotometer Lambda 1050 from PerkinElmer. The radiation source is a deuterium tungsten halogen lamp that covers the energy range from 175 nm up to 3300 nm. The double holographic grating monochromator selects a narrow band $\Delta\lambda$ from the radiation source. The measurement is first completed at this spectral band before the monochromator selects the next spectral band. The monochromatic light is guided by different optical elements to the sample compartment. The polarization of the light can be controlled by a rotatable polarizer. In the sample compartment there are two light paths; the sample beam path and reference beam path. The chopper switches between reference and sample beam path. After the interaction with the sample, the light is collected by a 150 mm integrating sphere equipped with a photomultiplier InGaAs/PbS detector shown in the inset of Figure 3.1. The light intensity is measured in percentage of the incident light intensity. Therefore, the light intensity from the sample beam path is divided by the light intensity from the reference beam path. For transmittance measurements, the sample is placed

at the transmittance port at the entrance of the integrating sphere. For reflectance measurement, the sample is placed after the integrating sphere at the reflectance port.

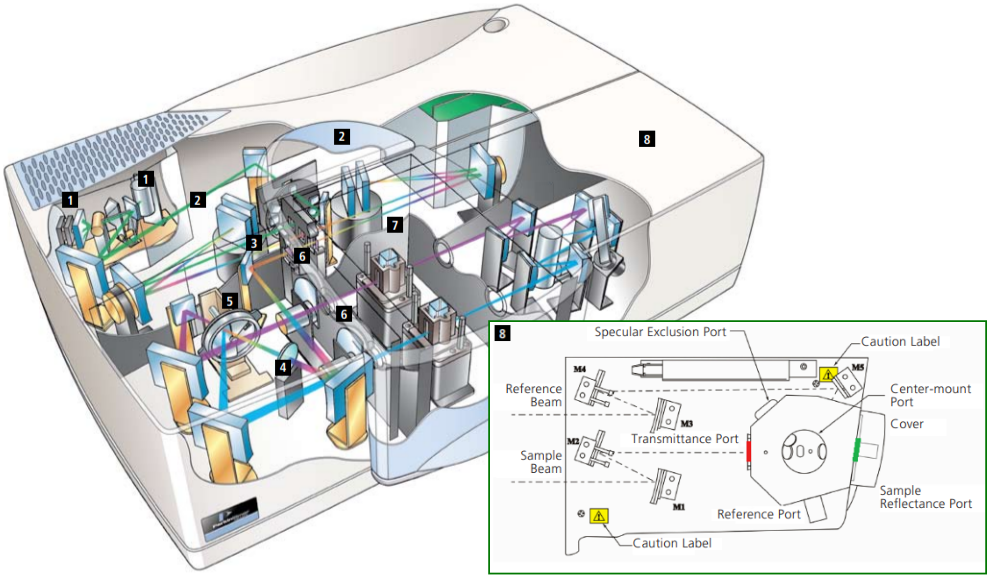

1. Deuterium tungsten halogen lamp (175nm-3300nm)
2. Double holographic grating monochromaters
3. Beam mask (mirror) for beam adjustment
4. Beam depolarizer
5. Switch between reference and sample beam
6. Beam attenuator
7. First sample compartment
8. Second sample compartment

Figure 3.1: Sketch of the UV/Vis/NIR spectrophomometer Lambda 1050 from PerkinElmer. The inset sketches the 2nd sample compartment with the 150 mm integrating sphere. The photomultiplier and the InGaAs/PbS detector are located inside the integrating sphere. The pictures are taken from Ref. [35] and [36].

3.1.2 *Jasco microspectrophotometer MSV-370*

The equipment described in this section belongs to the research group of Manfred Fiebig, ETH Zürich in Switzerland.

The microspectrophotometer MSV-370 from Jasco is made of a spectrophotometer attached to a microscope. This system is beneficial for the analysis of small samples. Another advantage is its compatibility with standard cryostat and standard temperatures stage solutions so that optical properties can be investigated as a function of temperature and pressure. Figure 3.2 shows a sketch of the Jasco microspectrophotometer MSV-370. The spectrophotometer operates a deuterium lamp for the UV and a halogen lamp for the visible and near infrared ranges. The principle components are sim-

ilar to the once described in the previous Section 3.1.1 on the spectrophotometer from PerkinElmer. The monochromator selects a spectral band from the light source. The light beam is split into a reference beam that is directly guided to the detector and a sample beam that is guided into the microscope. The polarization of the sample beam can be controlled by a polarizing element directly at the microscope. The sample is placed on the sample table in between the two Cassegrain-type objectives. In transmittance mode, the sample beam is focused by the Cassegrain objective CM1 onto the sample. The transmitted light is then collected by the Cassegrain objective CM2. In reflectance mode, however, the sample beam is focused and collected by the Cassegrain objective CM1. In both modes, the transmitted or reflected light is analyzed by the photomultipler and the PbS detector. After interacting with the sample, the light intensity is divided by the light intensity from the reference beam and given in percentage.

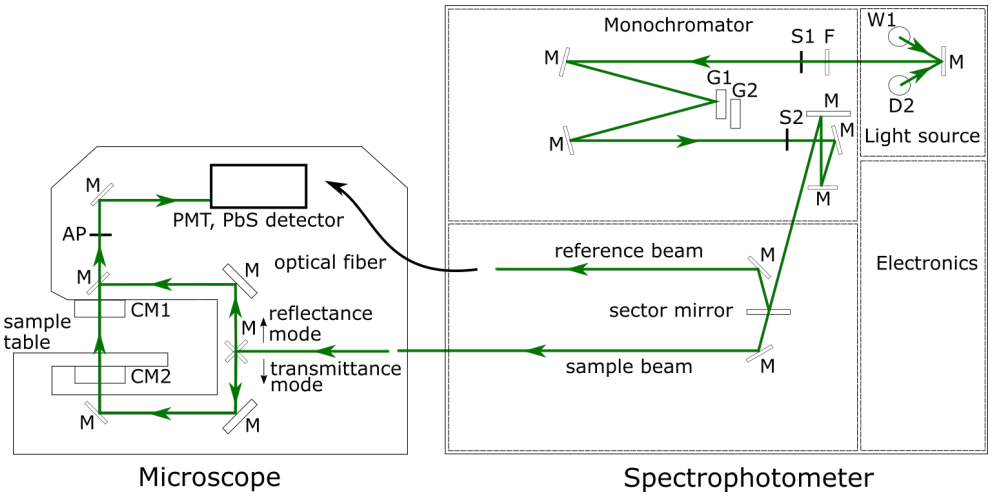

Figure 3.2: Sketch of the microspectrophotometer MSV-370 from Jasco. M: mirror, AP: aperture, CM1: Cassegrain objective, CM2: Cassegrain condensing mirror, PMT: photomultiplier, S1,S2: Slits, G1,G2: diffraction gratings, W1: halogen lamp, D2: deuterium lamp, F:filter

3.1.3 *Spectrometer Avantes StartLine AvaSpec-2048*

Figure 3.3 shows a sketch of the measurement set-up using a microscope, a LED light source and a spectrometer for the optical characterization of micro samples. We used a microscope from Olympus. As light source we used the *pE-Universal Collimator* from CoolLED attached to the microscope covering the wavelengths from 400 nm to 900 nm. The transmitted and reflected light was analyzed by the spectrometer *AvaSpec-2048* from Avantes. We used the polarizer from the microscope to select the polarization of the incident light. The sample was positioned on the microscope sample stage.

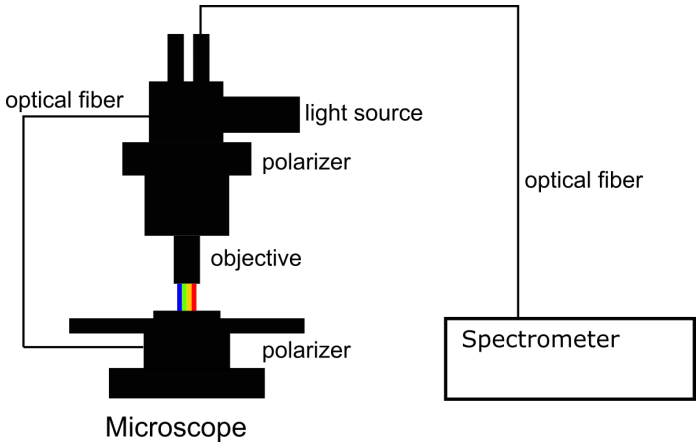

Figure 3.3: Sketch of the set-up using microscope, LED light source and spectrometer to measure transmittance and reflectance on micro spots.

3.1.4 *Measuring transmittance*

For correction, a dark spectral (0 %) baseline and a light spectral (100 %) baseline need to be recorded. For the dark spectral baseline, the sample beam path is measured without radiation. For the light spectral baseline, the sample beam path is measured with radiation but without the sample. For the thin film characterization on a transparent substrate, the light spectral baseline can be recorded with the bare substrate in the sample path. In this way, only the transmittance of the thin film itself is measured.

3.1.5 *Measuring reflectance*

The measured reflectance spectra are corrected for the reflectance of a reference material. For the reference material, there are two possibilities; a calibrated mirror or a calibrated white spectralon standard. In case the reflectance is measured using an integrating sphere as described in Section 3.1.1, the reflectance spectra needs to be corrected for the dark level of the integrating sphere as well.

3.2 PHOTOLUMINESCENCE

Emission of radiation is the inverse process of the absorption process. An electron occupying a higher energy states recombines to an empty lower-energy state by emitting electromagnetic radiation. All transitions that contribute to the absorption process can also occur in the opposite direction and produce a characteristic emission. Photoluminescence describes the emission after the excitation of the system via absorption. In the following, the set-up for photoluminescence measurements is described.

3.2.1 *Set-up*

The PL set-up described in this section belongs to the research group of Susanne Siebentritt, University of Luxembourg.

Figure 3.4 shows the setup used to measure photoluminescence. Different laser sources can be connected to the set-up; Argon-ion laser (514.5 nm), laser diodes (663 nm or 405 nm). Before the laser light hits the sample, it passes several filters (bandpass, laser line filter) to remove unwanted wavelengths. A filter wheel with neutral density filters allows for attenuation of the incident laser. Photons that are emitted from the sample are collected by a parabolic aluminium mirror. The high quality longpass filter, placed after the first mirror P1), removes the spectral reflection with an edge wavelength close to the incident laser energy. A second parabolic mirror focuses the emitted light onto an optical fiber that guides the emitted light into the spectrometer. Here, a spectrometer from Andor has been used. The spectrometer is equipped with an Si-CCD (200-1100 nm) and InGaAs-array (800-1600 nm) detector. The resolution depends on the chosen optical fiber and the choice of grating (100 lines/mm or 300 lines/mm grating).

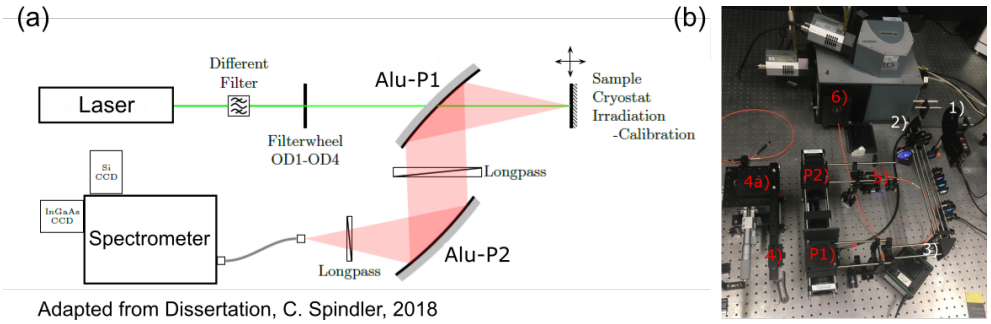

Figure 3.4: (a) Sketch of the photoluminescence set-up: The laser passes different filters before hitting the sample. The emitted light is collected by two parabolic aluminium mirrors and focused onto an optical fiber. The longpass filters remove the spectral reflection. The emitted light is analyzed by a spectrometer equipped with an Si and InGas detector. (b) Photograph of the PL set-up: 1) is a filter wheel to reduce laser power of the incoming beam. Before the sample the alignment is done by the mirrors 2) and 3). The sample holder 4) can be moved in xyz-direction 4a). The emitted light is collected by mirror P1) and P2) and focused on the optical fiber 5) and guided into the Andor spectrometer 6).

3.2.2 *Spectral corrections*

Each PL spectrum needs to be spectrally corrected for all optical elements and the detector used in the set-up. For the spectral correction, a calibrated halogen lamp from Avantes is used. The spectrum of that calibration lamp

$I_H^{cal.}$ is known. The correction function is given by dividing the known spectrum by the measured spectrum $I_H^{meas.}$.

$$f_{corr}(\lambda) = \frac{I_H^{cal.}}{I_H^{meas.}} \tag{3.1}$$

The measured spectrum is obtained by placing a spectralon diffuse reflectance standard with very high reflectivity at the sample position. Light of the halogen lamp is guided to the spectralon and then reflected into the set-up. For spectral correction, the correction function $f_{corr}(\lambda)$ is then multiplied with the actual measured photoluminescence spectrum.

$$I_{PL}^{corr.} = f_{corr.}(\lambda) \times I_{PL}^{meas.} \tag{3.2}$$

Measured and calibrated spectra must be given in the same spectral quantity (y-axis), typically in units of nm. After the correction, the y-axis of the PL spectrum can be converted into units of eV. Choice of filters, detector, optical fiber and grating have to be the same for the actual PL measurement $I_{PL}^{meas.}$ and the measurement of the halogen lamp $I_H^{meas.}$.

3.3 RAMAN SPECTROSCOPY

For a Raman scattering experiment, a monochromatic light (laser) is focused onto the sample by optical lenses. The scattered light is then analyzed for its different frequency components in a spectrometer. Raman scattering is a very weak process and the much stronger Rayleigh scattering needs to be removed by filtering elements. Because of their simplicity, notch or edge filters are used in many cases for this purpose. If the excitation frequency is changed, a filter based system requires the replacement of the filter with a filter that has exactly the right cut-off frequency for the laser line used in the experiment. For resonant Raman studies, a double or triple monochromator systems is the better choice. A monochromator based system allows for a tunable filtering of the Rayleigh scattering and therefore the system can be easily tuned to different laser lines. In this work, both a filter-based system as well as triple monochromator system have been used for the Raman characterization of $BiVO_4$. The resonant Raman studies were done with a triple monochromator system from Horiba. In this chapter, the two different systems are introduced and the importance of calibrating the Raman shift and absolute intensity is discussed.

3.3.1 *Confocal Raman microspectrometer from Renishaw*

Figure 3.5 shows a sketch of the confocal Raman microspectrometer InVia from Renishaw. The set-up is a filter-based system. Four lasers are connected to the set-up with the possible excitation wavelengths 325 nm, 442 nm 532 nm, 633 nm and 785 nm. The polarization of the incoming laser light can be changed with a $\frac{\lambda}{2}$-plate. The incoming laser light is guided with multi-

ple mirrors into the confocal microscope from Leica and focused onto the sample. The automated sample stage allows for mapping in the X-Y plane and for depth profiles in Z. The scattered light is then collected back by the microscope. At the spectrometer entrance, the very intense Rayleigh scattering and the specular reflection from the sample surface is removed by an edge filter. There is one edge filter for each of the 5 possible laser lines. To easily change between the laser excitations, four filters are pre-installed on a motorized filter wheel that is controlled by the software. By inserting $\frac{\lambda}{2}$-plate and/or a polarizer, scattered light of a certain polarization is selected. The grating separates the different energies of the scattered light before the light is imaged into the CCD detector. The Invia set-up from Renishaw is equipped with integrated silicon and a neon lamp for calibration of Raman shift (x-axis). A microscope enclosure ensures laser safety and reduces the background signal from surrounding light.

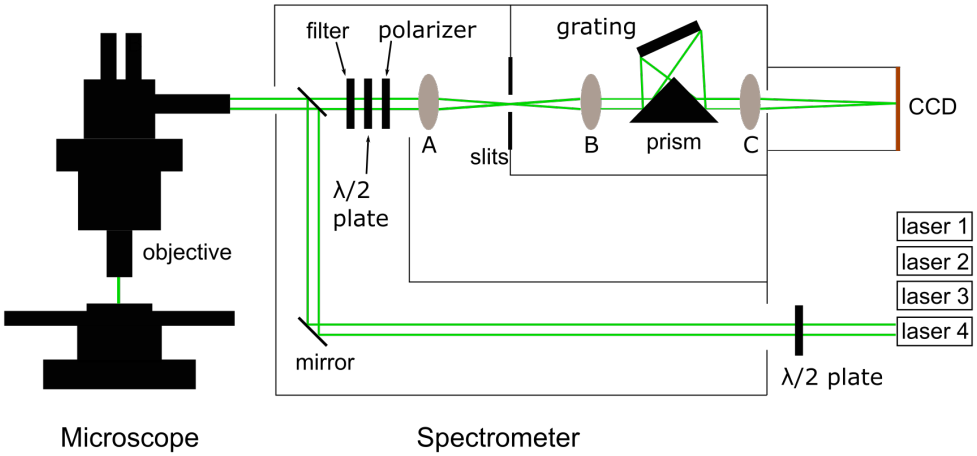

Figure 3.5: Sketch of the confocal Raman microspectrometer InVia from Renishaw that collects the scattered light with a Leica microscope. The spectrometer is equipment with filters, polarizing elements before and after the sample, prism and grating for light dispersion and a CCD detector.

3.3.2 *Triple stage spectrometer T64000 from Horiba*

For the resonant Raman studies in $BiVO_4$, we used the triple stage spectrometer T64000 from Horiba. The equipment used in this work belongs to the research group of Stephanie Reich, Freie Universität Berlin in Germany.

Figure 3.6 shows the design of the Raman spectrometer T64000 from Horiba with a laser source, a confocal microscope, a triple stage spectrometer and a CCD detector. For larger samples or liquid samples, there is the possibility to bypass the confocal microscope and use the macro-sample compartment instead. The advantage of a triple stage spectrometer is that it can be continuously tuned to the excitation laser light. Stage 1 and stage 2 act as a tunable filter to reject the Rayleigh light whereas stage 3 disperses the scattered light. The T64000 can be used in single stage mode, in triple additive or triple sub-

tractive mode. An additive mode gives the highest spectral resolution and high linear dispersion, whereas the subtractive mode gives a high stray light rejection and allows for collecting low-frequency Raman spectra down to $5\,\mathrm{cm}^{-1}$. In the triple subtractive mode, the polychromatic radiation enters Stage1 through the slit S1 and is dispersed by the grating G1. The slit Si1,2 at the entrance of Stage 2, selects a bandpass between $\lambda 1$ and $\lambda 2$. The grating G2 disperses the polychromatic radiation onto the slit Si2,3 that is limited to the spectral range between $\lambda 1$ and $\lambda 2$. In this way, the elastic scattered radiation is removed from the signal which is the main purpose of the stage 1 and stage 2. The polychromatic radiation selected by the pre-monochromator is then dispersed by the grating G3 and guided to the CCD detector.

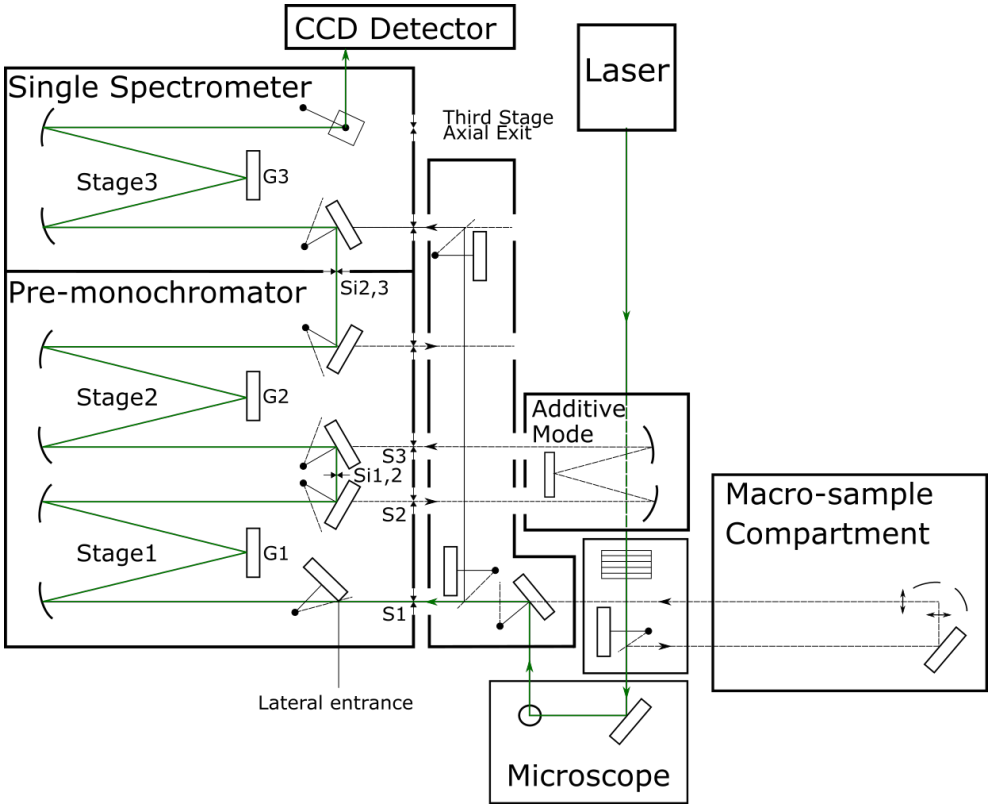

Figure 3.6: Design of the triple stage spectrometer T64000 from Horiba with a laser source, a confocal microscope or a macro-sample compartment, a triple stage spectrometer and a CCD detector. The triple stage spectrometer is equipped with gratings G1, G2 and G3 and multiple slits S.

The T64000 is connected to an argon-krypton (ArKr) laser from Innova with 12 laser lines from 458 nm to 647 nm and to a continuously tunable dye-laser covering the energy range from 580 nm to 785 nm.

3.3.3 *Polarized Raman and Porto's notation*

While standard Raman spectroscopy provides information on the sample composition, polarized Raman spectroscopy can provide further information on the symmetry of the vibrational modes and the orientation of the

sample. Porto's notation is used to record polarization conditions in a standardised manner. Porto's notation has the following form $A(BC)D$ and expresses the orientation of the crystal with respect to the polarization of the laser light in excitation direction and in the analysing direction. A is the propagation direction of the incident light, B is the polarization direction of the incident light, C is the polarization direction of the scattered light and D is the propagation direction of the scattered light. In backscattering geometry, the direction of the propagation of the incident and the scattered light is opposite, leading to $A(BC)\bar{A}$.

3.3.4 *Spectral corrections*

Most correction methods refer to the calibration of the frequency position. In a resonant Raman experiment, the change of Raman intensity as a function of excitation is of interest. In that case, the calibration of the Raman intensity is crucial. In the following, the different calibration methods with a strong focus on the calibration of the Raman intensity are explained.

3.3.4.1 *Calibration of frequency position*

If the primary quantity of interest is the Raman shift, calibration of frequency position is sufficient. The calibration of the frequency position requires the measurement of a known spectrum with sharp peaks at known frequency position. There are two common approaches to calibrate the x-axis of a Raman spectrometer. The first approach uses the emission lines of gases such as neon. [49] The second approach uses a reference scatterer with Raman bands at known wavenumber position. Materials that are often used are silicon with strong band at $520\,\mathrm{cm}^{-1}$ or diamond with a strong band at $1364\,\mathrm{cm}^{-1}$. Diamond is often used for calibration in the UV.

3.3.4.2 *Calibration of Raman intensity*

In literature, there are only a few examples of the absolute Raman cross section (benzene[54, 91]). In most examples, the Raman intensity is referenced to a transparent reference scatterer. This approach corrects for the spectral response of the equipment and the ω^4-dependency. In the following the procedure for the calibration of the Raman intensity by a transparent reference scatterer is described.

3.3.4.3 *Relative Raman intensity*

The Raman scattering cross section is measured in comparison with a transparent reference scatterer whose band gap is much higher than the measurement range. The Raman cross section of the sample is divided by the Raman cross section of the reference scatterer. Possible reference scatterer are calcite $CaCO_3$[41] with a band gap of 7 eV and several Raman lines (156, 283, 714,

1088, 1432 cm^{-1}) or quartz with a band gap in the same energy range. Another material that has been used widely in the literature [16, 57] is CaF_2 with only one Raman line at 321 cm^{-1} and a bang gap of 11 eV. The calibration requires a high quality crystal with very low defect concentration to exclude any resonant effects. Other examples are silicon[90], diamond[107] or liquid benzene[91].

3.3.4.4 *Correction for Bose-Einstein thermal occupation*

The Raman intensity given in Section 2.2.3.3 depends on the Bose-Einstein thermal occupation factor

$$n(\omega_s) = \frac{1}{exp(\hbar\omega_s/k_BT) - 1} \tag{3.3}$$

where ω_s describes the frequency of the scattered light, T the temperature and k_B the Boltzmann factor. When comparing intensities measured at different temperatures a correction of the Bose-Einstein factor $(n(\omega_s) + 1)$ is necessary.

3.4 INELASTIC NEUTRON SCATTERING

In a Raman scattering experiments we have only access to the phonons at the Brillouin zone (BZ) center. Inelastic neutron scattering allows for measurements of phonons outside the BZ center. The most important instrument to study neutron scattering is the triple-axis spectrometer (TAS).

3.4.1 *Thermal triple-axis spectrometer EIGER*

Figure 3.7(a) sketches the basic arrangement of the monochromator, the sample, analyzer and the detector in a triple-axis spectrometer. The triple-axis refers to the axes of rotation of the monochromator, the sample and the analyzer. Figure 3.7(b) shows a photograph of the triple-axis spectrometer EIGER at the continuous spallation neutron source SINQ at PSI, Villigen in Switzerland. The sample table, the analyzer and the detector can move on air-pressure to vary Θ_M,Θ_S and Θ_M.

EIGER is designed for experiments with thermal neutrons in the energy range from 1 to 100 meV. Figure 3.8 shows the design. The sapphire filters absorb neutrons with energies above 80 meV. After the sapphire filter, there are three rotatable steel cylinders in the neutron guide that are used as neutron beam shutters. The virtual source reduces the background signal before the neutron beam enters the monochromator PG_{002} with the massive shielding. The shielding is made of tungsten-paraffin composite[37] and reduces the γ- and fast neutron radiation as well as the neutronic background which can hit the sample or the detector system. The monochromator selects neutrons of a certain wavelength and focuses the neutron beam onto the sample. Figure 3.7(b) shows the PG_{002} monochromator that consists of 15 lamellas with

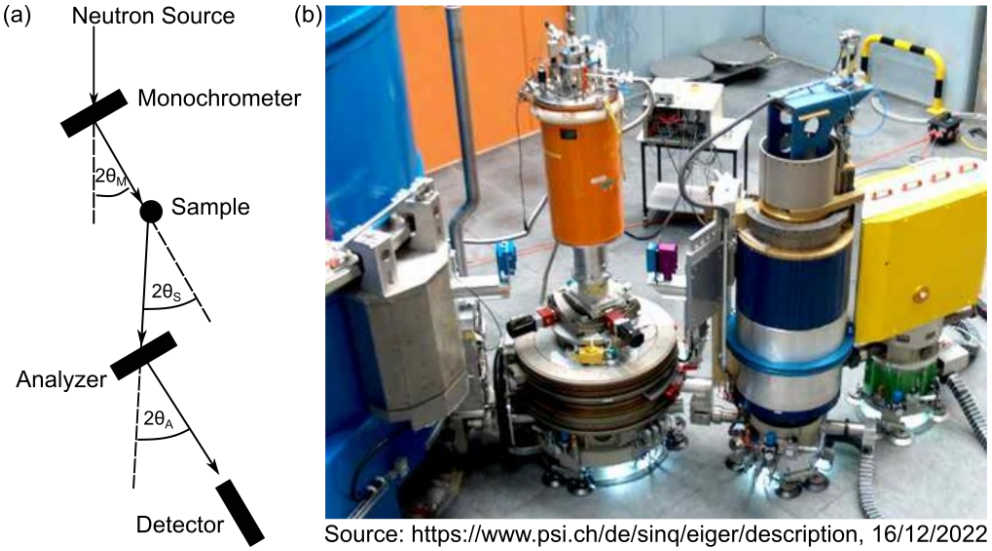

Figure 3.7: (a) The photograph shows the blue shielding of the monochromator, the sample table, the blue shielding of the analyzer and yellow detector housing. (b) Sample table, analyzer and detector can move on air-pressure to vary the angles Θ_M,Θ_S and Θ_M .

9 pyrolytic graphite (PG) crystals each.[97] The design is similar to the Multi-Analyzer Crystal Spectrometer (MACS) reported in [93] in which the vertical focusing of the neutron beam is achieved by bending and the horizontal focusing by rotating the lamella. The sample is mounted onto the sample table which can be rotated and tilted for proper alignment of the crystal axis with respect to the incident beam. The sample table can be equipped with furnace for high temperature measurements, cryostat for low temperatures, pressure cells or magnetic cells. The PG_{002} analyser has option for horizontal focusing only. The detector is a single He^3-tube.

3.5 SAMPLE ENVIRONMENT

3.5.1 *Linkam microscope stage THMS600*

Temperature dependent measurements have been done with the Linkam temperature stage THMS600 which covers temperatures from 80 K to 870 K, see Figure 3.9(a). The Linkam stage is designed so that it can be easily positioned on a microscope stage. In this work, the Linkam stage has been used with the Renishaw Raman microscope and the IR-Vis Microspectrometer from Jasco. Figure 3.9(b) shows the Linkam stage positioned in the Jasco microspectrophotometer. The sample is placed on a silver heating block with high thermal conductivity inside the cell. The quartz glass at the top and a small hole in the center of the silver block ensures full optical characterization of the sample including transmittance measurements. The temperature is regulated by resistive heating of the silver block. For temperatures from

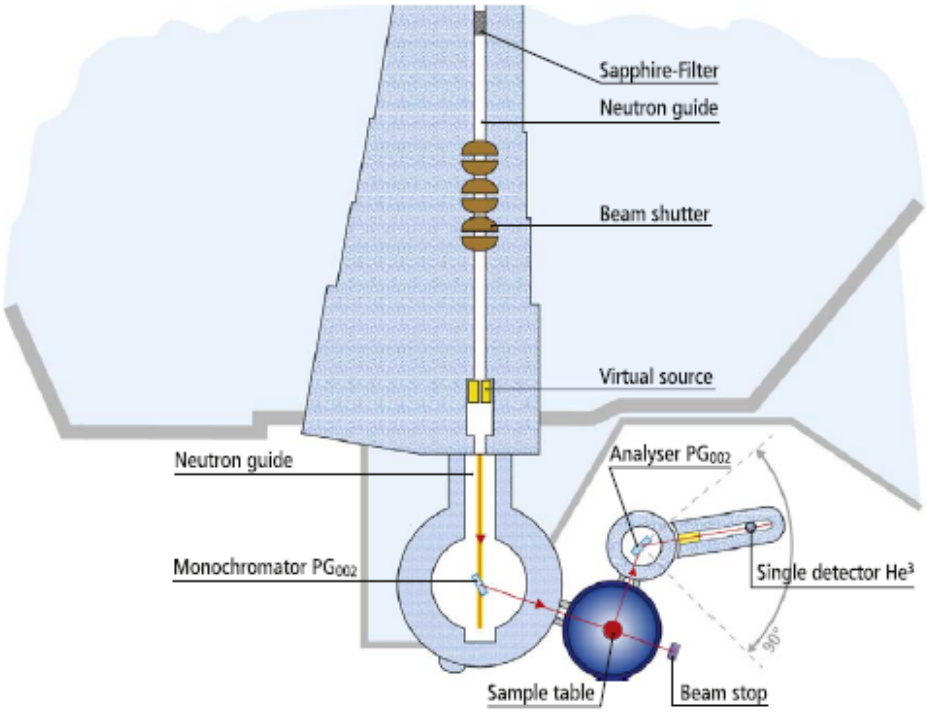

Figure 3.8: Sketch of the triple-axis spectrometer EIGER at PSI, Villigen in Switzerland, taken from Ref. [97]

80 K to RT, the stage is cooled by liquid nitrogen. At high temperatures, a water cooling prevents from overheating of the metal casing body.

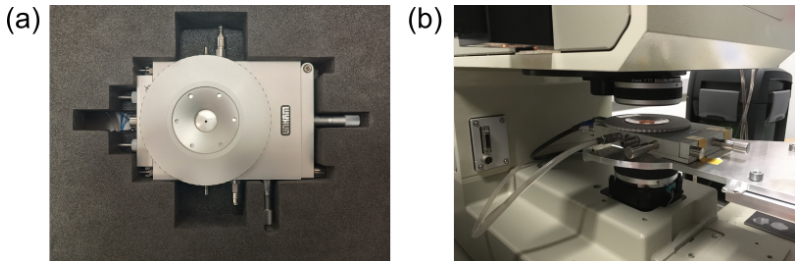

Figure 3.9: (a) Linkam temperature stage THMS600 with quartz glass window at the top. The sample is positioned onto a ceramic block inside the Linkam stage. A small hole in the ceramic block allows the light to pass for transmittance measurements. (b) Photograph showing the Linkam stage positioned in the Jasco microspectrophotometer for transmittance measurements.

3.5.2 *Oxford Instruments helium flow cryostat Microstat HiRes*

Helium flow cryostat from Oxford Instruments Microstat HiRes was used to cover the low temperature range from 5 K to 300 K. Figure 3.10(a) shows a typical set-up for a low temperature experiments using liquid helium. Liquid helium is pumped from the cryogen storage dewar into the transfer tube

and then into the cryostat. The helium gas exiting the cryostat is used to cool the shielding of the transfer tube to reduce the overall helium consumption. The sample is placed inside the cryostat in vacuum environment. Because of the vacuum environment there is little risk for ice formation on the sample. The temperature in the cryostat is regulated by MercuryiTC controller that controls the helium gas flow and the heating element in the cryostat. A window at the top of the cryostat allows the incident radiation to enter and interact with the sample. The cryostat is installed on a platform to minimise vibrations and sample drift, see Figure 3.10(b).

(a)

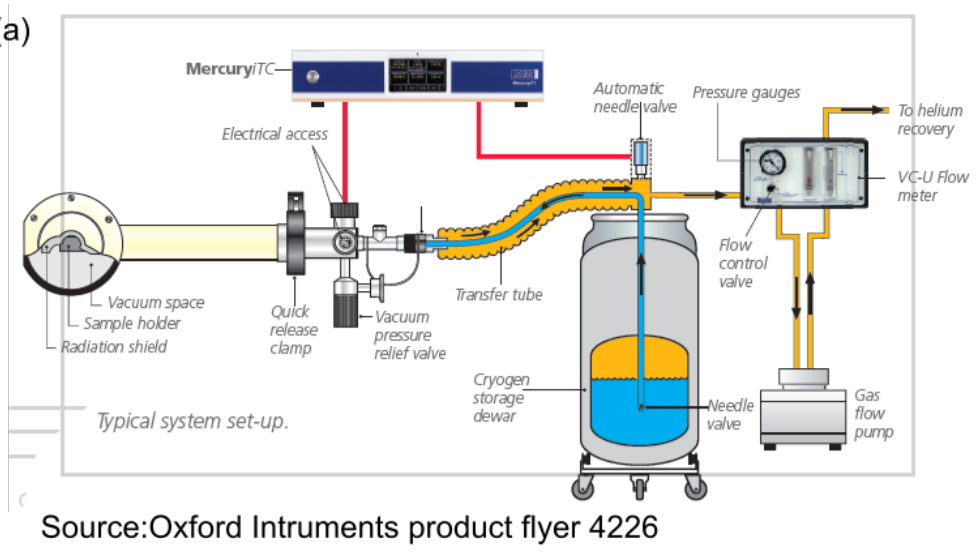

Source:Oxford Intruments product flyer 4226

(b)

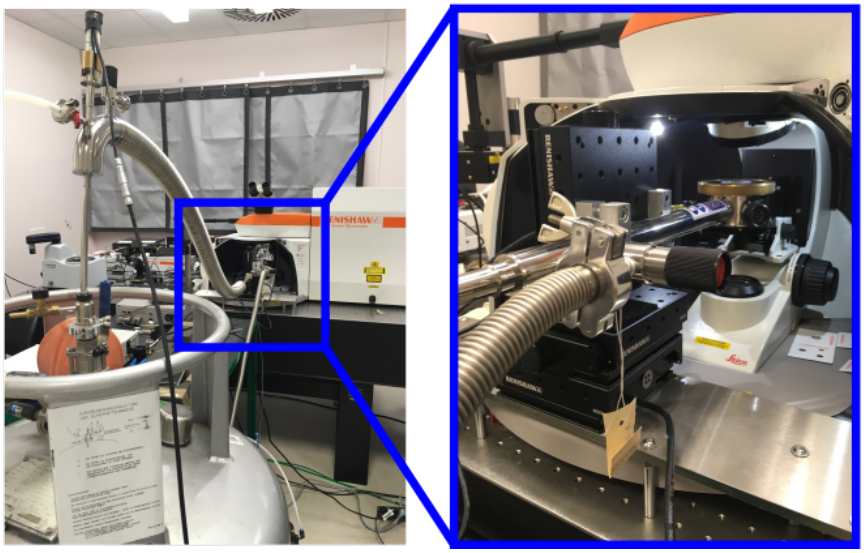

Figure 3.10: (a) Set-up for low temperatures measurements with the helium cryostat. (b) Photograph showing the helium cryostat inserted in the Renishaw Raman spectrometer.

4

LATTICE DYNAMICS IN BISMUTH VANADATE

This chapter shows the characteristic lattice vibrations and discusses the lattice dynamics in $BiVO_4$. After a presentation of the $BiVO_4$ crystal structure, we will discuss the Raman spectrum in the low-temperature monoclinic and in the high-temperature tetragonal phase. Afterwards, we will discuss new results. First, we will discuss the coupling of two Raman modes that is strongly temperature and polarization dependent. Then, we will present first findings on the lattice dynamics observed by inelastic neutron scattering.

4.1 CRYSTAL STRUCTURE OF BISMUTH VANADATE

The purpose of this section is to introduce the crystal structure of $BiVO_4$ and to define all the crystallographic directions that are used throughout the thesis. Figure 4.1(a) shows the schematic representation of the tetragonal unit cell of $BiVO_4$ that is valid at high temperatures above the phase transition temperature T_c but also largely relevant at temperatures below T_c since the monoclinic distortion is relatively small in the case of $BiVO_4$. The oxygen atoms are shown in red and the vanadium cation (V^{5+}) is positioned in the center of a oxygen tetrahedron. The bismuth cation (Bi^{3+}) is colored in violet. The crystallographic axes are indicated in the figure. Throughout the manuscript, all indications of orientations are given with respect to the tetragonal unit cell. Figure 4.1(b) shows a view on the (001) surface. From this view, it can be easily seen that the tetragonal unit cell has a 4-fold rotational axis parallel to the $[001]$-axis. The 4-fold rotational axis is called the principal axis. The phase transition is driven by a spontaneous shear strain developing in the ab-plane. In the monoclinic phase, the angle γ inbetween the a and the b-axis deviates from $90°$. The view on the (110) surface is given in Figure 4.1(c) in which the principal axis is labeled with c and the $(1\bar{1}0)$-axis with b'. The direction $[110]$ pointing out of the surface plane is labeled with a'. For this research work, we used single crystals of different surface orientations, there are (001), (110) and (100).

4.2 RAMAN SCATTERING IN BISMUTH VANADATE

In this section, we show the Raman spectrum of the low-temperature monoclinic and the high-temperature tetragonal phase. We assign all the observed modes and compare their frequencies to the values reported in literature. The Raman modes in $BiVO_4$, their frequency position and their evaluation across the phase transition as a function of temperature and pressure are known from literature. The main purpose of this chapter is to evaluate the crystal quality by checking whether the Raman modes and their frequency

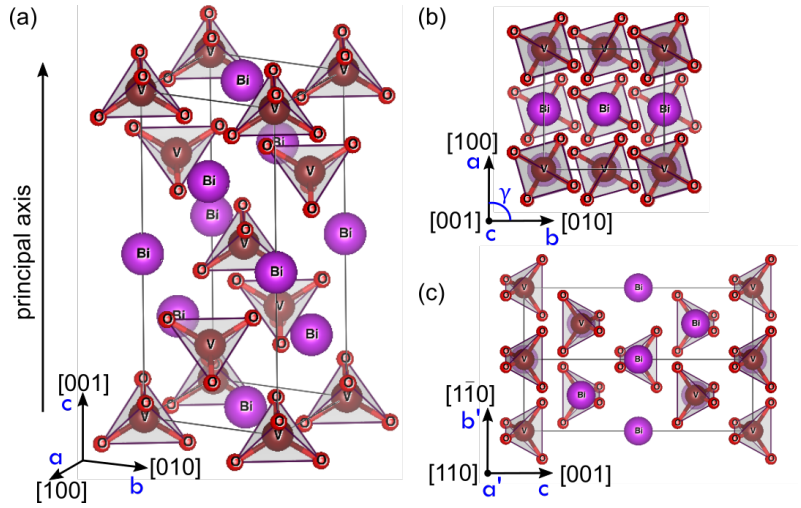

Figure 4.1: (a) Schematic representation of the tetragonal unit cell of bismuth vanadate. (b) View on the (001) surface and (c) view on the (110) surface are also given.

position matches the literature values. Besides, the chapter is an introduction to the characteristic features of the Raman spectrum of $BiVO_4$ to the reader.

4.2.1 *Sample description and measurement details*

For the measurement of the Raman spectra in the monoclinic and the tetragonal phase, we used different single crystal samples, namely *BVO110-Tim* and *BVO110-Mael* with surface orientation (110) and *BVO001-Andreas* with surface orientation (001). The Raman signal was measured with the Raman spectrometer InVia from Renishaw, described in Section 3.3.1, using a laser excitation of 633 nm (1.96 eV). For the low-temperature measurements, the samples were placed in the Oxford Instrument cryostat described in Section 3.5.2. For the characterization at temperatures above room temperature, the Linkam temperature stage described in Section 3.5.1 was used.

4.2.2 *Raman mode assignment*

A standard symmetry analysis shows that 13 and 18 Raman active modes are expected in the high-symmetry tetragonal and low-symmetry monoclinic phase respectively.[7] Table 4.1 summarizes the accessible modes for the different samples and different polarization configurations in the tetragonal and in the monoclinic phase.

First, we will assign the Raman modes in the low-temperature monoclinic phase. In the monoclinic phase only modes of A_g and B_g symmetry are expected. Figure 4.2 shows the Raman spectra measured at 10 K and at room temperature for different scattering geometries. All 8 A_g modes are successfully observed in the parallel polarization geometries. Their eigen-

Table 4.1: Description of the samples, their orientations and the Raman modes accessible in different polarization configurations. All orientations are given with respect to the principal axis c.

Sample	scattering geometry	Tetragonal	Monoclinic
Samples (001):	$c(aa)c$ and $c(bb)c$	$3A_g$+$5B_g$	$8A_g$
BVO-Andreas, *BVO-Thomas*	$c(ab)c$ and $c(ba)c$	$5B_g$	$8A_g$
Samples (110):	$a'(cc)a'$	$3A_g$	$8A_g$
BVO-Tim, *BVO-Mael*	$a'(b'b')a'$	$3A_g$+$5B_g$	$8A_g$
	$a'(cb')a'$ and $a'(b'c)a'$	$5E_g$	$10B_g$

frequencies are given in Table 4.2 and compared to values reported in literature.

Table 4.2 provides also the eigen-frequencies for the different Raman modes from density functional theory (DFT) calculations. The calculation of the lattice vibrations by DFT in the case of $BiVO_4$ is not trivial and requires the use of heavy hybrid functionals. This might be the reason why we found only one calculation on $BiVO_4$ from Pellicer-Porres[71] in the literature so far. Because of the little details on the calculation, our collaborator D. Vincent repeated the calculation on $BiVO_4$. From his experience, the crystal structure shows deviations from the real crystal structure despite the use of the time expensive hybrid functionals. The deviations are in particular reflected in the monoclinic angle and might cause errors on the eigen-frequencies of the low frequency modes.

According to the Table 4.1, B_g modes are expected in cross polarization geometries for a sample with (110) surface orientation. We observed 8 out of 10 expected B_g modes together with A_g modes leaking into the spectra. The leaking of A_g modes is explained by their strong intensity and the imperfections of the polarization conditions in the experiment. The eigen-frequency of each vibration mode has been extracted from the spectra by fitting the data with multiple Lorentzian functions. The eigen-frequencies are given in Table 4.2 and their values are compared to the literature. We do not have experimental values for the B_g^1 and the B_g^7 values for the following reasons. The expected frequency position of the B_g^1 mode is relatively low with $47\,cm^{-1}$. A measurement at low frequencies requires a modification of the experimental set-up that allows us to measure energies very close to the Rayleigh energy line. In the case of the B_g^7 mode, we found several A_g modes in the same frequency range leaking into the spectrum. Most probably, the Raman band of the B_g^7 mode is experimentally hidden by the intensity coming from A_g modes in the same frequency range. When it comes to cases like these, a theoretical calculation of the lattice vibrations and their frequency positions would help to make a mode assignment.

Second, we assigned the Raman modes in the high-temperature tetragonal phase. Figure 4.3 shows the Raman spectra of tetragonal $BiVO_4$ measured at 570 K with different polarization geometries. We could clearly assign two out

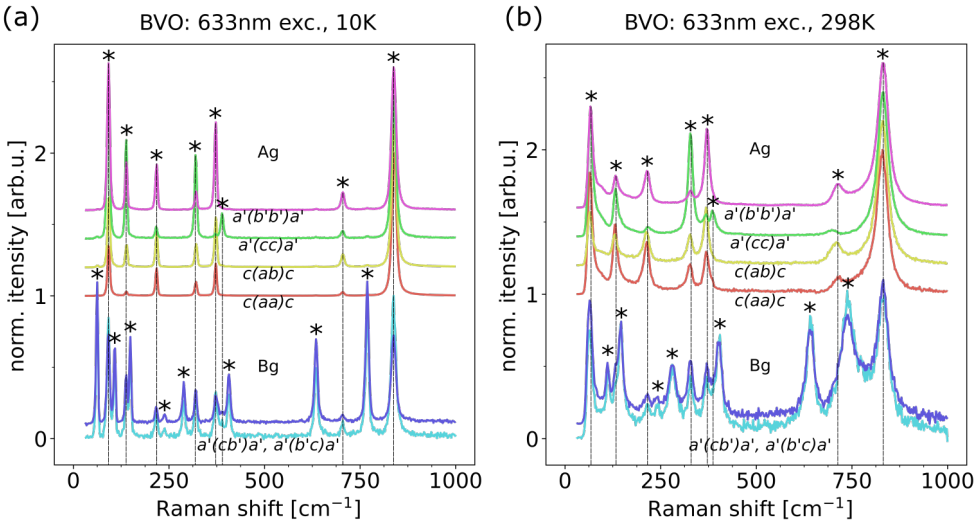

Figure 4.2: Raman spectra of the single crystal sample *BVO110-Tim* and *BVO001-Thomas* measured at T=10 K in various polarization geometries with a laser excitation of 633 nm. All spectra are normalized to the A_g^8 mode at 838 cm^{-1}.

Table 4.2: Raman eigen-frequencies assigned to the active Raman modes with A_g and B_g symmetry. The eigen-frequency is an average from the values extracted by Lorentzian fitting of the data shown in Figure 4.2 which were measured at different scattering geometries. The Raman eigen-frequencies are in good agreement with the values reported in literature. *phonon-phonon coupling observed: error on the estimation of the eigen-frequency by Lorentzian fitting is expected for the room temperature data

monoclinic bismuth vanadate						
Mode	ω_{10K}	ω_{300K}	Exp. Ref.[7]	Exp Ref.[71]	DFT Cal. Ref.[71]	DFT Cal. Ref.[106]
A_g^1	92	66	62	-	64	68
A_g^2	139	131*	130	129	136	140
A_g^3	217	213	212	213	214	226
A_g^4	321	325	326	327	339	332
A_g^5	372	370	370	369	364	354
A_g^6	389	387	386	383	389	393
A_g^7	705	702*	711	708	760	747
A_g^8	839	830	830	831	870	839
B_g^1	-	-	47	-	43	56
B_g^2	62	-	55	-	47	69
B_g^3	108	111	110	111	123	160
B_g^4	149	145	144	141	149	164
B_g^5	239	242	-	241	250	280
B_g^6	289	280	280	276	278	308
B_g^7	-	-	-	-	392	402
B_g^8	407	402	400	400	400	411
B_g^9	635	641	642	641	700	701
B_g^{10}	769	741	743	747	770	758

of three A_g modes, four out of five B_g modes and three out of 5 E_g modes. The assignment at high temperatures is more difficult due to the Raman modes broadening. A full assignment of all modes in the tetragonal phase could be completed by temperature and pressure dependent measurements as it has been done by Pellicer-Porres et al.[71]. The overall goal of this work was to measure resonant Raman profiles at room temperature so the focus here was on the mode assignment in the monoclinic phase and not so much in the tetragonal phase.

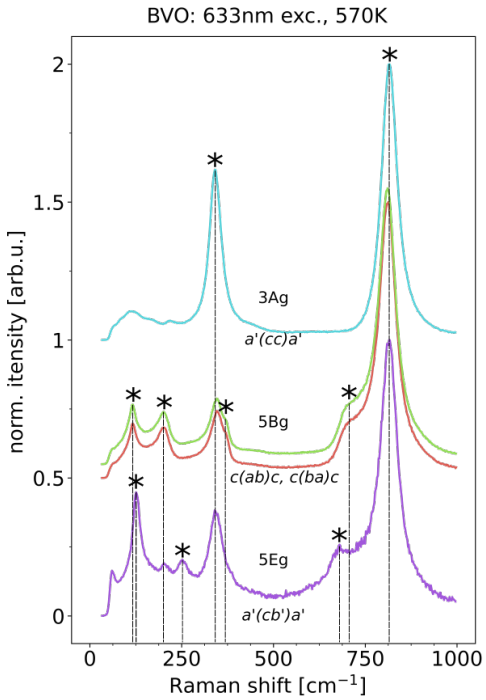

Figure 4.3: Polarized Raman spectra of *BVO110-Mael* and *BVO001-Andreas* at 570 K measured with 633 nm laser excitation. All spectra have been normalized to the $A_{g,tet}$ mode at 816 cm^{-1}.

4.3 PHONON-PHONON COUPLING IN BISMUTH VANADATE

For most of the observed Raman phonon modes in $BiVO_4$, the lineshape is well described by a Lorentzian function over a large temperature range. However, strong anomalies are observed for the A_g^7 mode at 700 cm^{-1} and the A_g^2 mode at 130 cm^{-1}. In this section we show that the frequency position of the A_g^7 mode strongly depends on the temperature and on the polarization conditions in the experiment. We discuss the origin of these anomalies and apply the damped harmonic oscillator model over large temperature range.

4.3.1 *Sample description and measurement details*

In this study, we investigated the Raman spectra of $BiVO_4$ single crystals over a large temperature range. We used the two samples *BVO110-Tim* and *BVO110-Mael*, both with (110) surface orientation. In the surface plane, we found the principle axis [001] and the crystallographic axis $[1\bar{1}0]$ that is perpendicular to the principal axis for both samples. All crystallographic directions are given with respect to the tetragonal unit cell. For simplicity reasons, we label the crystallographic directions [110], $[1\bar{1}0]$ and the principle axis [001] with a', b' and c, respectively. The Raman spectra were measured with the Renishaw Raman spectrometer described in Section 3.3.1 using the red laser of 633 nm (1.96 eV) for the excitation. We use Porto's notation to define the light propagation and polarization with respect to the crystallographic axes a', b' and c. For the low temperature measurements, we used the cryostat from Oxford Instruments. The measurement set-up for low-temperatures is described in detail in Section 3.5.2. For temperatures above room temperature, the Linkam microscope stage was used, details are given in Section 3.5.1.

4.3.2 *Results*

4.3.2.1 *Overview of the spectrum and evidence for coupling phenomena*

Figure 4.4 shows the phonon modes A_g^7 and A_g^8 measured at (a) 200 K and (b) room temperature with a 633 nm laser excitation for two polarization conditions. The first observation we made on the raw data is that the maximum intensity of the A_g^7 mode occurs at very different frequencies depending on the polarization condition for both temperatures. The data were fitted with a model based on two Lorentzian oscillators, which is shown by dotted lines, and with the coupled oscillators model, which is indicated by black dashed lines. The fitting parameters are given in Table 4.3. ω_7, ω_8 and Γ_7, Γ_8 are the eigen-frequency and the damping of the A_g^7 and the A_g^8 mode, respectively. The coupling is described by Γ_{78} in the coupled oscillators model. First, we will discuss the modeling with the classical Lorentzian model. At 200 K the Lorentzian model provides a good fit to the data. In contrast, the Lorentzian model fails to describe the lineshape of the A_g^7 mode at 300 K. There are

two reasons for that: first the lineshape of the A_g^7 is asymmetric and second there is intensity inbetween the two modes. For the fitting and only at 300 K, we fixed the eigen-frequency of the A_g^7 to the frequency position of its maximum intensity. Without any constraint on the fitting parameters, the algorithm does not converge and locates the Raman band of the A_g^7 mode at a frequency position far away from its maximum intensity. Now, we will discuss the fitting parameters in more details. The eigen-frequency of the A_g^8 mode is the same for both polarization conditions and for both temperatures. However, the eigen-frequency of the A_g^7 mode is very different from one polarization condition to the other at 300 K. This is surprising because in a first approximation, there is no physical explanation why the eigen-frequency of a Raman band would change from one polarization condition to another.

Next, we will discuss the modeling with the coupled oscillator model. For the coupled oscillators model we assumed that the eigen-frequency and the damping coefficient has to be the same for both polarization geometries. Further we assumed the real part of the coupling parameter Δ to be zero. At 200 K, both models, the Lorentzian and the coupled oscillators model, provide a good fit to the data. This is also true for the high intensity A_g^8 phonon mode for both polarization conditions at both temperatures. The overall lineshape is well described by both models and the frequency position as well as the damping coefficient of the A_g^8 mode is nearly identical for the both models. The major improvement is found for the A_g^7 mode at 300 K. The coupled oscillators model succeeds to describe the asymmetry in the lineshape of the A_g^7 mode as well as the increased intensity inbetween the two modes. This is especially true for the polarization condition $b'(a'a')\bar{b}'$. The coupling coefficients are very different from one polarization condition to the other. For $b'(cc)\bar{b}'$, the imaginary part of the coupling parameter Γ_{78} is positive which corresponds to a repulsion of the two phonon modes involved in the coupling. For $b'(a'a')\bar{b}'$, the imaginary part Γ_{78} is negative leading to an attraction of the two phonon modes.

In summary, we saw that the classical Lorentzian model fails to describe the asymmetric lineshape of the A_g^7 mode. The asymmetric lineshape is well described by the coupled oscillators model that suggests phonon-phonon coupling between the A_g^7 and the A_g^8 mode that seems to be strongly temperature and polarization dependent.

4.3.2.2 *The coupled oscillators model and its temperature dependence*

In this section, we will extend the coupled oscillators model to a large temperature range and study the temperature dependence of the coupling parameter Γ_{78}. Figure 4.5(a) shows the A_g^7 and the A_g^8 mode measured as a function of temperature for the polarization condition $b'(a'a')\bar{b}'$. Figure 4.5(b) shows a zoom on the A_g^7 mode measured for the polarization condition $b'(cc)\bar{b}'$. The black dashed lines are fits based on the coupled oscillators model. For both polarization conditions, the data are well described by the coupled oscillators model from low temperatures up to the phase transition at 523 K.

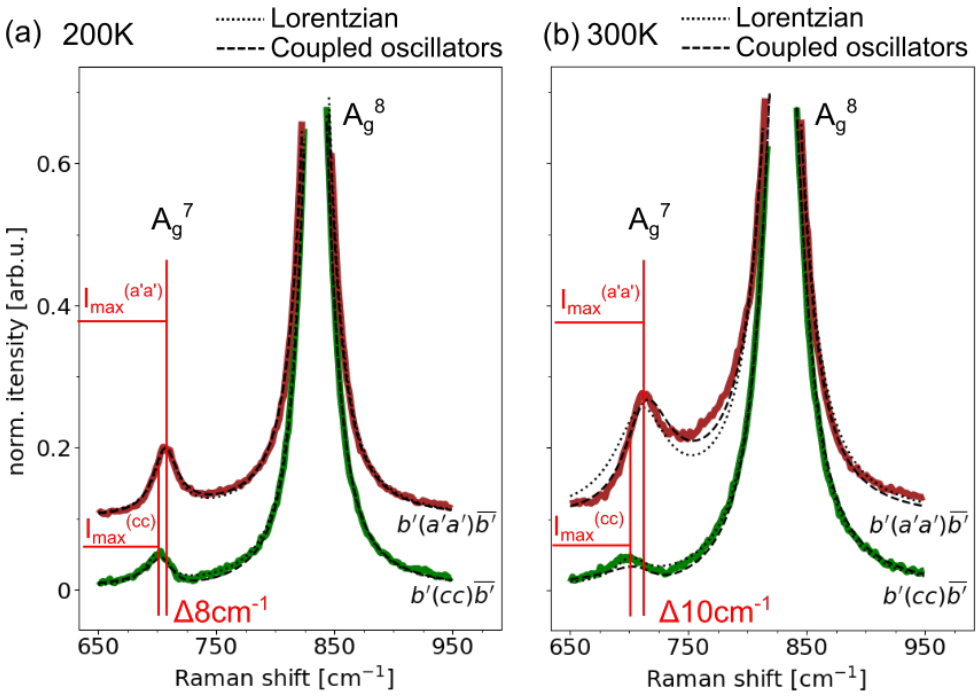

Figure 4.4: High frequency modes A_g^7 and A_g^8 measured at different polarization geometries $b'(cc)\bar{b}'$ and $b'(a'a')\bar{b}'$ at (a) 200 K and (b) 300 K. Dotted lines show the fits assuming two Lorentzian oscillators, the dashed lines show the fit based on the coupled oscillators model. The fitting parameters for both models are given in Table 4.3.

Table 4.3: Comparison of fitting parameters between the classical Lorentzian model and coupled oscillator model at 200 K and 300 K. Here, the real part of the coupling Δ is fixed to zero.

	200K		**300K**	
	$b'(a'a')\bar{b}'$	$b'(cc)\bar{b}'$	$b'(a'a')\bar{b}'$	$b'(cc)\bar{b}'$
Lorentzian model				
ω_7	708	700	711 (fixed)	701 (fixed)
Γ_7	24 (5%)	22 (9%)	54 (8%)	31 (12%)
ω_8	834	835	830	830
Γ_8	26	26	36	34
Coupled oscillators model				
ω_7	706		712	
Γ_7	25.5		47.0	
ω_8	835		831	
Γ_8	26.2		34.9	
Γ_{78}	-5.3	12.3	-15.0	22.4

The coupled oscillators model is overparameterized so that assumptions on the fitting parameters have to be made. A detailed discussion on the coupled oscillators model and the overparameterization is found in Section 2.2.3.6. First, we assumed the individual damping Γ_7, Γ_8 to increase linearly with temperature at a constant slope of 0.09 and 0.08, respectively. This approximation is perfectly acceptable at temperatures above 100 K. At low temperatures, the damping as well as the eigen-frequency saturates which is typically modelled by the so called *Klemens* model.[61, 119] Second, we assumed the coupling parameter Δ to be zero.

The intensity of the A_g^7 mode is extremely weak compared to the intensity for the A_g^8 mode. This is especially true for high temperatures and the polarization condition $b'(cc)\bar{b}'$. Because of this extreme intensity difference, the minimization algorithm had the tendency to optimize the model to the high intensity A_g^8 mode with large errors on the low intensity A_g^7 mode. Therefore, we had to find a solution to compensate for this huge intensity difference. That is why we introduced a *weight* equal to the inverse of the intensity in the minimization algorithm. The weight is introduced as a multiplication factor so that $weight * (data - fit)$ is minimized by the least-squares minimization method. The intensity difference is not as drastic for the light polarization $b'(a'a')\bar{b}'$, so that in this case the *weight* is equal to one.

We still encountered difficulties to apply the coupled oscillators model over the whole temperature range for the $b'(a'a')\bar{b}'$ polarization condition. We found ambiguous temperature trends for the mode coupling parameter and the eigen-frequency of the low-intensity A_g^7 mode. Also here we had to find a solution. Especially at high temperatures, we see a significant amount of the Raman intensity inbetween the individual Raman modes that originates from the coupling. This intensity increases with increasing temperatures with respect to the intensity contribution from the individual modes. That is why we expect a strong temperature dependence of the coupling parameter. Also the Raman band of the A_g^8 mode shifts strongly with increasing temperatures so we expect a strong temperature dependence in its eigen-frequency. In contrast, the frequency position of the A_g^7 mode does not vary strongly with temperature. With the purpose to find a unique temperature trend for the coupling parameter, we assumed the eigen-frequency of the A_g^7 to be constant as a function of temperature. The fitting results assuming constant eigen-frequency are shown in Figure 4.5(b). This non-standard assumption was only applied for the light polarization $b'(a'a')\bar{b}'$.

Figures 4.6(a) and (b) show the eigen-frequencies ω_7 of the A_g^7 mode and ω_8 of the A_g^8 mode as a function of temperature for the two polarization conditions, respectively. The data points above the phase transition are included and symbolized with a cross. These data points have been obtained by simple Lorentzian fits since no coupling is expected in the high-temperature tetragonal phase. The eigen-frequency ω_8 of the high-intensity A_g^8 mode strongly decreases about 3% with increasing temperature for both polarizations. At the phase transition T_c, the eigen-frequency ω_8 is continuous which is characteristic for a 2nd-order phase transition. Because of the strong inten-

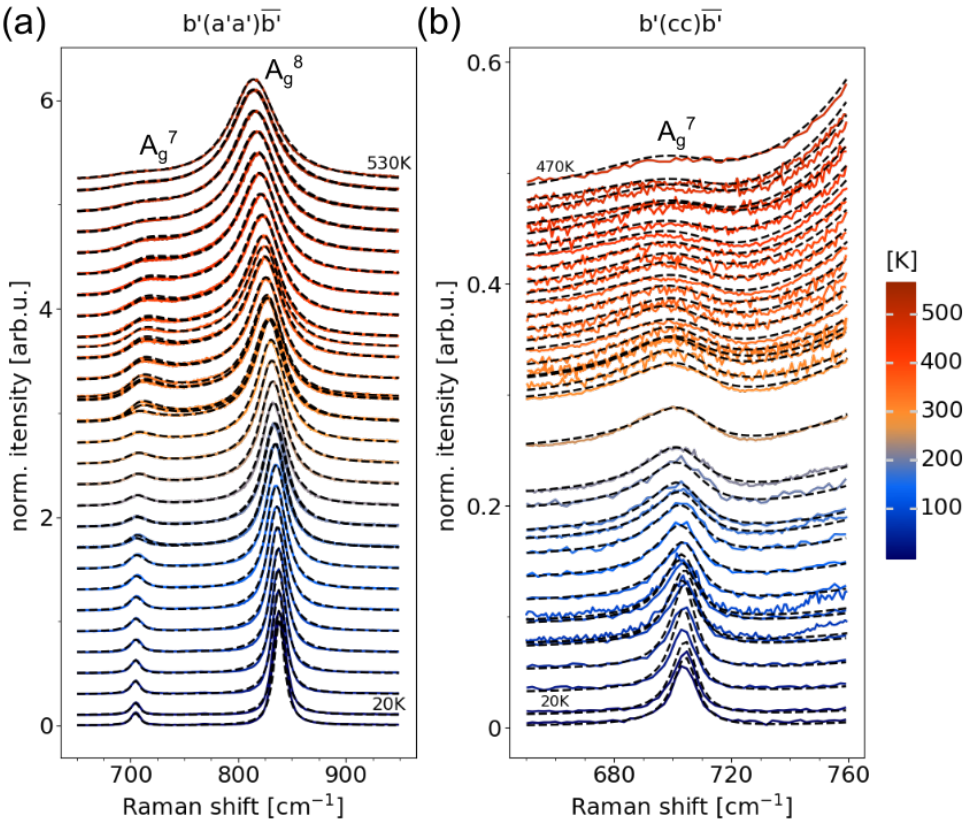

Figure 4.5: Coupled oscillators model applied to the Raman modes A_g^7 and A_g^8 at different temperatures for the polarization conditions (a) $b'(a'a')\bar{b}'$ and (b) $b'(cc)\bar{b}'$. Here, the real part of the coupling Δ is assumed to be zero. The damping of the individual oscillators Γ_7 and Γ_8 is assumed to increase linearly with temperature. Only for the polarization condition $b'(a'a')\bar{b}'$, the eigen-frequency ω_7 is assumed to be constant.

sity of the A_g^8 mode, the temperature trend of the eigen-frequency ω_8 of the A_g^8 mode is generally robust against different assumptions on the coupling.

As discussed previously, we assumed a constant eigen-frequency of 705 cm^{-1} for the light polarization $b'(a'a')\bar{b}'$. The value of 705 cm^{-1} is an average value that we obtained by fitting the temperature data for the other light polarization $b'(cc)\bar{b}'$. For this light polarization, the eigen-frequency of the A_g^7 is constant over a large temperature range, before the value slightly increases by $\approx 1\%$ while approaching the phase transition. At the phase transition, we see a small step in the eigen-frequency which we believe is in the range of expected error because of the low intensity of the A_g^7 mode.

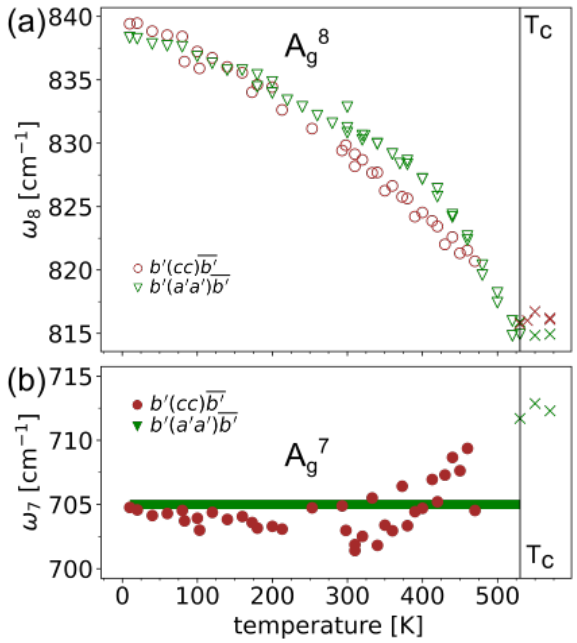

Figure 4.6: Eigen-frequencies (a) ω_7 of the A_g^7 mode and (b) ω_8 of the A_g^8 mode for the two polarization conditions as a function of temperature obtained from the coupled oscillator model.

Figure 4.7(a) shows the coupling parameter Γ_{78} while Figure 4.7(b) shows the ratio of the oscillator strengths ratio P_7/P_8 as a function of the temperature for the polarization condition $b'(cc)\bar{b}'$ and $b'(a'a')\bar{b}'$. Interestingly, the coupling parameters are of opposite sign depending on the polarization condition. In the polarization condition $b'(cc)\bar{b}'$, the coupling parameter is positive and increases continuously with increasing temperatures. In the other scattering geometry, the coupling parameter is negative. At very low temperatures, the coupling parameter has small positive values. We believe that this value is still reasonably small indicating that the coupling can be neglected at these temperatures. In the polarization condition $b'(a'a')\bar{b}'$, the absolute value of the coupling parameter Γ_{78} increases with increasing temperatures up to 400 K before the absolute value decreases again. The ratio of the oscillator strengths P_7/P_8 decreases while approaching the phase transition for both polarization conditions. That is consistent with the observation on the

raw data, where the intensity of the A_g^7 is extremely weak at high temperatures at which the A_g^8 mode dominates.

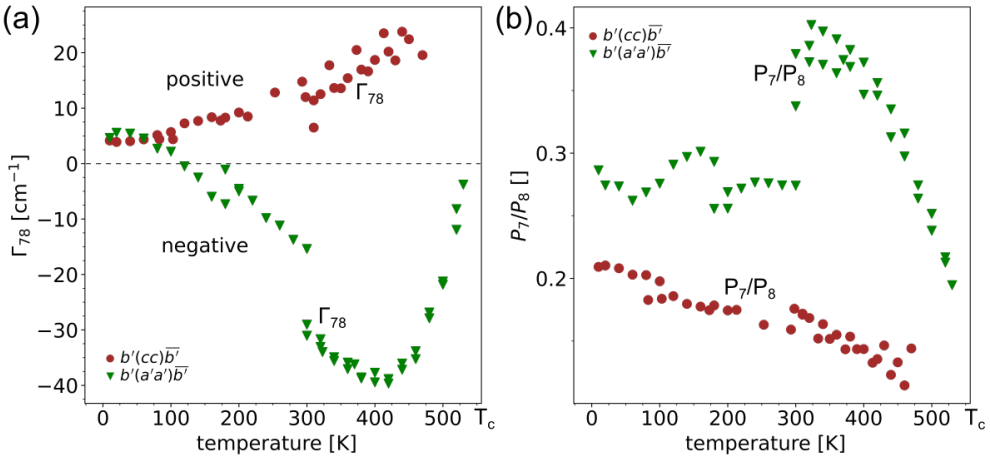

Figure 4.7: (a) Coupling parameter Γ_{78} and (b) oscillator strengths ratio P_7/P_8 as a function of temperature for the polarization conditions $b'(cc)\bar{b}'$ and $b'(a'a')\bar{b}'$ obtained from the coupled oscillators model.

4.3.3 *Discussion*

Chaves et. al [20] demonstrated that only phonon modes of the same symmetry can couple. In $BiVO_4$, we found a nice example that illustrates this concept. In the monoclinic phase, we observed a coupling between the A_g^7 and the A_g^8 mode that is strongly temperature and polarization dependent. At the phase transition, the A_g^7 changes its symmetry to a B_g symmetry while the A_g^8 remains of A_g symmetry. As a consequence, no coupling is expected in the high-temperature tetragonal phase and this is reflected in an unusual temperature trend in the coupling parameter for the light polarization $b'(a'a')\bar{b}'$. The absolute value of coupling parameter Γ_{78} first increases up to 400 K before it decreases again. This is explained by the following. According to the selection rules, modes of A_g and B_g symmetry are allowed in the tetragonal phase for this light polarization condition. Due to the change in symmetry of the A_g^7 mode, no coupling is expected in the tetragonal phase and that is why the coupling parameter has to decreases while approaching the phase transition.

The picture is very different for the other light polarization $b'(cc)\bar{b}'$. In this light polarization condition, only modes of A_g symmetry are allowed in the tetragonal phase. Therefore, the Raman intensity of the A_g^7 mode decreases with increasing temperature. At the phase transition, the A_g^7 mode disappears because of its change in symmetry. For the coupling parameter we observed a continuous increase with increasing temperature.

One difficulty in our case is the large difference in intensity of the two modes. While the intensity of the A_g^8 mode is very strong, the intensity of the A_g^7 mode gets very weak while approaching the phase transition. To

overcome this difficulty, we introduced a weight into the fitting algorithm that compensates for the huge intensity difference between the two modes.

The limitation of the coupled oscillator model is clearly its overparametrization. Because of the overparametrization, a good prior knowledge of the modeling system is required that allows you to define meaningful physical constraints. In addition, a verification of the modelling parameters is recommended for example at multiple temperatures. We used a data set recorded over a large temperature range and at different polarization conditions. The temperature trend of the eigen-frequency of the high-intensity mode A_g^8 mode is robust against different physical constraints. However, the temperature dependence of the lineshape of the A_g^7 mode is either reflected in the temperature dependence of its eigen-frequency or in the coupling parameter. The variation of the eigen-frequency over the whole temperature range is maximum $7\,\mathrm{cm}^{-1}$. This is calculated from the low-temperature value of $705\,\mathrm{cm}^{-1}$ and the value of $712\,\mathrm{cm}^{-1}$ at the phase transition in the tetragonal phase. This variation is relatively small compared to the temperature variation of $25\,\mathrm{cm}^{-1}$ observed in the eigen-frequency of the A_g^8 mode. For the purpose of finding a robust solution for the temperature dependence of the coupling parameter, we assumed a constant eigen-frequency of the low-intensity A_g^7 mode. We believe this assumption is acceptable because of the relatively small variation of maximum $7\,\mathrm{cm}^{-1}$ (1%) across the whole temperature range.

4.4 INELASTIC NEUTRON SCATTERING

In the last section, we show preliminary results from inelastic neutron scattering experiments. At the moment, nothing is known on the optical phonons outside of the Brillouin zone center. The goal of this experiment was to measure for the first time the optical phonon branches across the phase transition and thereby contribute to a better understanding of the lattice dynamic across the phase transition.

4.4.1 *Sample description and measurement details*

Inelastic Neutron scattering (INS) measurements were performed using the triple-axis spectrometer EIGER. The $BiVO_4$ single crystal was purchased from SurfaceNet, Rheine in Germany. Figure 4.8(a) shows a photograph of the crystal with a size of roughly 15 mm by 15 mm and mass of 2.856 g. Figure 4.8(b) shows a binocular picture of the single crystal cleavage plane (010) with the typical domain structure and the (001) surface. The $BiVO_4$ single crystal was mounted onto a steel grid and placed inside a furnace with the [110] and [001] axes in the scattering plane. The furnace temperature is monitored with a thermocouple at the bottom of the furnace.

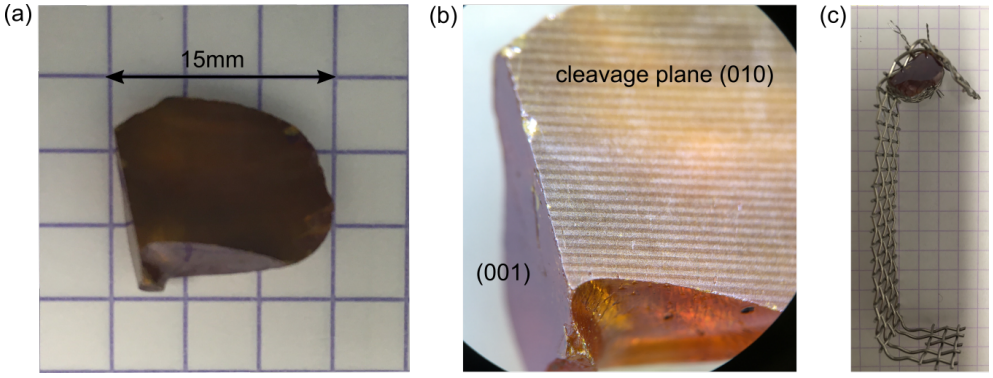

Figure 4.8: (a) Photograph of the $BiVO_4$ single crystal *Urs* (b) Binocular picture of *Urs* showing the cleavage plane (010) with its domain structure and the (001) plane (c) sample *Urs* mounted on a steel grid

4.4.2 *Results*

Figure 4.9 shows the phonon dispersion measured along the $[hh\bar{8}]$ direction at a furnace temperature of 528 K. We clearly observe the acoustic phonon and its dispersion, confirming the results of Tomeno et al. [101]. In addition, we observe one optical phonon at 9.5 meV and its dispersion. Slightly lower in energy we observe another optical phonon mode at 6 meV. Its optical branch shows an anomalous intensity behaviour. The intensity at the Brillouin zone center is very weak and gains intensity moving away from the zone center. We also notice in Figure 4.9 an anomalous intensity variation on the acoustic branch with very high intensity at the Brillouin zone center

and a drop in intensity at QH=0.2. The anomalous intensity variations of the acoustic branch and of the optical branch slightly higher in energy might be caused by coupling effects between the two branches.

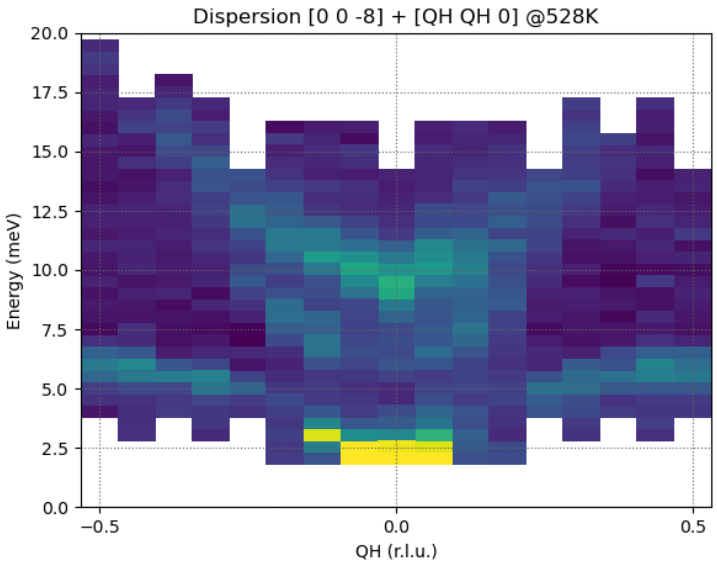

Figure 4.9: Phonon dispersion of $BiVO_4$ measured along $[hh\bar{8}]$ on the triple-spectrometer EIGER and a furnace temperature of 528 K.

Figure 4.10 shows INS spectra measured at $[00\bar{8}]$ at different furnace temperatures fitted with three Gaussians. The optical phonon O2 shifts from 10.68 meV down to 9.5 meV at high temperatures while the O1 seems to be constant over temperature. We carried out measurements of the full dispersion between $[\frac{\bar{1}}{2}\frac{\bar{1}}{2}\bar{8}]$ and $[00\bar{8}]$ and found similar pictures.

4.4.3 *Discussion*

The first results from the neutron scattering experiment were very encouraging for the following reasons. First, the data showed two optical phonon modes and its dispersion that have not been reported in literature so far. Second, we observed intensity variations within the acoustic branch and in one of the two optical branches that suggest coupling effects. Third, the data show strong shifts in the optical phonon E^2_{opt} that indicates a softening towards the phase transition. These observations were a good basis to formulate research questions that will be addressed in a follow-up experiment. The first question is what are the corresponding lattice vibrations for the optical phonon O1 and O2. Here, the DFT calculations from our collaborator D. Vincent will help us in assigning these features. Another important information that might help for a conclusive assignment would be a detailed temperature study across the phase transition for the optical branches. Second, we would like to understand the origin of the anomalous intensity variations. For this, data with a better q-resolution would be desirable to investigate the dip in the intensity for the acoustic and the optical branch slightly higher in energy.

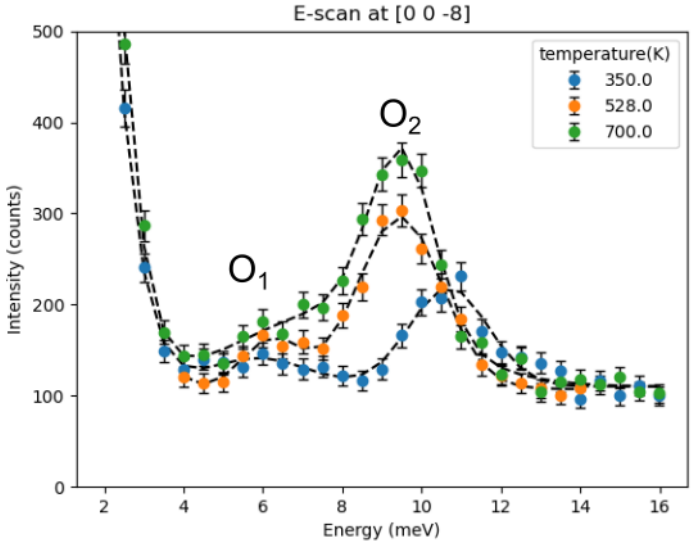

Figure 4.10: Neutron scattering spectra measured at $[00\bar{8}]$ at 350 K, 528 K and 700 K. The dashed lines are Gaussian fits to the data. The optical phonon O2 clearly shifts with temperature.

To address these research questions, a follow-up experiment was proposed to the PSI neutron source with the request to repeat the experiment with a more detailed temperature dependence and a better q-resolution.

4.5 CONCLUSION

In $BiVO_4$ we found an example of a phonon-phonon coupling. We show that the phonon-phonon coupling is the origin of the asymmetric lineshape of the A_g^7 mode at high temperatures. Further, we demonstrate that the coupling strength is first of all strongly temperature dependent and secondly, strongly depends on the polarization condition. Depending on the polarization condition, the sign of the coupling parameter is either positive or negative, referring to either repulsion or attraction of phonon modes. The coupling strength, expressed in the absolute value of the coupling parameter, increases with increasing temperatures. At temperatures above 400 K, the coupling strength decreases for the $b'(a'a')\bar{b}'$ polarization condition. This is explained by the change in symmetry of the A_g^7 mode, which leads to decoupling of the two phonon modes above the phase transition temperature.

We observed the acoustic phonon and its dispersion in agreement with the publication from Tomeno et al.[101] In addition, we measured two optical phonons and their dispersion; one at 6 meV and one at 11 meV at the Brillouin zone center and at T=350 K. We observed anomalous intensity variations of the acoustic and of the optical branch at slightly higher energies that suggest mode coupling of the acoustic branch with the optical branch.

In summary, the Raman modes of $BiVO_4$, their symmetry, their eigenfrequency and their evolution across the phase transition are very well known. However, looking into the details, we discovered particular features such as mode coupling effects. For our research goal, which targets to use resonant Raman scattering as a technique for probing electronic transitions, the implication of these features have to be carefully evaluated. The relevance of these implications is minor if we work at moderated temperatures and if we concentrate on these Raman modes that are well approximated by a simple Lorentzian function.

4.6 PERSPECTIVES

We observed mode coupling effects for the A_g^2 and A_g^3 mode at low frequencies that are strongly temperature dependent and polarization dependent, similar to the observations made for the A_g^7 and A_g^8 mode at high frequencies. The origin of the mode coupling effects at low frequencies has to be verified. The modeling of the coupling effects at low frequencies is more difficult for two reasons. First, we observe an additional broad band whose origin is not clear at the moment. Its intensity, its frequency position and its band width are strongly temperature dependent. Second, the intensity of the soft A_g^1 mode is very strong in comparison to the modes of interest (A_g^2 and A_g^3). The intensity of all these modes are overlapping so modeling of the coupling not only requires a model for the A_g^2 and A_g^3 but also a numerical description for the high-intensity soft mode A_g^1 and the additional broad band.

The inelastic neutron scattering leaves a number of open questions. What is the origin of the optical phonon mode slightly above the acoustic phonon? Is mode coupling the origin of the anomalous intensity variations in the branches of the optical and acoustic phonon modes? What is the detailed temperature dependence of the optical phonon at higher energies that shows softening at high temperatures? To answer these questions further measurements are required with better q-resolution and at various temperatures. Accurate calculations of the dynamical structure factors and scattering function would help to assign the features observed so far. Calculating $BiVO_4$ from first principles is not easy and requires the expensive calculations with hybrid functions.

CONTRIBUTIONS

Thank you to D. Vincent from the University Rennes for his first-principles calculations on the IR and Raman modes in $BiVO_4$.

I would like to thank C. Toulouse for her guidance and her support for the low-temperature measurements with the helium cryostat. Setting up and operating the Raman spectrometer with the helium cryostat requires know-how and patience. Thank you to G. Gordeev for his feedback and critical questions on data analysis of the phonon-phonon coupling.

Many thanks to T. Fennell and U. Stuhr from PSI, Villingen in Switzerland for their support and guidance to perform a neutron scattering experiment on a 'small' $BiVO_4$ single crystal.

5 OPTICAL AND ELECTRONIC PROPERTIES

UV/Vis spectroscopy and photoluminescence are classical techniques to study electronic transitions in a semiconducting material. In this Chapter, we apply these techniques to scheelite $BiVO_4$ single crystals and discuss their limitations. In the first part of this Chapter, we measured the absorption edges as a function of temperature and quantified the optical anisotropy by UV/Vis spectroscopy. We show that the optical absorption is sensitive to the ferroelastic phase transition and is dominated by the evolution in ferroelastic shear strain.

In the second part of this chapter, we discuss the origin of the broad PL band observed in photoluminescence measurements. Characterizations as a function of temperature, incident light polarization and laser power suggest that the PL band originates from a defect level. We found no evidence for a PL emission from a band-to-band transition.

5.1 OPTICAL ABSORPTION IN BISMUTH VANADATE

Parts of the work presented in this section have been published in APL Materials 8, 081108 (2020) under a Creative Commons Attribution (CC BY) license.[47] Major parts in the following sections are identical in content and word with the publication. The text that is identical in words with the publication is placed in between the following symbols ★/..../★.

5.1.1 *Sample description and measurement details*

We used two single crystals that were obtained by the Czochralski-method. Both samples were polished from both surface sides with the purpose to obtain parallel surface planes and to eliminate the diffuse reflectance from each surface. The first sample has a surface orientation (110) and a thickness of 360 µm; the second sample has a (001) oriented surface and a thickness of 100 µm, see Figs. 5.1(a) and 5.1(b). For the measurement of the transmittance and reflectance we used the Jasco MSV-370 microspectrophotometer which is presented in detail in section 3.1.2. The samples were placed in a Linkam THMS600 heating stage, details see section 3.5.1. For the (110)-oriented sample and the (001)-oriented sample the measurement areas were set to $400 \times 400\,\mu m^2$ and $300 \times 300\,\mu m^2$, respectively, by using an aperture. We took great care to position the measurement area on the sample in a region which is free of domain walls or surface cracks. For all reflectance measurements, we used an aluminium mirror for the calibration.

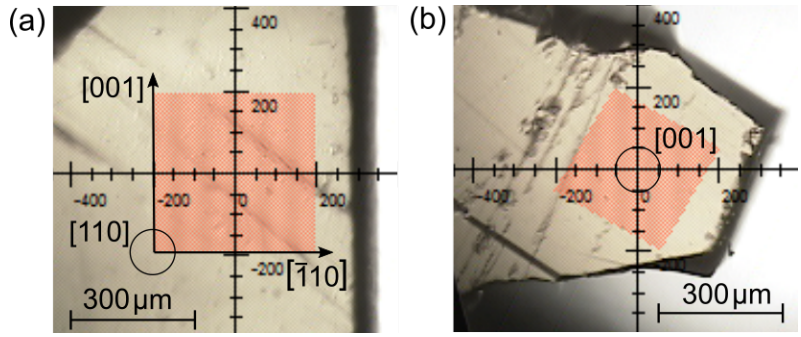

Figure 5.1: Optical microscopy images of (a) the (110)-oriented sample and (b) the (001)-oriented sample. For both samples, optical measurements were done with a vertical and a horizontal light polarization. The measurement areas are highlighted in red. Figure adapted from the publication [47].

5.1.2 *Results*

5.1.3 *Absorption coefficient and Tauc method*

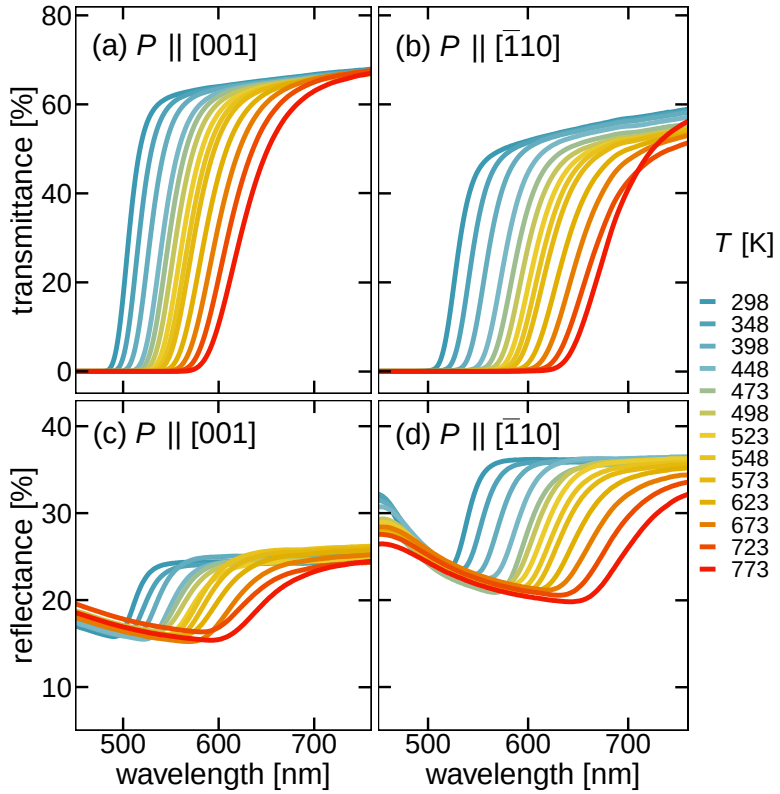

Figure 5.2: Transmittance spectra measured on the (110)-oriented sample (a) for $P \parallel [001]$ and (b) for $P \parallel [\bar{1}10]$ as a function of temperature. (c) and (d) Reflectance spectra for $P \parallel [001]$ and $P \parallel [\bar{1}10]$ respectively. The figure has been published in [47].

★/ We first discuss the results for the (110)-oriented sample. Experiments were performed with two different directions of the linear light polarization P: first, with P parallel to the crystallographic axis [001] and second with $P \parallel [\bar{1}10]$, see Fig. 5.1(b). The sample showed clearly visible domain walls that could be used to facilitate a visual alignment and confirm the sample orientation[23]. The data are shown in Fig. 5.2. For both light polarization directions, reflectance and transmittance data show a pronounced temperature dependence, with an absorption edge shifting to longer wavelengths as temperature increases. To investigate the nature of the band gap and its possible change with temperature, the absorption coefficient was calculated /★ with the Equation 2.24 given in Section 2.2.1.1. Figs. 5.3(a) and 5.3(b) show the absorption coefficient as a function of temperature for both light polarization directions. The theory of interband optical absorption reveals that the absorption coefficient α varies with the photon energy according to the well-known relation $(\alpha h\nu)^n = A(h\nu - E_{\text{opt}})$ which has been described in detail in Section 2.2.1.2. The exponent n characterizes the nature of the transition that dominates the optical absorption. The nature of the band gap can then be derived from the Tauc plot by plotting $(\alpha h\nu)^n$ versus the photon energy $h\nu$. Details on the Tauc method and the Tauc plot are given in Section 2.2.1.2. For a direct transition, the data are described by a straight line for $n = 2$ and in case of an indirect transition for $n = 0.5$. The optical absorption edge E_{opt} is then given by the intercept of the linear fit with the photon-energy axis.

★/ Figs. 5.3(c) and 5.3(d) show the Tauc plots for both light polarizations assuming indirect ($n = 0.5$) and Figs. 5.3(e) and 5.3(f) for direct ($n = 2$) transition. In all four cases, the data can be described by a straight line making it difficult to conclude on the nature of the transition with this measurement alone. Considering the similar curve shape of the absorption coefficient at each temperature, there are no indications that first, the nature of the transition differs from one to the other light polarization and secondly, that the nature of the transition changes with temperature. Following the recent conclusions by Cooper et al. on the indirect nature of the band gap, we extract an energy for the absorption edge of 2.27 eV for $P \parallel [\bar{1}10]$ and of 2.39 eV for $P \parallel [001]$ at room temperature./★

5.1.3.1 *Anisotropy of the optical absorption*

★/ In a next step, we investigated the anisotropy of the optical absorption. To analyze the data without having to rely on any particular hypothesis on the nature of the band gap, we define the absorption edge as the inflexion point of the transmittance curve. We determined this point by fitting the first derivative of the transmittance curve with an asymmetric Gaussian function. This function was chosen because it produces a satisfactory fit for all data and provides a consistent analysis, although we do not claim any particular physical meaning for it. The results are shown in Fig. 5.4. In a first approximation, the evolution of the absorption edges was fitted linearly, with separate fits above and below T_c. Fig. 5.4(a) shows the absorption edge obtained

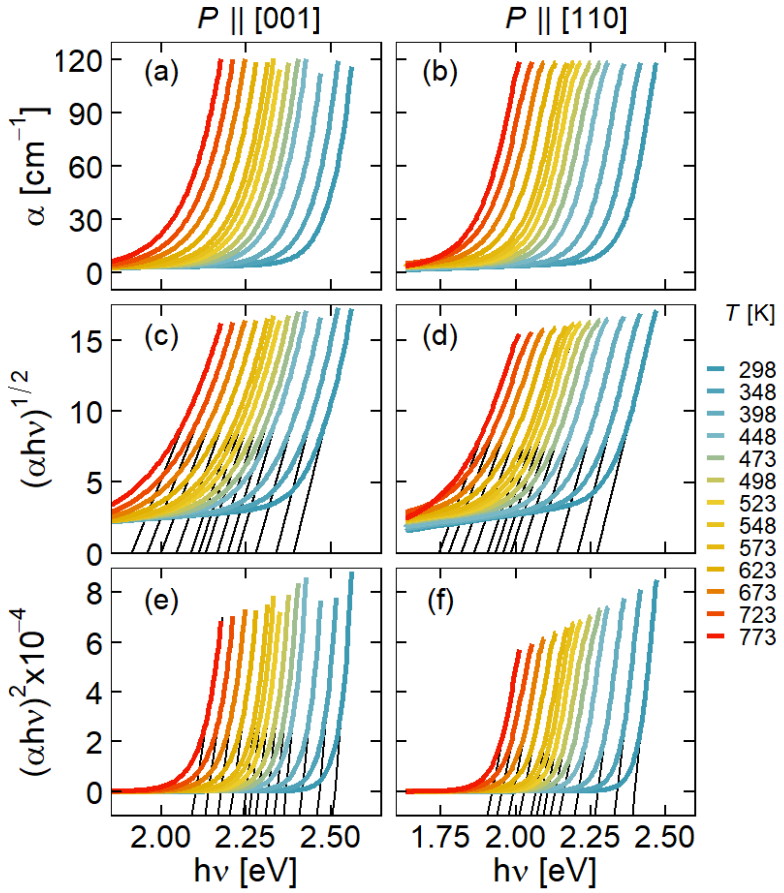

Figure 5.3: (a), (b) Optical absorption coefficient calculated from transmittance and reflectance data of the (110)-oriented sample for $P \parallel [001]$ and $P \parallel [\bar{1}10]$, respectively. (c), (d) and (e), (f) Tauc plots calculated for both polarization directions, assuming an indirect and a direct band gap, respectively. The figure has been published in [47].

for the (110)-oriented sample for both polarizations. We notice, first, that the absorption is clearly anisotropic in the tetragonal phase, with an energy difference of $\approx 0.2\,\mathrm{eV}$ between the two polarizations. This difference remains constant for temperatures above T_c, and the absorption edge decreases at the same rate of $\approx -0.85\,\mathrm{meV\,K^{-1}}$ for both light polarizations. Second, we observe a clear kink at T_c in the temperature evolution of the absorption edge for both light polarizations. Below T_c, in the monoclinic phase, the evolutions for both light polarizations remain linear, albeit with different slopes. This demonstrates that the absorption edge is sensitive to ferroelastic strain. These findings are robust even if alternative methods to extract the absorption are used./★ The corresponding plots are provided in the Appendix A.

5.1.3.2 *Optical anisotropy in the monoclinic* (001)*-plane*

★/ In the monoclinic phase, the optical absorption is expected to be anisotropic also in the plane perpendicular to the principal axis. To estimate the magnitude of this anisotropy, we performed a similar experiment with the (001)-

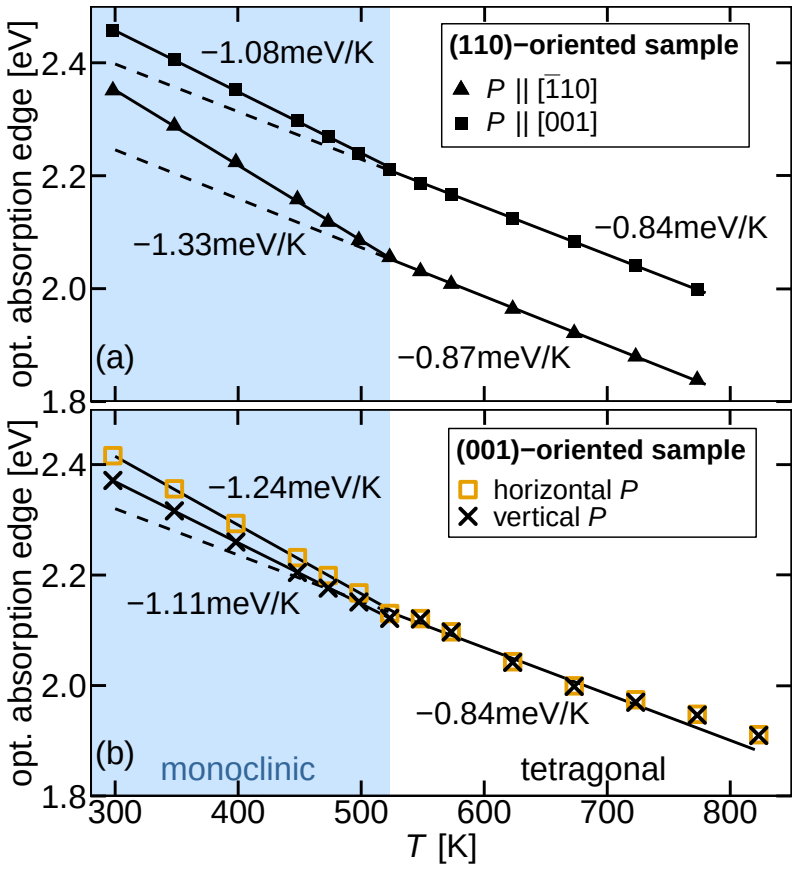

Figure 5.4: Temperature dependence of the optical absorption edge for (a) the (110)-oriented sample and (b) the (001)-oriented sample. The solid lines are fits to the data. The dashed lines are extrapolations of the high temperature trend into the low-temperature region. The figure has been published in [47].

oriented sample. We first measured the transmittance at room temperature, at a fixed wavelength of 515 nm, as a function of polarization direction. We chose 515 nm because it is close to the absorption edge and therefore we expected significant difference in transmittance for different polarization directions. Fig. 5.5 shows the transmittance at 515 nm as a function of polarization direction P. The sample was aligned in such a way that the maximum transmittance occurred close to the horizontal P and the minimum at vertical P. The position of the sample is shown in the inset of Fig. 5.5. The evolution of the transmittance is fitted with a sinusoidal function.

Then the transmittance spectra were measured over the full wavelength range for the vertical and horizontal light polarization. The difference in absorption edges measured in this configuration amounts to 45 meV at room temperature. Transmittance spectra were also collected with increasing temperature, and the corresponding absorption edges are shown in Figure 5.4(b). The energy difference decreases with increasing temperature and vanishes at T_c, as expected from the tetragonal symmetry./★ The difference in the absorption edge should be considered as a first estimation, because the birefrin-

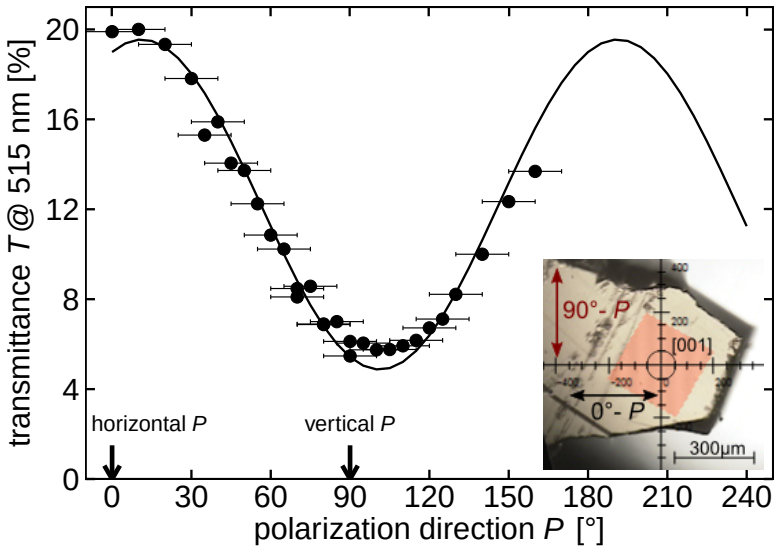

Figure 5.5: Transmittance as a function of polarization direction, measured at a fixed wavelength of 515 nm and at room temperature on the (001)-oriented sample. The figure has been published in the supplementary information of [47].

gence is neglected here. By neglecting the effect of birefringence we assume that the incident light polarization remains linear while the light is transmitted trough the sample. In fact, the anisotropy in the refractive index causes a change in the light polarization from linear to elliptical. However, the experiment shows that the anisotropy in the (001)-plane is relatively small, so that the fundamental band gap is found for light polarized perpendicular to the principal axis, at room temperature and above.

5.1.3.3 *Optical absorption is sensitive to shear strain*

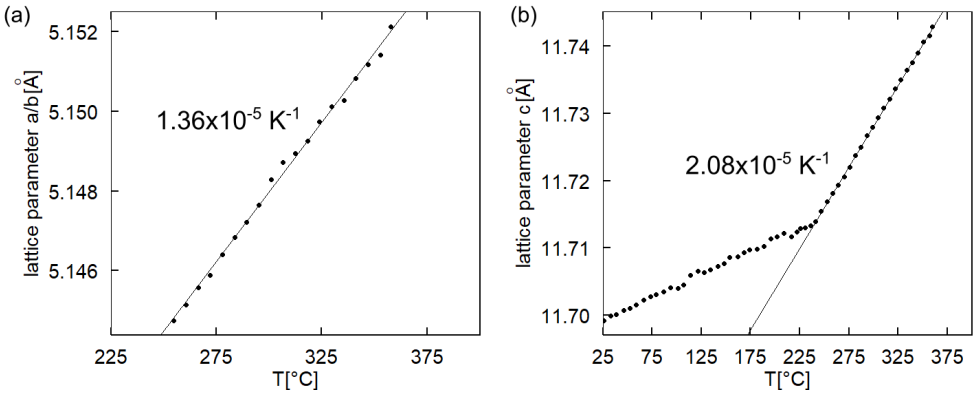

Figure 5.6: Evolution of the lattice parameter (a) *a*,*b* and (b) *c* across the phase transition. The solid lines are linear fit to the data taken from David and Wood [30]. The tensor coefficient $\alpha_{11}^{\text{tetra}}$ and $\alpha_{33}^{\text{tetra}}$ are given in (a) and (b), respectively.

★/ Having established that the optical absorption is clearly sensitive to the ferroelastic transition, it is insightful to decompose the observed variations of the absorption edges as a function of the different components of strain. For that purpose, we use the detailed knowledge of the volume, lattice constants and strains across the phase transition in Ref. [30], and focus here on the (110)-oriented sample. Figure 5.8(a) shows the evolution of the unit-cell volume across the phase transition and the corresponding volumetric thermal expansion coefficients. /★ The volumetric thermal expansion coefficient is defined by:

$$\alpha = \frac{1}{V}\frac{\mathrm{d}V}{\mathrm{d}T} \tag{5.1}$$

The volumetric thermal expansion coefficient for the tetragonal and monoclinic phases can directly be estimated by using the experimental data presented in Figure 5.8(a). We consider the volume to change linearly with temperature in both phases and therefore assume linear trends above and below T_c

$$\alpha^{\mathrm{mono}} = \frac{1}{V_0}\left.\frac{\mathrm{d}V}{\mathrm{d}T}\right|_{\mathrm{mono}} = 1.4 \times 10^{-5}\,\mathrm{K}^{-1} \quad \text{and} \tag{5.2}$$

$$\alpha^{\mathrm{tetra}} = \frac{1}{V_0}\left.\frac{\mathrm{d}V}{\mathrm{d}T}\right|_{\mathrm{tetra}} = 4.7 \times 10^{-5}\,\mathrm{K}^{-1}\,, \tag{5.3}$$

where $V_0 = 310.1\,\text{Å}^3$ is the volume at T_c. Hereby, we neglect the temperature dependence of the thermal expansion, but the error made is not larger than 1%. As an alternative approach, we can describe the anisotropy of the thermal expansion by a second-rank tensor. In the tetragonal symmetry, the tensor possesses two independent coefficients $\alpha_{11}^{\mathrm{tetra}}$ and $\alpha_{33}^{\mathrm{tetra}}$. These coefficients can be directly derived from the lattice parameters shown in Figure 5.6. Again we use linear fits to the evolution of a and c above T_c, we then write

$$\alpha_{33}^{\mathrm{tetra}} = \frac{1}{c_0}\left.\frac{\mathrm{d}c}{\mathrm{d}T}\right|_{\mathrm{tetra}} = 2.08 \times 10^{-5}\,\mathrm{K}^{-1} \quad \text{and} \tag{5.4}$$

$$\alpha_{11}^{\mathrm{tetra}} = \frac{1}{a_0}\left.\frac{\mathrm{d}a}{\mathrm{d}T}\right|_{\mathrm{tetra}} = 1.36 \times 10^{-5}\,\mathrm{K}^{-1}\,, \tag{5.5}$$

where $a_0 = 5.14$ and $c_0 = 11.72$ are again the values at T_c. These values can be directly compared to the evolution of the secondary strain coefficients in the monoclinic phase, described as $\varepsilon_{11}^{\mathrm{SS}}$ and $\varepsilon_{33}^{\mathrm{SS}}$ shown in Figure 5.7. In first approximation, these values also change almost linearly with temperature and we have

$$\frac{\mathrm{d}\varepsilon_{33}^{\mathrm{SS}}}{\mathrm{d}T} = -1.45 \times 10^{-5}\,\mathrm{K}^{-1} \quad \text{and} \tag{5.6}$$

$$\frac{\mathrm{d}\varepsilon_{11}^{\mathrm{SS}}}{\mathrm{d}T} = -1.03 \times 10^{-5}\,\mathrm{K}^{-1}\,, \tag{5.7}$$

The meaning of the negative sign is that these strains act against the background thermal expansion. The fact that the ratios $(\varepsilon_{33}^{\mathrm{SS}}/\varepsilon_{11}^{\mathrm{SS}})$ and $(\alpha_{33}^{\mathrm{tetra}}/\alpha_{11}^{\mathrm{tetra}})$

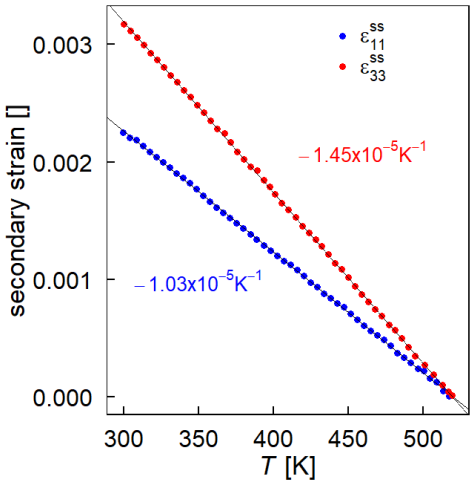

Figure 5.7: Temperature dependence of the secondary strains ε_{11}^{SS} and ε_{33}^{SS}. The solid lines are a linear fit to the data which are taken from David and Wood [30]. The slopes of the linear fits are provided in the figure.

are very similar justifies the use of a single coefficient to compare the thermal expansions in the two phases. This allows us to estimate the contribution of the thermal expansion to the shift of the optical absorption edge. ★/ In the high-symmetry tetragonal phase, only thermal expansion is present and both absorption edges follow linear and parallel evolutions at an average rate of $\approx -0.85\,\mathrm{meV\,K^{-1}}$ for a volumetric thermal expansion coefficient of $\approx 4.7 \times 10^{-5}\,\mathrm{K^{-1}}$. At the transition, the volume exhibits a kink and the thermal expansion is reduced to $1.4 \times 10^{-5}\,\mathrm{K^{-1}}$ below T_c. Assuming the same scaling, this would account for a change in absorption edge of $\approx -0.25\,\mathrm{meV\,K^{-1}}$, which is only a small fraction of the total change shown in Figure 5.4(a). We conclude that the ferroelastic shear strain dominates the evolution of the optical band gap in the monoclinic phase. This spontaneous shear strain develops in the (ab) plane, has B_g symmetry and is the primary order parameter of the transition [30]. In Figure 5.8(b) we show the temperature evolution of the total shear strain calculated from the a, b and γ lattice parameters as defined by Aizu [3] and reported in Ref. [30]. The respective influences of volume vs. shear strain to the optical absorption are best illustrated in Fig. 5.8(c), where we show the absorption edges versus the unit-cell volume. The contribution of the simple volume change in the monoclinic phase is shown by the extrapolated dashed line and is clearly marginal. In the inset of Fig. 5.8, we also show the difference in optical band gap ΔE caused by the phase transition as a function of temperature for both polarizations. In both cases, the evolution deviates from linearity and shows the beginning of a saturation behavior, which again is an indication that they scale predominantly with the shear strain [30]./★

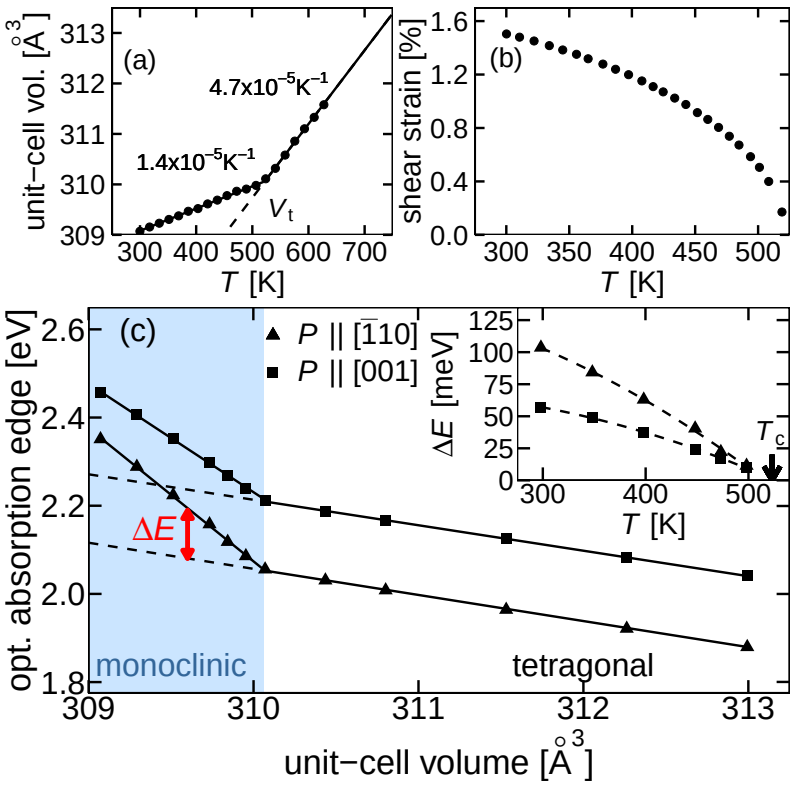

Figure 5.8: (a) Evolution of the unit-cell volume across the phase transition and (b) of the shear strain in the monoclinic phase, as discussed in the text. Data are taken from Ref. [30]. (c) Position of the absorption edge for $P \parallel [001]$ and $P \parallel [\bar{1}10]$ as a function of the unit-cell volume. Inset: Difference in absorption edges ΔE associated to the phase transition as a function of temperature. The figure has been published in [47].

5.1.4 *Discussion*

In this section, we discuss the results in the light of the current theoretical understanding [26, 34, 108, 117] of the optical absorption presented in the introduction to the thesis. ★/ We confirm the strong anisotropy of the optical absorption. At all temperatures, and irrespective of the anisotropy in the (001)-plane, the lowest absorption edge is found for light polarized perpendicular to the principal axis. For a quantitative comparison of the band gap value(s) and the anisotropy, one should bear in mind the strong temperature dependence and therefore extrapolate experimental values down to 0 K. With this in mind, we find that the absolute value of the calculated band gap [26] (2.47 eV) agrees reasonably well with our experimental value at 0 K (assuming an indirect band gap). This extrapolation is not trivial, because the behaviour at low temperatures is non linear for various reasons: the strain dependence described above, and a possible saturation of the order parameter at low temperatures [85], but also the usual non-linear lattice anharmonicity and electron-phonon interactions [103]. The first effect can be taken into account by fitting a power law $\Delta E_{\text{opt}} = A(T_c - T)^{\beta}$ to the data below T_c – this yields an extrapolated value of 2.62 eV at 0 K. Saturation of

the order parameter in $BiVO_4$ can be neglected, as demonstrated by birefringence studies [112]. On the other hand, the other non-linear effects cannot be neglected a priori. In the Appendix B, we use physical arguments to show that they could lead to an additional lowering of the extrapolated value by as much as $\approx 0.3\,\text{eV}$. In any case, the experimental value agrees well with the calculated value of 2.47 eV from Ref. [26]. On the other hand, we find a significant difference in the magnitude of the anisotropy between light polarized parallel and perpendicular to the principal axis: because of the influence of the shear strain, the difference between absorption edges is reduced to 90 meV at 0 K, which is much weaker than the theoretical value [26] of 0.5 eV. In light of the sensitivity to shear strain described above, we hypothesize that these disagreements find their origin in the accuracy with which the calculation captures the small monoclinic distortion of the scheelite structure. A better quantitative prediction will require a particular attention to these structural aspects. /★

5.2 PHOTOLUMINESCENCE IN BISMUTH VANADATE

In this section, we will first summarize the results from the characterization of $BiVO_4$ single crystals by photoluminescence. In the last part of this section, we will discuss the possible origin of the observed PL emission.

5.2.1 *Sample description and measurement details*

$BiVO_4$ single crystal substrates purchased from SurfaceNet GmbH, Rheine in Germany have been used for the photoluminescence study. Figure 5.9 shows the two substrates (a) *BVO001-Clemens* with surface orientation (001) and (b) *BVO100-Julian* with surface orientation (100). All crystal orientations are given with respect to the tetragonal unit cell.

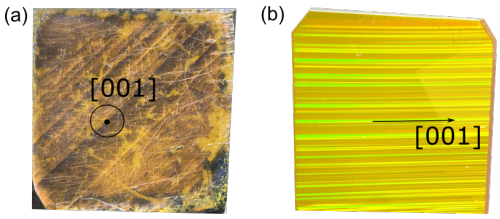

Figure 5.9: (a) Binocular image of the $BiVO_4$ single crystal substrate *BVO001-Clemens* with surface orientation (001) with gold deposition at the back surface and roughened top surface. (b) Binocular image of the $BiVO_4$ single crystal substrate *BVO100-Julian* with surface orientation (100). The domain structure with an average domain width of 80 µm is clearly visible.

Surface roughness of the crystal *BVO001-Clemens* was mechanically roughened to reduce spectral reflection.

The PL measurements were done in collaboration with S. Siebentritt and D. Adeleye. We used the PL set-up described in Section 3.2.1 with a 405 nm laser. The sample was placed in a helium cryostat with similar design described in Section 3.5.2. The room-temperature measurements have be done on the $BiVO_4$ single crystal substrate *BVO100-Julian*. The PL spectra of this sample have been recorded with the Renishaw Raman spectrometer described in Section 3.3.1. All PL spectra presented in the following section have been calibrated following the procedure described in Section 3.2.2.

5.2.2 *Results*

As discussed in Section 2.2.2, different electronic transitions can be visible in a PL measurement depending on the measurement conditions. To identify the origin of the PL emission in $BiVO_4$, we performed measurement as a function of temperature, laser power and incident light polarization. The results from these measurements will be presented in the following.

5.2.2.1 *Photoluminescence at low temperature*

First, we will have a look on the PL emission in $BiVO_4$ at low temperature. Figure 5.10 shows a PL spectrum measured at 10 K on the single crystal substrate *BVOoo1-Clemens* with surface orientation (001) plotted in (a) linear scale and (b) in log scale. In a first step, the data have been fitted with a Gaussian (black dashed line) leading to a PL maximum at 1.58 eV and a FWHM of 614 meV. The position of the PL maximum is much lower in energy compared to the expected absorption edge of 2.37 eV, see extrapolation to low temperatures in the Appendix B. Further, we observe that the PL band is relatively broad and its lineshape is asymmetric. A better fit (red dashed line) is achieved with the Reshchikov model (Equation 2.29) that accounts for an asymmetry of the PL spectrum. The Huang-Rhys factor S_e is calculated to 10.25 and $E_0^* = E_0 + 0.5\hbar\Omega$ is calculated to 2.41 eV, in which E_0 is the zero phonon line. We observed a low intensity signal at energies larger than 2.2 eV. At this point, we cannot exclude that this signal is a measurement artefact.

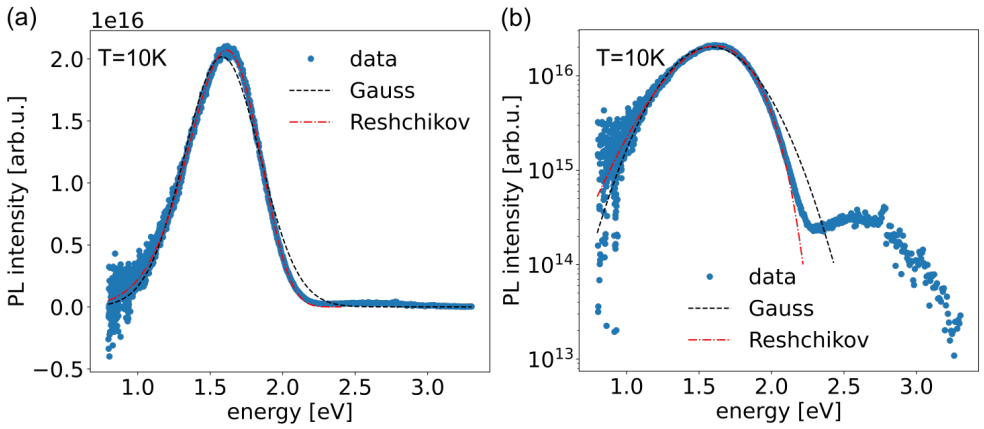

Figure 5.10: PL spectrum of *BVOoo1-Clemens* measured with 405 nm excitation at 10 K in (a) linear scale and (b) logarithmic scale. The dashed black line is a Gaussian fit with following parameters: I_{PL}^{max} =2.02 × 10^{16} counts/ sec, $\hbar\omega_{max}$ =1.58 eV and FWHM=614 meV. The dashed red line is a fit using the Reshchikov model (Equation 2.29) with the following parameters: I_{PL}^{max} =2.07 × 10^{16} counts/ sec, S_e =10.25, E_0^* =2.41 eV and $\hbar\omega_{max}$ =1.61 eV.

5.2.2.2 *Temperature-dependent photoluminescence*

In the next step, we studied the temperature dependence of the PL emission in $BiVO_4$. Figure 5.12 (a) shows PL spectra measured as a function of temperature measured on the Renishaw spectrometer with 442 nm laser excitation (2.81 eV). The dashed black lines are Gaussian fits to the data. At low temperatures, the shape of the PL band strongly deviated from a Gaussian like lineshape. At temperatures above 200 K, the Gaussian function provides a good fit to the data. The PL intensity decreases with increasing temperature. Figures 5.12(b) and (c) show the energy of the PL maximum and the FWHM

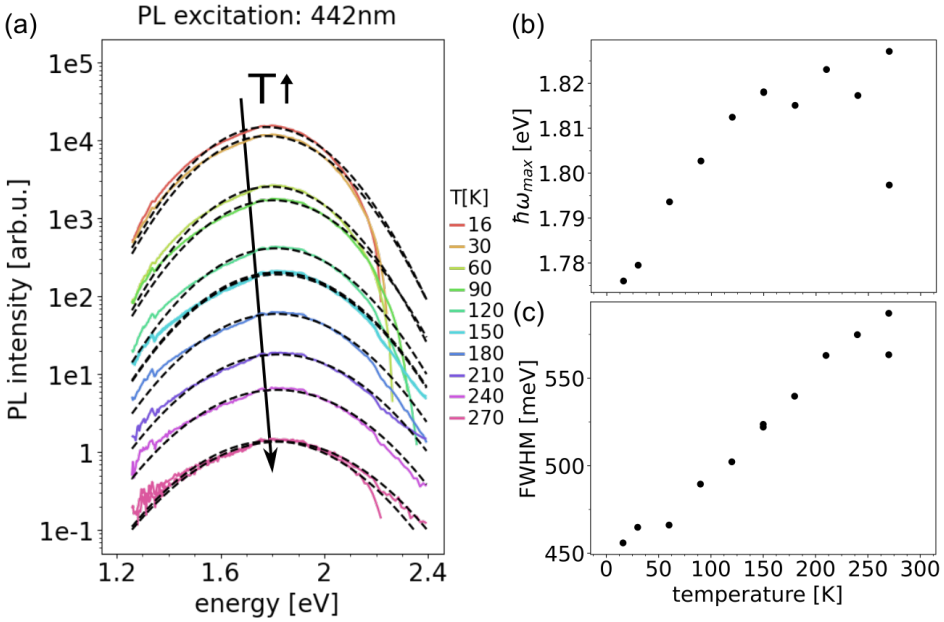

Figure 5.11: (a) PL spectra of $BiVO_4$ single crystal measured on the Renishaw spectrometer with 442 nm excitation as a function of temperature. The dashed lines are Gaussian fits to the data. (b) Position of the PL maximum obtained from the Gaussian fit shifts to higher energies with increasing temperature. (c) FWHM from the Gaussian fit increases with increasing temperatures.

extracted by the Gaussian fits as a function of temperature, respectively. Both parameters increase with increasing temperatures. The thermally activated broadening of the PL band is generally expected and goes together with the decrease in the PL intensity with increasing temperature.

Figure 5.12(d) compares the PL spectrum measured at 10 K with the PL spectrum measured at 100 K. Both PL spectra have been measured with the PL set-up and a laser excitation of 405 nm (3.06 eV). Also here, the PL intensity decreases with increasing temperature. The dashed black lines are Gaussian fits to the data and the red dashed lines are fits based on the Reshchikov model. For both temperatures, the Reshchikov model provides a better fit to the data. The fitting parameters for 100 K are given in the caption of the corresponding figure. In case of the Gaussian fit, the PL maximum and FWHM were found to be 1.62 eV and 687 meV, respectively. Both values are higher compared to the values extracted at 10 K. For the Reshchikov model, the coupling parameter S_e was found to be 9.56 which is lower than the value extracted at 100 K. E_0^* was found to be 2.48 eV at 100 K which is 70 meV higher than the value extracted at 10 K.

5.2.2.3 *Photoluminescence and its dependence on the laser power*

As discussed in Section 2.2.2, the PL intensity as a function of the excitation intensity follows a simple power law in which the exponent k characterizes the origin of the PL emission. We performed PL measurements at varying

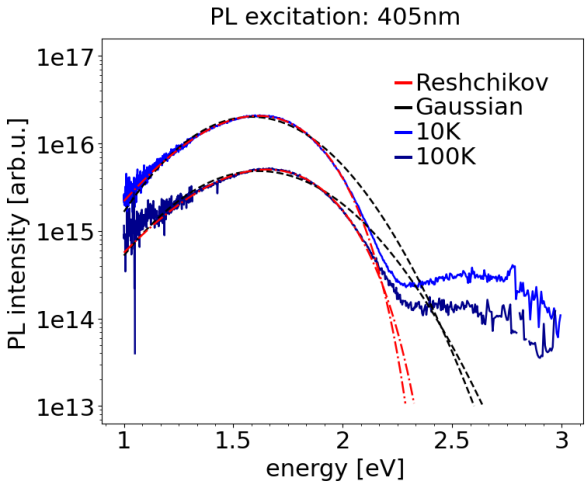

Figure 5.12: PL spectra of *BVO001-Clemens* measured on the PL set-up with 405 nm excitation at 10 K and 100 K with constant laser power of 4 mW. The red dashed lines are fits from the Reshchikov model using Equation 2.29. For 100 K, the parameters are calculated to I_{PL}^{max} =5.04 × 10^{15} counts/ sec, S_e =9.56, E_0^* =2.48 eV and $\hbar\omega_{max}$ =1.65 eV. The black dashed lines are Gaussian fits to the data with the following parameters at 100 K: $\hbar\omega_{max}$ =1.62 eV and FWHM=687 meV. For 10 K, fitting parameters have been presented in Figure 5.10.

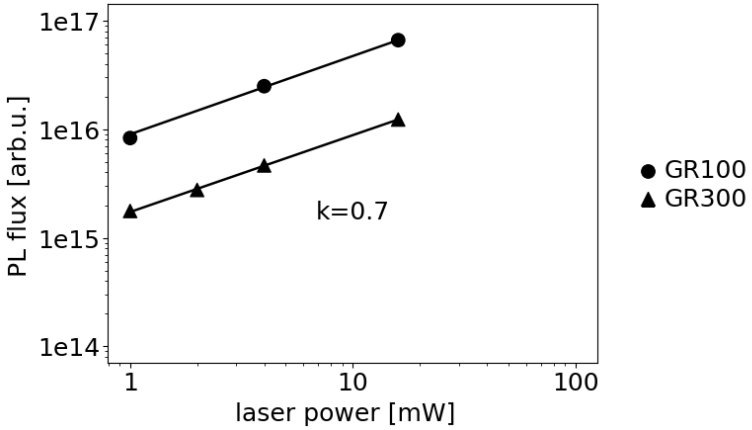

Figure 5.13: PL flux follows a simple power law dependency. The single spectra have been measured at 10 K with 405 nm excitation with a 300 l/mm (GR300) grating and a 100 l/mm (GR100) grating.

laser power at 10 K with the goal to identify the origin of the PL emission in $BiVO_4$. Figure 5.13 shows the PL intensity as a function of laser power measured with laser excitation of 405 nm (3.06 eV) and two different gratings on the PL set-up. The single spectra have been fitted with Gaussian functions. The PL intensity is then given by the integrated intensity under the Gaussian. Then, the PL intensity is plotted versus the laser power and the data were fitted with the power law given in Equation 2.26 in Section 2.2.2. For both gratings, the fits reveals a k value of 0.7.

5.2.2.4 *Photoluminescence and its polarization dependence*

In the first section of this chapter, we discussed the strong anisotropy in the optical absorption. The goal of the following experiment was to study the impact of the optical anisotropy on the PL emission. Figure 5.14 shows the PL spectra measured at 300 K on the single crystal substrate *BVO100-Julian* for two different incident light polarizations with a laser excitation of (a) 442 nm (2.81 eV) and (b) 532 nm (2.33 eV). For a laser excitation with 442 nm that is clearly above band gap, the PL band is visible for both light polarizations. For a laser excitation with 532 nm, however, the PL band is only excited if the incident light is polarized perpendicular to [001].

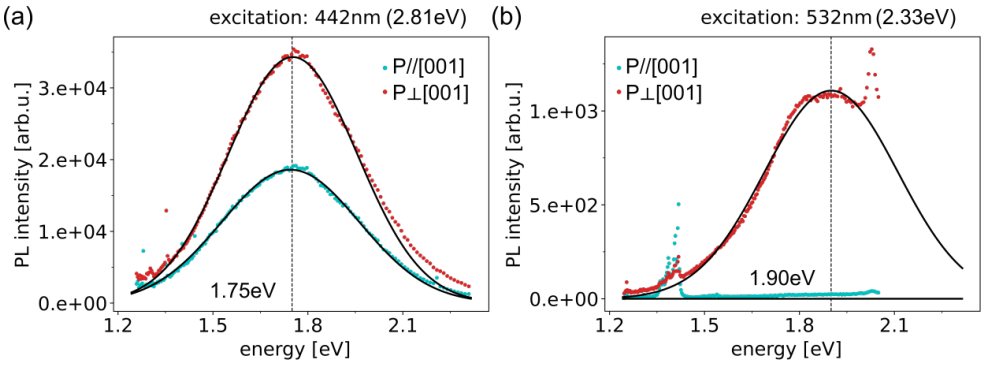

Figure 5.14: (a) PL spectra of $BiVO_4$ substrate *BVO100-Julian* measured at 300 K and incident light polarization parallel to the principal axis ($P \parallel [001]$) and perpendicular to [001] ($P \perp [001]$) with a) 442 nm excitation and (b) 532 nm excitation measured on the Renishaw spectrometer.

5.2.3 *Discussion*

We measured a PL emission with maximum intensity at 1.6 eV at 10 K. This result is in good agreement with the results from Cooper et al. [25], who reported a PL emission at 1.85 eV at 12 K on polycrystalline films.

We found that the PL band is relatively broad and its lineshape is asymmetric. Both features are typically observed in case of a PL emission originating from deep defect states. For all temperatures, the position of the PL maximum is much lower in energy compared to the optical absorption edge. In addition, the position of the PL maximum shifts $\hbar\omega_{max}$ to higher ener-

gies with increasing temperatures in contrast to the temperature trend of the absorption edge.

Also, the PL intensity decreases with increasing temperature which supports the hypothesis that the PL is defect related. The probability for carriers to escape from the defect levels and to populate higher energy states increases with increasing temperatures [68]. This process is called ionization of defects and ionized defects are inactive. In contrast, at low temperatures, carriers in the defect levels are effectively frozen and therefore defects states are more clearly visible in PL measurements at low temperatures.

Further, we measured the PL intensity as a function of laser power which follows a power law dependence with an exponent $k = 0.7$. An exponent $k < 1$ indicates that the PL emission in $BiVO_4$ is defect related.

Finally, we studied the dependence of the light polarization on the PL emission for the laser excitation at 442 nm (2.81 eV) and at 532 nm (2.33 eV). For both laser excitation energies, we studied the impact on the PL emission for light polarization parallel and perpendicular to the principal axis [001]. For laser excitation at 442 nm (2.81 eV) which is clearly higher than the band gap energy in $BiVO_4$, the PL emission is excited for both light polarization conditions. For the laser excitation at 532 nm (2.33 eV), the PL emission is only excited for light polarized perpendicular to [001]. For light polarized perpendicular to [001], the optical absorption edge was found to be 120 meV lower than light polarization along [001]. The energy of the green laser (532 nm) is sufficiently high to create a electron-hole pair and to excite a PL emission. For the light polarization along [001], however, the energy of the green laser is not high enough in energy to excite a PL emission. This is another indication that the PL emission is related to a defect state. If the PL emission would originate from a band-to-band transition, both lasers should be sufficiently high to excite the PL signal.

In summary, temperature-dependent, laser power-dependent and polarization-dependent PL measurements suggest that the PL emission in $BiVO_4$ is defect related. The broad and asymmetric lineshape of the PL band suggest PL emission from deep defects levels. A model that accounts for PL emission from deep defects is the Reshchikov model. We found that the Reshchikov model provides a much better fits than the Gaussian function to the data measured at 10 K and 100 K. The Reshchikov model assumes electron-phonon coupling and depending on its strength, the actual energy of the electronic transition involved in the PL emission cannot be simply derived from the PL maximum. The actual energy of the electronic transition is then given by the zero-phonon line. In our case, the exact value for the zero-phonon line cannot be calculated since the effective phonon energy $\hbar\Omega$ is unknown. The effective phonon energy as well as the Huang-Rhys factor can be experimentally determined by measuring the temperature-dependent broadening of the PL band. The procedure is described in [4] and [78]. However, the energy of the zero-phonon line must be very close to the band gap energy indicating that the PL originates either from a state very close in energy to the band gap energy or from the actual band-to-band transition. In both

cases the phonon coupling is relatively strong which is unusual for a band-to-band transition.

The Huang-Rhys factor is an indication for the phonon-electron coupling strength. We extracted a Huang-Rhys factor S_e of 10.25 and 9.26 for 10 K and 100 K, respectively. The extracted values are comparable to the Huang-Rhys factor of $S_e = 7.4$ observed in GaN by Reshchikov [79]. In case of $S_e > 1$, the PL maxima shift away from the zero-phonon line. That is why we cannot conclude on the actual transition energy of the defect level from the current measurements. At this stage, we would require further measurements at various temperatures to justify the applicability of the Reshchikov model and to verify its fitting parameters, especially the effective phonon energy and the Huang-Rhys factor.

5.3 CONCLUSIONS

We measured the optical absorption in $BiVO_4$ over a broad temperature range across the ferroelastic transition. We extracted a band gap of 2.27 eV at room temperature. The value agrees well with the band gap values that have already been published. Our data do not provide a direct support for the indirect nature of the band gap, but they do show that the nature of the band gap remains unchanged in the temperature range under study. We quantified the optical anisotropy by measuring the absorption edges for light polarized parallel and perpendicular to the principal axis. We found that the high-symmetry tetragonal phase exhibits a constant anisotropy in optical absorption of 0.2 eV. In the low-symmetry monoclinic phase, the optical anisotropy continuously reduces to 0.1 eV at room temperature. The fundamental band gap was found for light perpendicular to the principal axis which is consistent with the expectations from DFT calculations. We believe that because of the strong optical anisotropy the activation of different band-to-band transitions is possible by playing with the polarization of the light. We demonstrate that the spontaneous shear strain which develops in the monoclinic phase, dominates the temperature evolution of the absorption edges and enhances the thermochromic behaviour. These findings indicate that a careful control of crystallite orientation would be beneficial for the optimization of the optical properties of $BiVO_4$-based light absorbers. Additionally, interface effects, epitaxy, nano-size effects, or cation substitution could be used to take advantage of the sensitivity to strain.

Temperature-dependent, laser power-dependent and polarization-dependent photoluminescence studies show that the broad PL band observed in $BiVO_4$ might be defect related. The data at 10 K and 100 K are well described by the Reshchikov model that suggests deep defect levels as the origin for the PL emission. Because the Reshchikov model suggests a strong phonon-electron coupling ($S_e > 1$), we cannot conclude on the actual transition energy of the defect level from the current measurement. At this stage, further measurements at various temperatures are required to justify the use of the Reshchikov model and to verify its fitting parameters. No evidence for a band-to-band PL emission was found.

5.4 PERSPECTIVES

UV/Vis spectroscopy is limited to the characterization of the optical absorption in the vicinity of the absorption edge. The characterization of the sub-band absorption and the absorption at energies above the absorption edge remains open. A technique that is very well suited for the characterization of the high absorption coefficient values is ellipsometry. Ellipsometry analyses the change of polarization of reflected light by the sample surface and therefore allows for the characterization of the complex refractive index including the absorption coefficient. Ellipsometry is a complementary technique to UV/Vis spectroscopy that allows for the characterization of the optical

anisotropy as well as the birefringence. However, the application of ellipsometry on anisotropic materials requires detailed know-how.

As discussed in the previous chapter, the extrapolation of the optical absorption edge to low temperatures is expected to be non-linear. Characterization of the optical anisotropy at low temperatures would allow for quantitative comparison with DFT calculations that often provide values at 0 K.

The broad PL emission observed in $BiVO_4$ is strongest at low temperatures. Also, here characterization of the optical properties by UV/Vis spectroscopy and ellipsometry at low temperatures could help to make a direct comparison. Cooper et al. [25] suggested that the broad PL band is caused by deep defects originating from oxygen vacancies. They support their hypothesis by DFT calculations. However, so far the nature of the defects has not been experimentally verified. The Reshchikov model, which describes the emission from deep defect levels, provides a good fit to the asymmetric lineshape of the broad PL emission at low temperatures. However, further measurements at various temperatures are required to verify the fitting parameters, especially the zero phonon line and the Huang-Rhys factor, a measure for the coupling strength. A direct measurement of the zero phonon line could be done by a photoluminescence excitation experiment in which the PL intensity is measured as a function of excitation energy.[4] The technique gives the absorption profile of a defect and therefore the actual defect level.

CONTRIBUTIONS

I would like to thank M. Weber an J. Lehmann for their help on the temperature-dependent transmittance and reflectance measurements. Thank you T. Leinen who performed a pre-study on the microspectrophotometer to check the feasibility of this study.

Thank you to D. Adeleye for her help on the photoluminescence measurements and for her guidance on the analysis of the data. Many thanks to S. Siebentritt for the discussions and her feedback on the interpretation of the photoluminescence data.

6

RESONANT RAMAN SCATTERING IN BISMUTH VANADATE

A resonant Raman experiment demands for a tunable laser and a spectrometer that can be easily tuned to the changing laser energies. Starting with a laser excitation at energies far below the optical absorption, the laser energy is stepwise increased while measuring the Raman spectrum at each energy step. At the moment at which the laser energy matches the energy of an electronic transition, the Raman cross section is enhanced according to Equation 2.55 and we arrive at resonance condition. By further increasing the laser energy we move out of resonance condition and the Raman cross section decreases again.

In contrast to a typically Raman experiment in which small changes in the Raman shift are of interest, the challenge lies here in measuring the Raman intensity precisely. This kind of experiment was new to our research group and we repeated the experiment in three studies on two different samples and with slightly modified experimental set-ups. In this chapter, the results of the three studies and their limitations will be discussed in chronological order. Finally, the consistency of the main findings from the three studies will be validated.

6.1 FIRST RESONANT RAMAN STUDY USING A CONFOCAL MICROSCOPE

In this section, we describe the results from our first resonant Raman study using a tunable laser. For this study, the incident light was focused with a confocal microscope onto the sample.

6.1.1 *Sample description and measurement details*

We used the single crystal sample *BVO001-Andreas* that was cut from a larger crystal pulled by Czochralski-method. The surface orientation of this sample is (001) with respect to the principal axis; in plane we find the *a* and *b*-axis.

For the resonant Raman study we used the triple-stage spectrometer T64000 from Horiba that is described in Section 3.3.2. For the excitation, we used in total 8 emission lines from an ArKr laser (476 nm, 488 nm, 501 nm, 514 nm, 520 nm, 531 nm, 568 nm and 647 nm) and a continuous tunable dye laser in the energy range from 580 nm to 643 nm. We used the Horiba spectrometer in the micro mode in which the incident light is focused by a confocal microscope onto the sample surface.

In order to study the phonons of different symmetries, we performed experiments in parallel and cross polarization configuration. To label the different polarization configurations, we use Porto's notation. On the sample

BVOoo1-Andreas, we have $c(aa)\bar{c}$ and $c(ab)\bar{c}$ for parallel and cross polarization, respectively. A polarizer was placed after the sample and before the analyser. To change the polarization condition from parallel to cross polarization, a $\lambda/2$-plate was placed before the beam splitter. For the wavenumber calibration we used silicon with a surface orientation (111) (*Si111*) and for the intensity calibration we used the transparent scatterer CaF_2 with a single Raman mode at 322 cm^{-1}. For CaF_2 and *Si111*, there are no Raman selection rules. However, the spectral response of the equipment might be different for parallel and cross polarization. That is why we performed calibration measurement on CaF_2 and on *Si111* for the both polarization conditions.

Starting with the laser excitation at a certain wavelength, first the $BiVO_4$ sample was measured for cross and parallel polarization at constant laser power of around 1 mW. Then the sample table was moved to the CaF_2 position and CaF_2 was measured for both polarization conditions. After that *Si111* was measured for both polarizations as well. It is important that the laser power is constant throughout the measurement of $BiVO_4$ and CaF_2. The acquisition time was increased by 2-3times for CaF_2 since the Raman intensity is much lower compared to the Raman intensity of $BiVO_4$. All measurements were done at room temperature. The measurements were done by M. Guennou in the laboratory of S. Reich at the Freie Universität Berlin, Germany.

6.1.2 *Results*

In this section, I show how the resonance Raman data are analyzed. The work flow to derive the resonant Raman profiles from the raw data is depicted in Figure 6.1. In a first step, the Raman spectrum is calibrated with silicon for the correct frequency position (Section 3.3.4.1). The calibrated Raman spectra measured on the sample *BVOoo1-Andreas* at different laser excitation energies for the parallel and cross polarization condition are shown in Figure 6.2(a) and (b), respectively. The Raman modes of A_g symmetry are selected for the parallel polarization condition $c(aa)\bar{c}$. The Raman modes of B_g symmetry are observed in the cross polarization condition $c(ab)\bar{c}$ together with A_g modes leaking into the spectra. All spectra are normalized to the A_g^8 mode at 828 cm^{-1} for better comparison.

After the frequency calibration, the spectrum was separated into three frequency ranges. Each frequency range was then fitted with several Lorentzian functions depending on the number of Raman peaks visible in the spectrum, the fitting details are shown in the Appendix C.

In a next step, the Raman cross section Rcs_k^{BVO} for each individual Raman mode k is extracted from the Lorentzian functions. The Raman cross section of an individual mode is given by the integrated intensity of the corresponding Lorentzian function.

In a last step, the Raman cross section of each individual Raman mode in $BiVO_4$ is normalized to the Raman cross section of CaF_2. The Raman cross section of CaF_2 was extracted by fitting the mode at 322 cm^{-1} with a Lorentzian function, see also Appendix C.

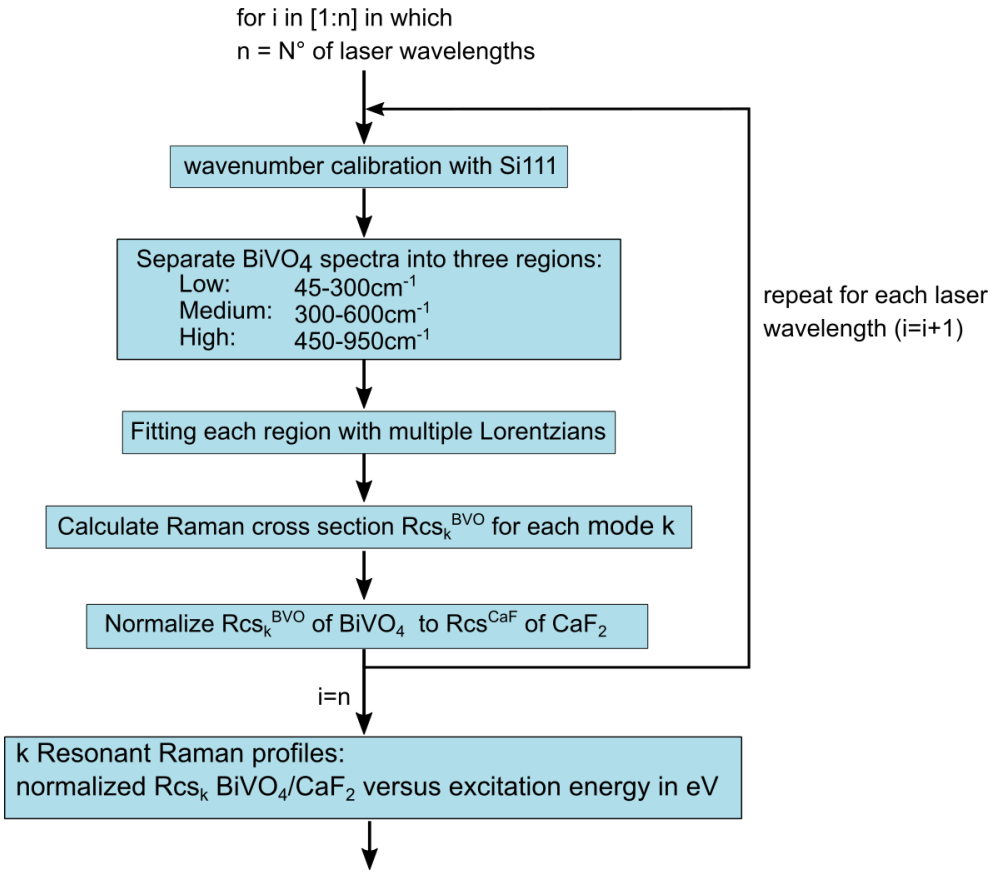

Figure 6.1: Flow chart showing the steps in the data analysis to calculate the Raman cross section.

All steps of the work flow were repeated for each laser wavelength. Finally, the normalized Rcs_k for each individual Raman mode k is plotted as a function the excitation energy in a resonant Raman profile.

6.1.2.1 *Resonant Raman effects for the A_g modes*

The resonant Raman profiles of the A_g modes are shown in Figure 6.3. They were measured with parallel light polarization $c(aa)\bar{c}$ on the sample *BVO001-Andreas*. For the normalization to CaF_2, we used the spectra measured with parallel polarization shown in the Appendix C, Figure C.3(a).

The data in each resonant Raman profile were fitted by the Equation 2.55. The transition energy E_a and the damping constant γ are provided for each resonant Raman profile. In average we found a transition energy E_a of 2.23 eV and a damping constant γ of 0.32 eV, corresponding to a lifetime τ of 2.06 fs. The data points symbolized with red triangles were not considered for the fitting. It is important to note that these red data points are coming from the same Raman spectrum measured at 580 nm, 626 nm and 643 nm in each resonant Raman profile.

The Raman cross section of the A_g^1 soft mode at 60 cm^{-1} is not shown. Because of the choice of the measurement parameters, there are no data

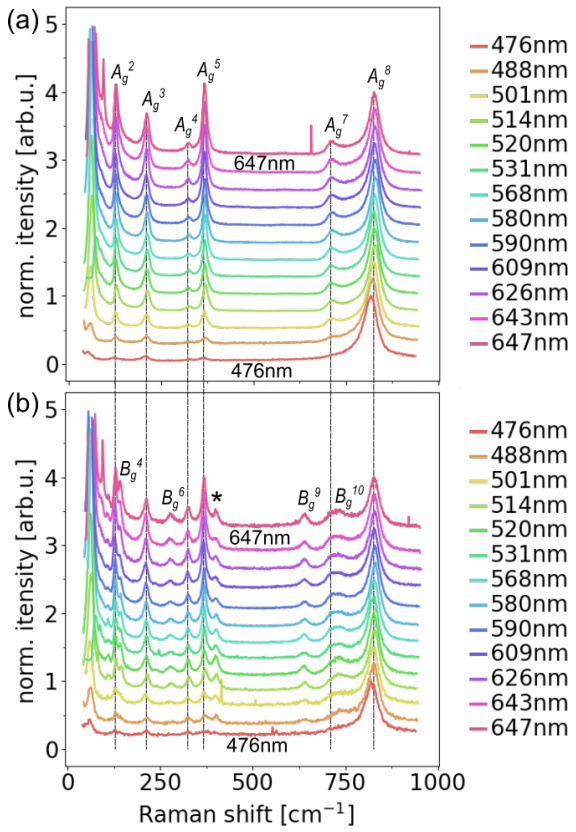

Figure 6.2: Raman spectra measured on the sample *BVO001-Andreas* at different laser excitation energies for the scattering geometries (a) $c(aa)\bar{c}$ and (b) $c(ab)\bar{c}$. All Raman spectra are calibrated with silicon for the correct frequency position and normalized to the A_g^8 mode at 828 cm^{-1}.

available for frequencies below 45 cm^{-1} meaning the low frequency tail of the soft mode is not measured. A precise fitting of the A_g^1 soft mode was not possible because of the missing data at low frequencies.

6.1.2.2 *Resonant Raman effects for the B_g modes*

We calculated the normalized *Rcs* of the Raman modes with B_g symmetry following the same procedure as described above. The details on the calculations are provided in the Appendix C.

Figures 6.4(a) to (d) show the resonant Raman profiles of the Raman modes with B_g symmetry measured on the sample *BVO001-Andreas* at cross polarization $c(ab)\bar{c}$. Figure 6.4(e) shows the resonant Raman profile of the A_g^8 mode leaking into the spectra measured with the same light polarization. Whereas the normalized *Rcs* of the B_g^{10} mode at 734 cm^{-1} and A_g^8 mode at 827 cm^{-1} maximize at around 2.13 eV, no clear response to resonance condition is observed for the Raman modes B_g^4 at 143 cm^{-1}, B_g^6 at 279 cm^{-1} and B_g^9 at 638 cm^{-1}. The resonant Raman profiles of the B_g^{10} and A_g^8 mode were fitted with the Equation 2.55. The data points indicated with red triangles were excluded for the fitting algorithm. We found a transition energy E_a of

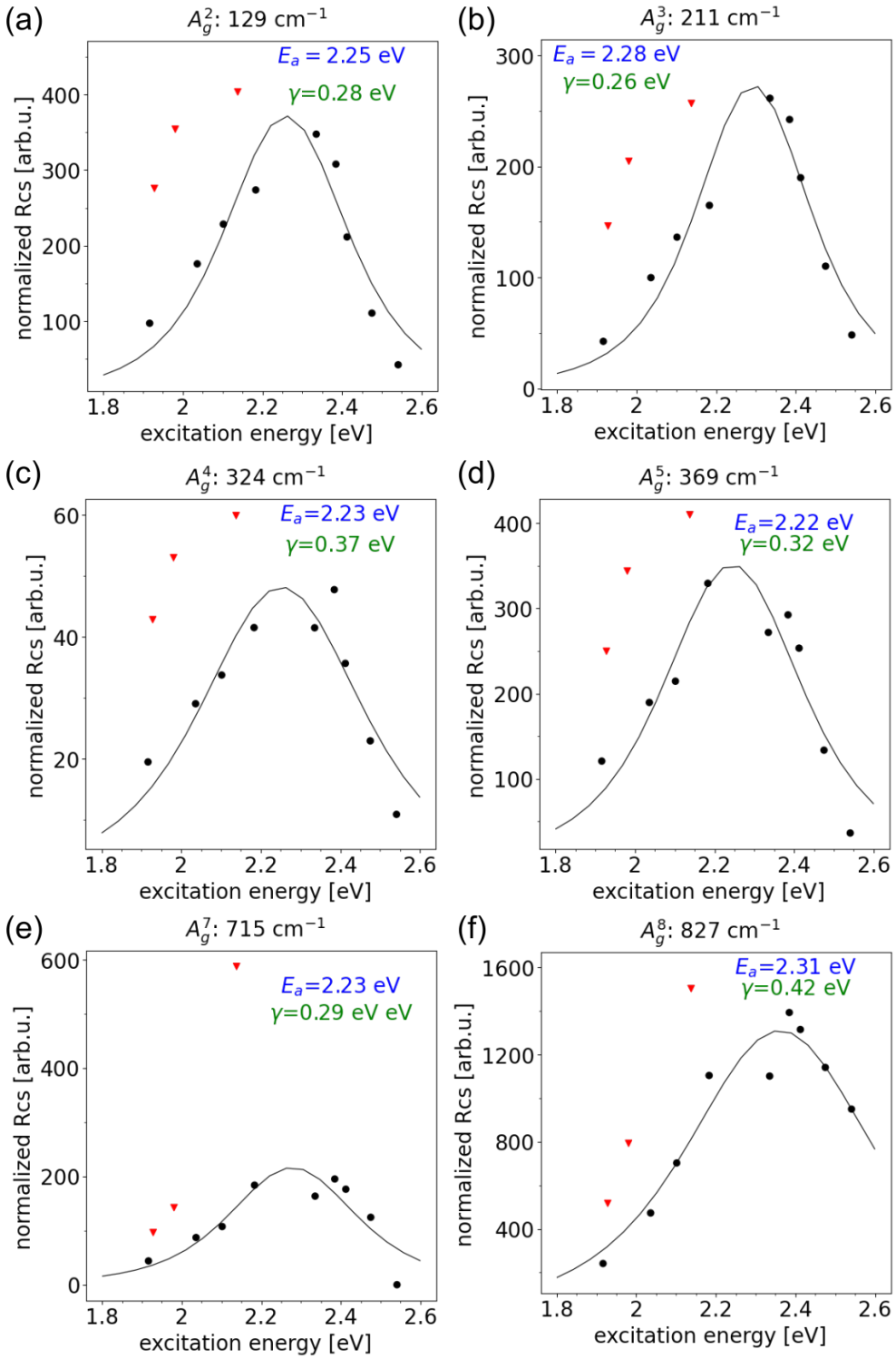

Figure 6.3: Resonant Raman profiles of modes with A_g symmetry measured on the sample *BVO001-Andreas* with parallel light polarization $c(aa)\bar{c}$ for (a),(b),c) the low, (d),(e) the medium and (f),(g) high frequency range. The solid black lines are fits to the data using the Equation 2.55. The transition energy E_a and the damping constant γ are provided in the plot. The red data points are not considered for the fits.

2.13 eV, 2.14 eV and damping constant γ of 0.54 eV, 0.48 eV corresponding to a lifetime τ of 1.22 fs, 1.37 fs for B_g^{10} and A_g^8, respectively.

6.1.3 *Discussion*

We observed resonant Raman effects for the A_g modes measured on the sample *BVO001-Andreas* at room temperature and with light polarization $c(aa)\bar{c}$. In this polarization configuration the incoming light is perpendicular to the principle axis, meaning we probe the fundamental absorption edge. The normalized Raman cross section of all 7 A_g modes show a comparable resonant Raman profiles and we extracted an average transition energy of 2.23 eV that matches the fundamental absorption edge of 2.27 eV from UV/Vis spectroscopy. The lifetime of the electrons in the corresponding electronic state was estimated to 2.03 fs.

For the extraction of the transition energy and the corresponding lifetime, we excluded some data points from the fitting in case of the resonant Raman profiles obtained for the sample *BVO001-Andreas*. These outliers were excluded on the basis of all resonant Raman profiles measured at the same light polarization because they did not seem to match the overall trend. The measurement itself or the raw data did not show any anomalies. It is noticeable that all of these outliers appear on the low-energy side. Reasons for these outliers could be in the measurements itself, for example, variations in the laser power or in the focal point of the laser on the sample surface moving from one laser energy to the other. The focusing of the laser is done visually. A rough sample surface results in the scattering of some parts of the laser light. Because of the scattering the laser spot appears blurry and a visual focusing is more difficult then on a polished sample surface. Differences in the focal point might lead to variations in Raman intensity despite the expected intensity variations from the resonant Raman effect.

Another reason for the outliers on the low-energy side might be an intrinsic one. Because these outliers were found at energies below the absorption edge, they might be related to defect states in the band gap.

For the calculation of the Raman cross section we fitted the spectra with multiple Lorentzian functions. This procedure might introduce an error especially when deviations from a Lorentzian-like lineshape are observed. We observed lineshape asymmetries for the A_g^2 and the A_g^7 mode. The lineshape asymmetry for the A_g^7 mode is caused by the phonon-phonon coupling that we discussed in Section 4.3. The phonon-phonon coupling is strongly temperature dependent. At room temperature, we consider the error to be small while fitting these modes with a Lorentzian function.

We observe no clear response of the B_g modes to the resonance condition measured on the sample *BVO001-Andreas*. Only the B_g^{10} mode seem to resonate but looking at the raw data in Figure 6.2, we cannot exclude that the A_g^7 leaks into the spectra and overlaps with the B_g^{10} mode. Therefore, we believe that the resonant Raman profile of the B_g^{10} mode is dominated by the resonance of the A_g^7 mode. In general, the analysis of the Raman effect on the

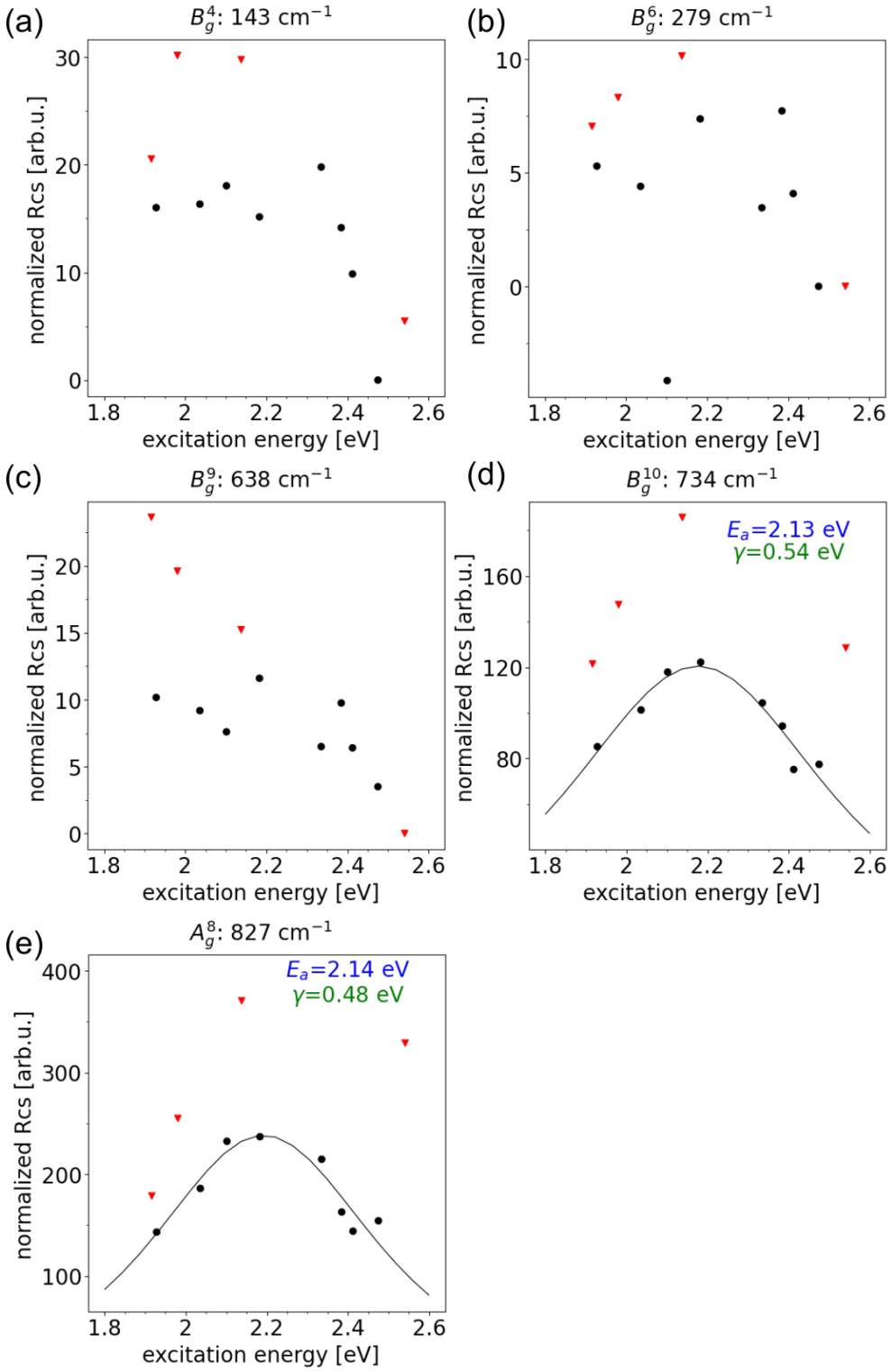

Figure 6.4: Resonant Raman profiles of B_g modes (a) to (d) measured on sample *BVO001-Andreas* with cross polarization $c(ab)\bar{c}$. (e) shows the resonant Raman profile of an A_g mode leaking into the spectra measured at the same light polarization. The solid black lines are fits to the data using the Equation 2.55. The transition energy E_a and the damping constant γ are provided in the plot. The red data points are not considered for the fits.

B_g modes is very difficult. The Raman intensity of all B_g modes is relatively low compared to the intensity of the A_g modes leaking into the spectra. For many of these modes we observe overlapping intensities. Only the B_g^6 and B_g^9 are well isolated. Nevertheless, the resonant Raman profile of the B_g^4, B_g^6 and B_g^9 suggest a constant normalized Raman cross section that decreases at energies above the fundamental absorption edge. The reason for the decrease of the normalized Raman cross section is most likely the increase in absorption above the band gap leading to a change in the scattering volume.

Overall, the data points in all of the resonant Raman profiles are limited to an energy range from 1.92 eV to 2.54 eV and to 12 or even less data points in that energy range. With the current energy range, we cover the maximum in the resonant Raman profiles but we have no information on the non-resonant background. For this, measurement at energies lower than 1.92 eV would be required. Measurements at energies higher then 2.54 eV are not necessarily beneficial as the Raman intensity gets very small for $BiVO_4$ and also for CaF_2 in the UV. In addition, the spectral resolution is not as good in the UV.

6.2 SECOND RESONANT RAMAN STUDY USING THE MACRO COMPARTMENT

After very promising results for the first Raman study, we planned a second study. The Raman intensity coming from a micro spot is relatively low. This results in long measurement times. Long measurement times introduce the risk of intensity variations due to instabilities in the laser power. In addition, we planned on more measurement points in a larger energy range. A reduction in the measurement time of a single spectrum reduces the overall experiment time significantly. To reduce the measurement times, we decided to perform the second study on a larger sample in the macro compartment of the Horiba spectrometer that allows us to use higher laser powers. Another benefit, the laser beam is focused by macro lenses on the sample so that no visual focusing procedure is required. That reduces the error of intensity variations due to differences in the focusing point. In addition, the macro mode allowed us to use liquid benzonitrile instead of CaF_2 for the intensity calibration. The Raman intensity of benzonitrile is much higher compared to CaF_2 and provides a good signal up to the UV.

In this section, we discuss the result and the limitations of the second resonant Raman study on a $BiVO_4$ single crystal substrate with polished surface.

6.2.1 *Sample description and measurement details*

THE $BiVO_4$ SUBSTRATE SAMPLE was purchased from SurfaceNet GmbH in Rheine, Germany. Figure 5.1(b) shows a photograph of the $BiVO_4$ substrate sample *BVO100-Julian* with surface orientation (100). The domain structure is clearly visible. The domain width varies between 20 µm and 100 µm.

With the purpose to optically characterize the domain structure, we performed transmission measurements on single domains by UV/Vis spectroscopy with the set-up described in Section 3.1.3. Figures 6.5(a) and (b) show a microscope picture of the domain structure taken in transmission with light polarized perpendicular and along the principal axis ([001]-axis), respectively. For the light polarization perpendicular to [001], the sample appears orange and the different domains are clearly visible because of their different orange shades. For the light polarization along [001], the sample appears yellow and the different domains are hardly distinguishable by color. The difference in the absorption depending on the light polarization is also confirmed by transmittance measurements. Figure 6.5(c) shows the transmittance as a function of incident light energy measured on the domain labeled with d2 for the two different light polarizations. The absorption edge is shifted to higher energies for the measurement with light polarized parallel to the [001]-axis. At energies below the absorption edge, the transmittance is much higher compared to the other light polarization.

Then we investigated the variations from one domain to another. Figures 6.5(e) and (f) show the transmittance and reflectance as a function of incident light energy for the different domains d1 to d5 measured with light polarized perpendicular to the [001]-axis. The transmittance values at low energies show strong variations from one domain to another whereas little variations are observed for the reflectance. Consequently, the strong variations in the transmittance value must result from variations in the absorption at low energies. The absorption edge for the different domains is shown in Figure 6.5(e). Here, we defined the absorption edge as the inflexion point of the transmittance curve. The domain d2 shows an absorption edge that is 100 meV lower then the average of 2.31 eV.

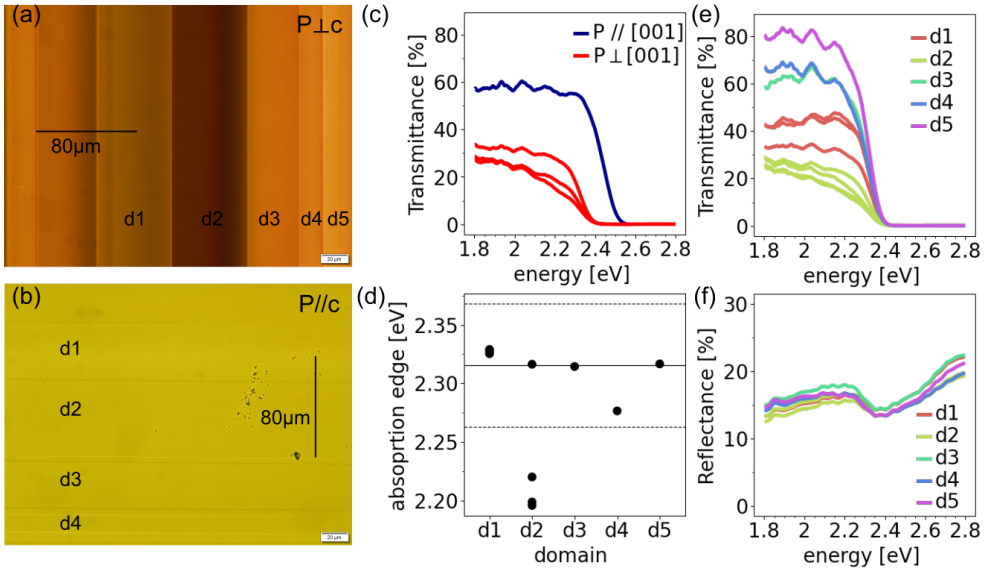

Figure 6.5: Microscope picture of the domain structure of the sample *BVO100-Julian* taken in transmission with (a) light polarized perpendicular to the principle axis [001] and with (b) light polarized parallel to [001]. The domains are labeled d1 to d5. (c) Transmittance as a function of light energy for light polarized perpendicular and parallel to [001] measured on the domain d2. (e) Transmittance and reflectance (f) as a function of light energy for the different domains d1 to d5 measured with light polarized perpendicular to [001].(d) Absorption edges extracted from the transmittance measurements for the different domains d1 to d5.

THE RAMAN SPECTROMETER T64000 from Horiba in macro mode was used for the second resonant Raman study. The laser spot size is a few hundred micrometer for the macro mode. Meaning, we measure an average of multiple domains on the sample *BVO100-Julian*. For the excitation we used the ArKr laser, the continuous tunable dye laser from 565 nm to 675 nm and the continuous tunable TiSa laser from 700 nm to 900 nm. For the frequency and the intensity calibration we used liquid benzonitrile. Liquid benzonitrile has many Raman modes in the frequency range from 400 cm^{-1} to 1700 cm^{-1}. We used the Raman mode at 460 cm^{-1} for calibration. A polarizer was placed at the entrance of the spectrometer to change the polarization of the incident

light and an additional polarizer was placed at the entrance to the analyzer to select the scattered light with a certain polarization. The sample position was fixed and not moved for the whole series of experiments. We performed resonant Raman experiments at four different polarization configurations: two at parallel polarizations $a(cc)\bar{a}$, $a(bb)\bar{a}$ and two at cross polarizations $a(cb)\bar{a}$ and $a(ba)\bar{a}$. Similar to the approach described in the previous section, first the sample *BVO100-Julian* was measured at the four different polarization configurations, then immediately afterwards liquid benzonitrile was measured with the same polarization configurations. With this approach, we assume that the laser power is constant for the measurements of the sample and for the measurements of benzonitrile. In order to redirect the incident laser from the sample or on liquid benzonitrile we used a mirror. After the completion of all measurements, the laser was tuned to the next wavelength. Then the measurements at different light polarization configurations were repeated first for the sample and then for benzonitrile. All measurements were done by myself at room temperature in the laboratory of S. Reich at the Freie Universität Berlin, Germany.

6.2.2 *Results*

6.2.2.1 *Resonance Raman effect of the A_g modes*

In a first step, we will focus on the resonant Raman effects observed for the A_g^8 mode. Figure 6.6 shows the Raman intensity of the A_g^8 mode measured on the single crystal substrate sample *BVO100-Julian* at different laser wavelengths for the light polarizations (a) $a(bb)\bar{a}$ and (b) $a(cc)\bar{a}$. All spectra are calibrated for its correct frequency position and the intensity is normalized to the Raman cross section of benzonitrile. For light polarizations $a(bb)\bar{a}$, the maximum intensity is found around 610 nm and for the light polarizations $a(cc)\bar{a}$, the maximum intensity is found around 600 nm.

In the next step, we calculated the resonant Raman profile of the A_g^8 mode following the procedure described in the previous section. Figure 6.7 shows the normalized Raman cross section of the A_g^8 mode as a function of excitation energy for the light polarizations (a) $a(bb)\bar{a}$ and (b) $a(cc)\bar{a}$. The resonant Raman peaks are indicated by a solid line as a guide to the eye which was calculated from the Equation 2.55. The data points in blue were measured at a later time. The goal of that later experiment was to verify the energy range at which no resonance occurs. In between the two experiments, the set-up was modified and therefore a constant factor between these two experiments is expected. That is why the normalized *Rcs* was multiplied by a factor of 1.8 to match the low energy points of the resonant Raman profile.

For both resonant Raman profiles, we observe a resonant peak at 2.0 eV and 2.03 eV for light polarization $a(bb)\bar{a}$ and $a(cc)\bar{a}$, respectively. In both cases, the enhancement compared to the non-resonant background is roughly a factor of 10. At low energies, the data scattering is relatively large, especially for the light polarization $a(bb)\bar{a}$. At higher energies, we observe a sec-

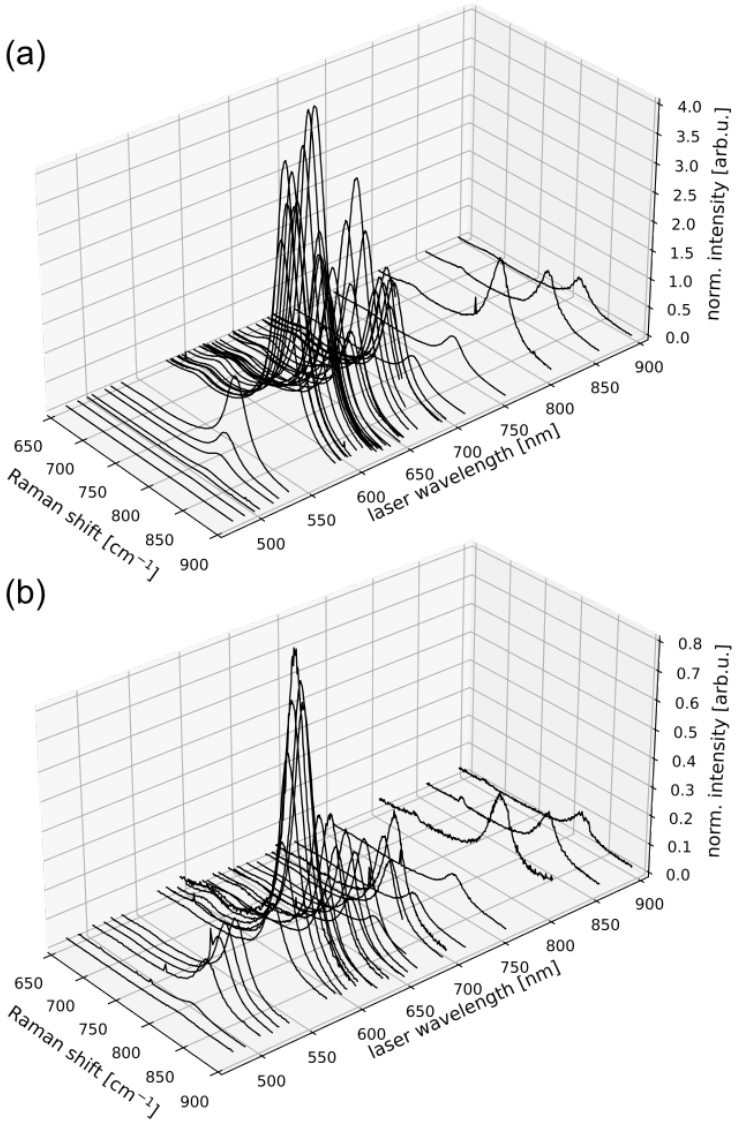

Figure 6.6: Raman intensity of the A_g^8 mode measured on sample *BVO100-Julian* at different laser wavelengths for the light polarizations (a) $a(bb)\bar{a}$ and (b) $a(cc)\bar{a}$. The Raman mode at 456 cm^{-1}in benzonitrile was used for the calibration of the frequency position and the intensity is normalized to the Raman cross section of the same mode in benzonitrile.

ond maximum at 2.34 eV for the light polarization $a(cc)\bar{a}$ that matches the energy of the optical absorption edge measured by UV/Vis spectroscopy. Because of the anisotropy in the optical absorption of 120 meV, we expect another resonant peak at 2.22 eV for the light polarization $a(bb)\bar{a}$ which is indeed visible as a shoulder to the main peak. However, the estimated transition energy of this shoulder falls in the energy range in which we have no data. At higher energies, the excitation is done with the ArKr laser that has no emission lines in the energy range from 2.15 eV to 2.35 eV.

The resonant Raman profiles of the A_g modes in the medium-frequency range are shown in Appendix C. Similar to the resonant Raman profiles of the A_g^8 mode, they show a maximum at energies ranging from 2.03 eV to 2.1 eV. The data suggest no dependence on the polarization of the incident light. For the A_g modes at medium frequencies, we have a limited number of data points because of their low intensity, especially at higher energies. The second maximum at higher energies is not observed most probably because of the limited number of data points in this energy range.

6.2.2.2 *Resonant Raman effect of the B_g modes*

Figures 6.8(a) and (b) show the resonant Raman profiles of the B_g^9 and the B_g^{10} modes measured on the *BVO100-Julian* sample with the light polarization $a(cb)\bar{a}$, respectively. Similar to the observations in the first experiment run, the Raman intensity is relatively weak for all B_g compared to the A_g modes leaking into the spectra which is especially true at higher energies. That is the reason why we have no data at energies larger than 2.2 eV for the B_g^9 mode and 2.35 eV for the B_g^{10} mode. For the B_g^9 mode, the normalized Raman cross section seems to be constant up to 2.1 eV. The normalized Raman cross section of the B_g^9 mode, however, seems to increase before the Raman cross section decreases for both modes.

6.2.3 *Discussion*

We observe resonant Raman effects for the Raman modes with A_g symmetry. In contract to the first study, we observe a strong resonant peak at energies between 2.0 eV and 2.03 eV that seems to be independent of the polarization conditions. This strong resonant Raman peak is visible in the resonant Raman profiles of all modes with A_g symmetry.

The resonant Raman profiles of the high-intensity A_g^8 modes suggest a second resonant peak that matches the energy of the optical absorption edges. At light polarization $a(cc)\bar{a}$, we found a second maximum at 2.34 eV that compares well with the optical absorption edge at 2.39 eV from UV/Vis spectroscopy. This second resonant Raman peak at higher energies seems to be sensitive to the polarization of the incident light.

In all resonant Raman profiles, we observe large data scattering at energies below 2.1 eV that is especially true for the light polarization $a(bb)\bar{a}$. In this light polarization, the incident light is polarized perpendicular to the

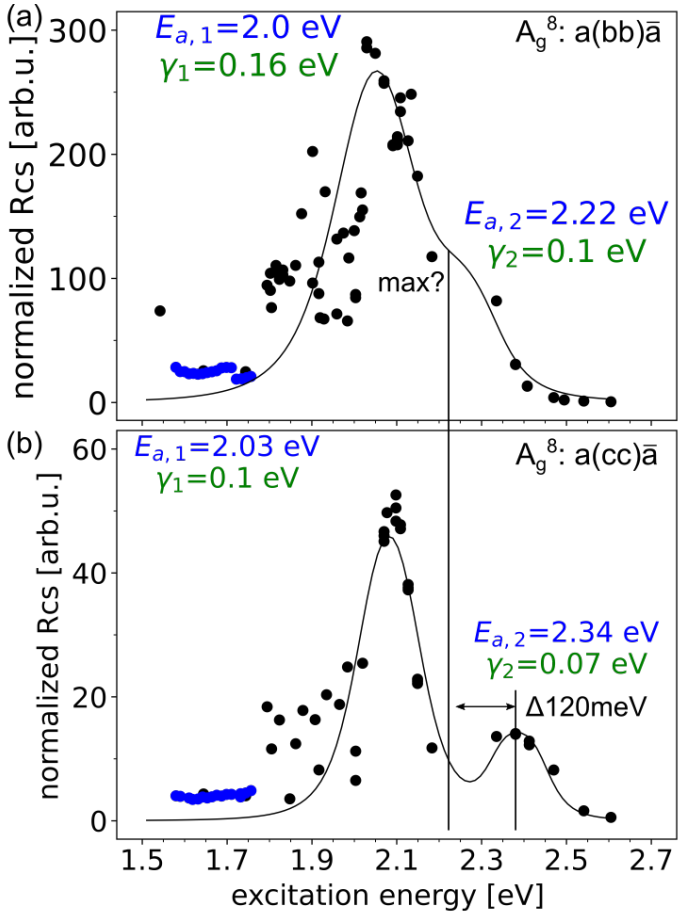

Figure 6.7: Raman intensity of the A_g^8 mode measured on sample *BVO100-Julian* at different laser wavelengths for the light polarizations (a) $a(bb)\bar{a}$ and (b) $a(cc)\bar{a}$. The Raman mode at 456 cm^{-1} in benzonitrile was used for the calibration of the frequency and the intensity is normalized to the Raman cross section of the same mode in benzonitrile. The main peaks are indicated by solid lines as guides to the eye calculated from Equation 2.55. The transition energies and the damping coefficients are provided in the plots.

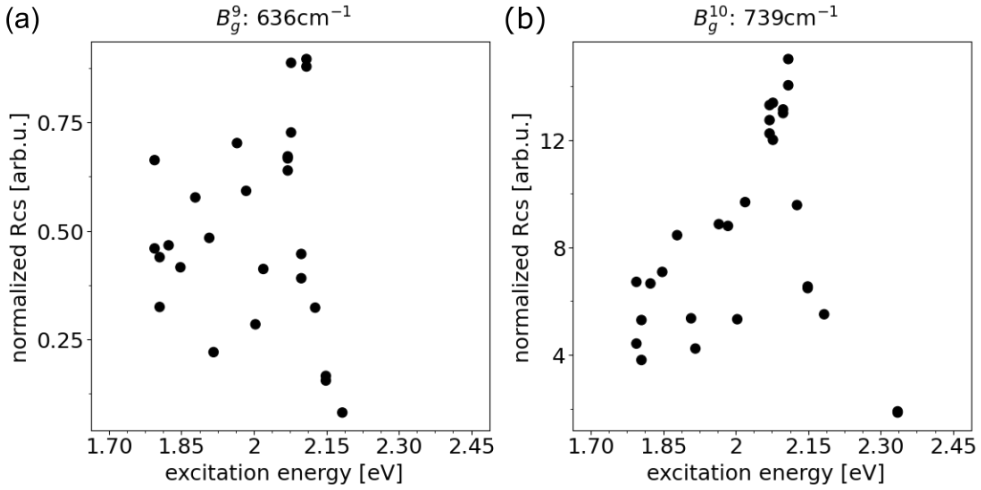

Figure 6.8: Resonant Raman profile of (a) the B_g^9 and (b) the B_g^{10} Raman modes measured on sample *BVO100-Julian* with the light polarization $a(cb)\bar{a}$. The Raman cross section is normalized to the Raman cross section of the Raman mode at 456 cm^{-1} in benzonitrile.

principal axis. We believe that the large data scattering is linked to the domain structure of the sample. From one domain to another, we measured large variations in the optical absorption below the absorption edge if the incident light is polarized perpendicular to the principal axis.

Another reason could lie in the measurement set-up itself. To redirect the laser beam from the sample to the transparent scatterer benzonitrile, we used a mirror. This mirror was smaller than the scattered beam size. If the laser beam arrives at the mirror at slightly different angles, the scattered light will not fully hit the mirror. This might have introduced an error in the intensity calibration for some laser wavelengths.

For the B_g modes, we observe no clear resonant Raman response. Similar to the observations in the first study, the analysis of the resonant Raman effects for the B_g modes is limited by the low intensity of these modes compared to the A_g modes leaking into the spectra. In many cases, the intensities of the B_g and A_g modes overlap, which makes a estimation of the Raman cross section imprecise.

6.3 THIRD RESONANT RAMAN STUDY FOCUSING ON A SINGLE DOMAIN

In the previous section, we speculated that the domain structure has an important impact on the resonant Raman profiles. $BiVO_4$ exhibits two different types of ferroelastic domains. The domain walls are always oriented along the principal axis and the crystal orientation rotates in 90° steps around the principal axis from one domain to another. The purpose of the third resonant Raman study was to investigate the resonant Raman profiles of single domains and compare the profiles coming from the two different domain types.

6.3.1 *Sample description and measurement details*

For this study, we used the single substrate sample *BVO100-Julian*. The domain structure of this sample is shown in Figure 6.9(a), in which the two different domain types are labeled with A and B. The crystallographic axes are labeled in the figure. The c-axis is parallel to the domains and clearly defined in all domains. Depending on the domain type, a^* and b^* correspond to the a-axis or the b-axis of the unit cell. For our purpose, we define that a^* is equal to the a-axis and b^* is equal to the b-axis if the measurement is taken in the domain B.

With the purpose to study single domains, we moved back to the micro mode of the Horiba spectrometer in which the confocal microscope is used to focus the laser beam on the sample. The spot size in the micro mode is roughly 1 µm. We used the Horiba spectrometer in the single monochrometer configuration to increase the output power of the scattered light on the analyzer so that the measurement time per single spectrum is significantly reduced. The Rayleigh light was removed by filters. We performed measurements at different laser wavelengths in the range of 476 nm to 660 nm. At each laser wavelength, we did one line-scan of 35 µm starting from domain type A and moving to B and a second line-scan of 35 µm from domain type B to A for the light polarization conditions $a^*(b^*b^*)\bar{a}^*$ and $a^*(cc)\bar{a}^*$. Each line-scan contains 350 single spectra that were measured in 0.1 µm steps. The dimension of a line-scan in comparison to the domain width is shown in the optical microscope image in Figure 6.9(a). The microscope image is an exemplary image that does not show the actual measurement area. Figure 6.9(b) shows single spectra measured in the domain A and in the domain B with light polarization $a^*(b^*b^*)\bar{a}^*$. Here, we limited the measurements to Raman modes with A_g symmetry in the medium- and high-frequency range. For the intensity calibration, CaF_2 was used. The measurements were done by G. Gordeev in the laboratory of S. Reich at the Freie Universität Berlin, Germany.

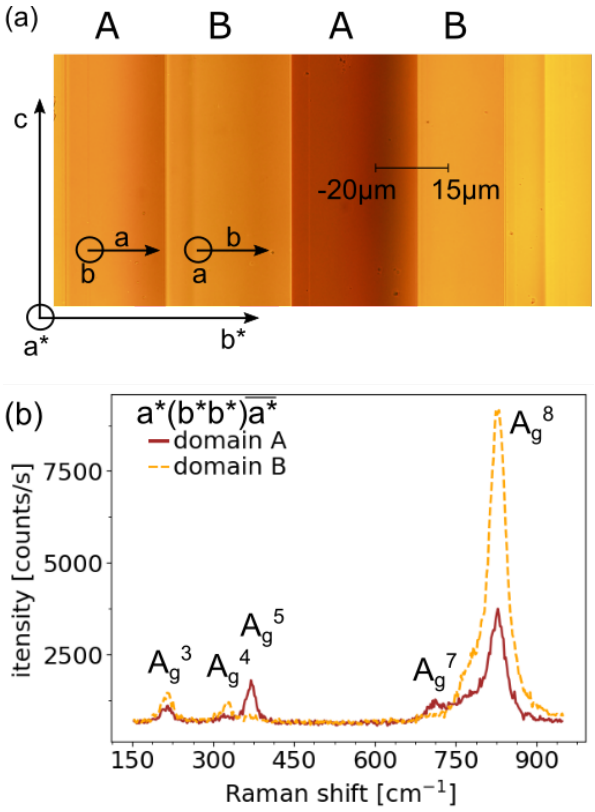

Figure 6.9: (a) Optical microscope picture showing the domain structure of the sample *BVO100-Julian*. The two different domain types are labeled with A and B. A line-scan of 35 µm across the domain A and B is indicated in the picture. (b) Single Raman spectra measured in the domain type A and B for which the Raman intensity strongly varies from one domain type to the other.

6.3.2 *Results*

The results section is structured into two main parts. First, we will discuss the variations in the Raman signal from one domain type to the other. Secondly, we will show the different resonant Raman profiles and discuss their characteristic features and their dependence on the polarization direction of the incident light.

VARIATIONS IN THE RAMAN SIGNAL from one domain type to the other have been observed previously. To investigate these variations, we fitted the high-intensity A_g^8 mode of all 350 single spectra measured along a line-scan with a Lorentzian function. From the fitting, we obtained the Raman cross section Rcs, the eigen-frequency and the linewidth as a function of position along a line-scan. Figures 6.10(a) and (b) show the Rcs measured at light polarization $a^*(cc)\bar{a}^*$ along a line-scan starting in domain type A going to domain type B and starting from B going to A, respectively. Under this measurement condition, the polarization direction of the incident and scattered light is along the c-axis and therefore parallel to the domain walls. For both line-scans, the Rcs measured in the domain type A is slightly lower (3%-7%) compared to the Rcs of the domain type B. The small step in the Raman cross sections must be the position of the domain wall.

The Figures 6.10(c) and (d) show the Rcs measured for light polarization $a^*(b^*b^*)\bar{a}^*$ for a line-scan from domain A to B and from domain B to A. For this light polarization, the polarization direction of the incident and scattered light is perpendicular to the domain walls. For both scans, the Rcs measured in the domain type A is only ≈30% of the value measured in the domain type B. Also here, the position of the domain wall falls together with the sudden increase in the Rcs. The sudden increase is much sharper when going from domain A to B.

Figures 6.11(a) and (c) show the Raman shift and linewidth (HWHM) along a line-scan measured with light polarization $a^*(cc)\bar{a}^*$. In this light polarization, the Raman shift and the HWHM is constant with an average value of $827\,\mathrm{cm}^{-1}$ and $19\,\mathrm{cm}^{-1}$ along the line-scan. For the light polarization $a^*(b^*b^*)\bar{a}^*$, however, there is a difference in the Raman shift of $2.5\,\mathrm{cm}^{-1}$ from domain A to B. The values of the linewidth scatter within an interval of two standard deviations.

In summary, the Raman cross section strongly varies from domain type A to domain type B, especially for measurements in which the polarization direction of incident and scattered light is perpendicular to the domain walls. For the further data analysis, we therefore treated the spectra measured in the domain types A and B separately.

RESONANT RAMAN PROFILES were calculated in the next step for polarization direction of the scattered and incident light (a) along the domain walls and (b) perpendicular to the domain walls. The domain walls indicate the direction of the c- (principal) axis of the unit cell.

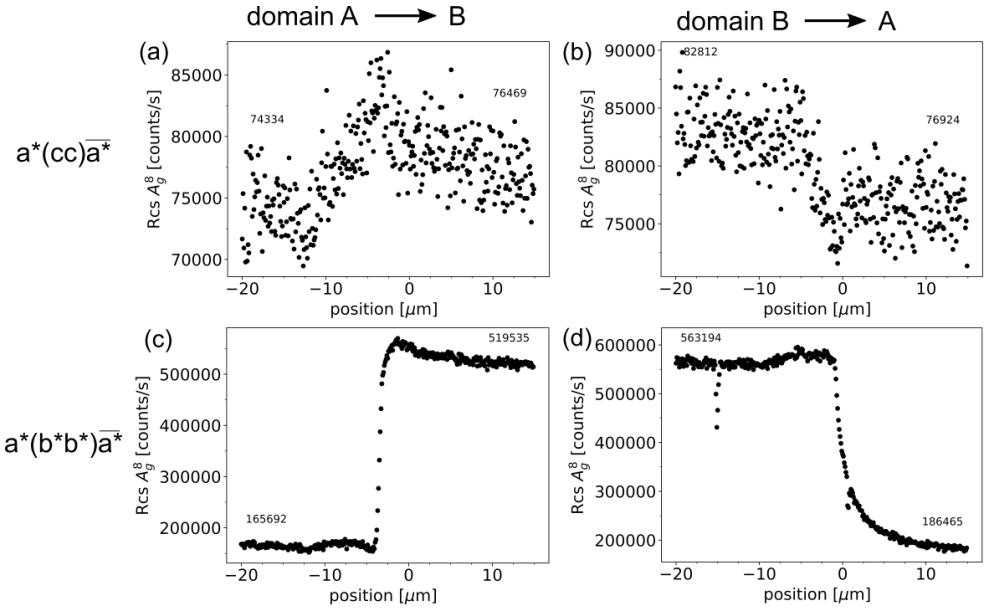

Figure 6.10: Raman cross section Rcs of the A_g^8 as a function of position along a line-scan for polarization condition $a^*(cc)\bar{a}^*$ (a) from domain A to domain B and (b) from domain B to A. Rcs along a line-scan for polarization condition $a^*(b^*b^*)\bar{a}^*$ (c) from domain A to domain B and (d) from B to A.

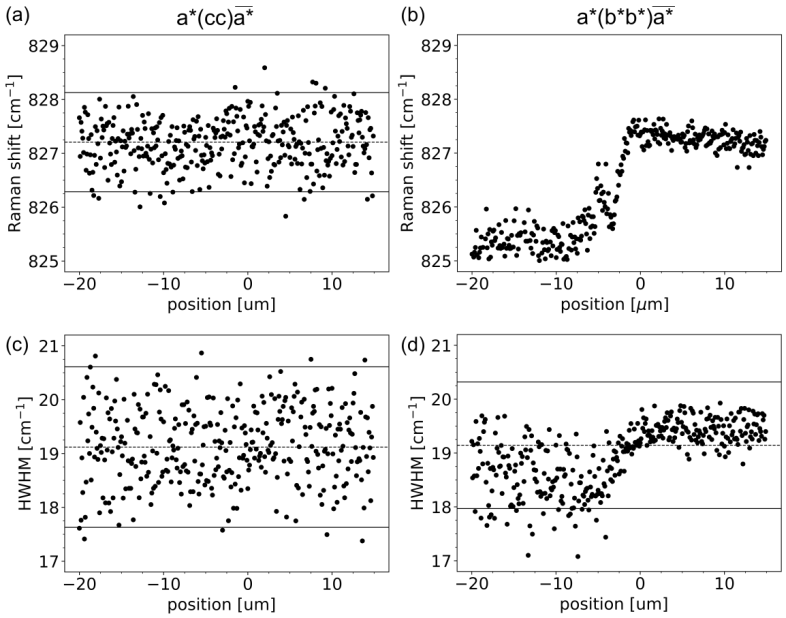

Figure 6.11: Raman shift and linewidth (HWHM) of the A_g^8 mode measured along a line-scan from domain A to B with light polarizations (a),(c) $a^*(cc)\bar{a}^*$ and (b),(d) $a^*(b^*b^*)\bar{a}^*$. The dashed lines indicate the median and the solid lines show the value of two standard deviations.

The procedure to arrive at one resonant Raman profile is described shortly. First, all 350 single spectra measured along a line-scan, were fitted by Lorentzian functions. With this we obtained the Raman cross section of the different Raman peaks A_g^4,A_g^5 and A_g^8 as a function of position along a line-scan similar to the plots shown in Figure 6.10. The domain type A and B is thereby clearly distinguishable by a sudden change in the Raman cross section. Second, the Rcs of the domain type A and B was calculated by averaging the first 50 and the last 50 data points of the line-scan. Third, the averaged Rcs was divided by the Rcs of the transparent scatterer CaF_2, which was measured at the same laser wavelength and with the same laser power. These three steps were repeated for all the line-scans from domain A to B and for all the line-scans from B to A done at different laser wavelengths and for the two different polarization conditions.

Figures 6.12(a) and (b) show the resonant Raman profiles of the high-intensity A_g^8 and the A_g^4 mode measured with polarization direction of the incident and scattered light along the principal axis, respectively. In both profiles, we observe two maxima in the normalized Raman cross section, one maximum at around 1.9 eV and another maximum at higher energies at around 2.5 eV. Here, we show only the profiles measured in the domain type A, because the Raman cross section of the domain A and B is nearly constant in this polarization condition.

For the polarization direction perpendicular to the principal axis, the Raman cross section strongly differs from domain A to the domain B. Figures 6.12(c) and (d) show the resonant Raman profiles of the A_g^8 and the A_g^5 modes measured in the domain type A. In this configuration, the propagation direction of incident and scattered light is along the b-axis of the unit cell and the polarization direction of the incident and scattered light is along the a-axis per definition. In Porto's notation, the polarization configuration is given by $b(aa)\bar{b}$. Figures 6.12(e) and (f) show the resonant Raman profiles of the A_g^8 and the A_g^4 modes measured in the domain type B leading to a polarization configuration $a(bb)\bar{a}$ in Porto's notation. In all four profiles, we see two maxima in the normalized Rcs. The first maximum is found at around 1.9 eV for all four profiles and the second maximum at higher energies around 2.3 eV.

Now, we will compare the resonant Raman profiles measured of the domain type A and B. If we compare the resonant Raman profiles shown in Figures 6.12(c) and (e) or in Figures 6.12(d) and (f), we find very similar results. The two maxima are located at nearly identical energies and the ratio of the first and second maximum is comparable. The y-axis, however, is very different which is explained by the strong variation in the Raman intensity between the domain types.

Next, we will compare the difference between the profiles of the high-intensity A_g^8 mode with the profiles of the A_g^4 and A_g^5 mode. For the profiles of the A_g^8 mode in Figures 6.12(a),(c) and (e), the second maximum at 2.5 eV / 2.4 eV or 2.34 eV is higher compared to the first maximum at 1.9 eV. For the profiles of the A_g^4 and A_g^5 mode in Figures 6.12(b),(d) and (f), we observed

the opposite. This suggests that the different modes couple differently to the electronic transitions corresponding to the two maxima in the resonant Raman profiles.

Last, we will compare the resonant Raman profiles measured with light polarization direction along and perpendicular to the principal axis. The main difference is in the energy at which the second maximum occurs. If we compare the profiles shown in Figures 6.12(a) and (c), we find the second maximum at 2.5 eV for light polarization $b(cc)\bar{b}$ while the second maximum is 100 meV lower in energy for the light polarization $a(bb)\bar{a}$ and $b(aa)\bar{b}$. Comparing the profiles from the Figures 6.12(b) and (f), we find a difference of 150 meV. This difference reflects the optical anisotropy in $BiVO_4$.

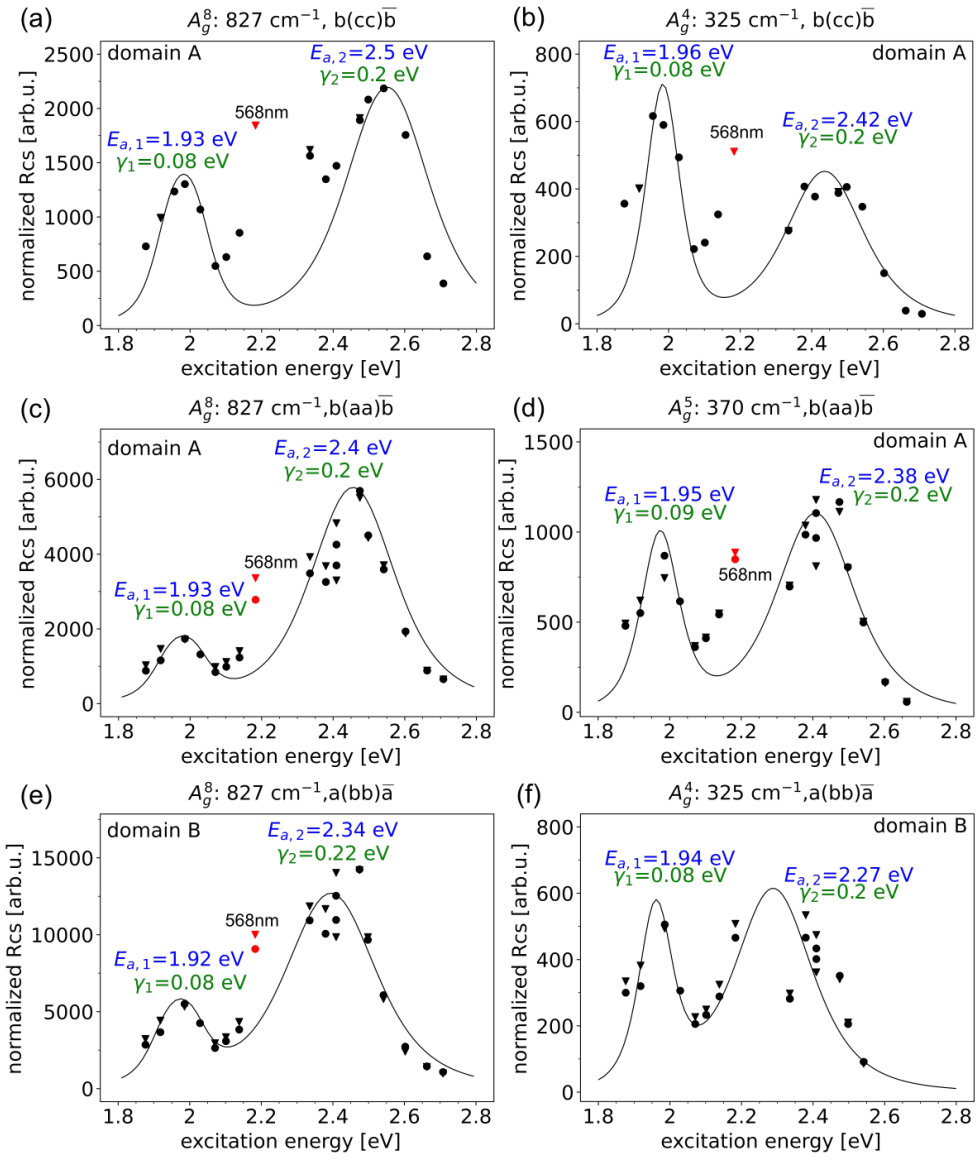

Figure 6.12: Normalized Raman cross section Rcs of the A_g^8 mode as a function of excitation energy measured for the polarization conditions (a) $b(cc)\bar{b}$, (c) $b(aa)\bar{b}$ and (e) $a(bb)\bar{a}$. Normalized Rcs of (b) the A_g^4 mode measured for $b(cc)\bar{b}$, (d) the A_g^5 mode measured for $b(aa)\bar{b}$ and (f) the A_g^4 mode measured for $a(bb)\bar{a}$. The main resonant Raman peaks are indicated by a solid line as a guide to the eyes which was calculated from Equation 2.55. The transition energies and the damping coefficients are provides in the plots.

6.3.3 *Discussion*

Depending on the light polarization direction with respect to the principal axis, we saw strong variations in the Raman intensity between the two different domain types in $BiVO_4$. We successfully eliminated the impact of the domain structure on the resonant Raman profiles by developing an experimental procedure to study the Raman cross section for the two domain types separately. For this, we performed line-scans across a domain wall that include 350 single spectra. The position of the domain wall within the line-scan is clearly visible because of a sudden change in the Raman cross section. The main limitations of this experimental procedure are the long measurement time per line-scan and the huge amount of data that requires a semi-automatic data analysis.

All resonant Raman profiles showed two maxima in the normalized Raman cross section. The first maximum was found at around 1.9 eV independent of the polarization condition in the experiment. This maximum has been observed already in the second study for the same sample which was measured in the macro compartment of the spectrometer. The fact that we observe resonant Raman scattering from an electronic level which is below the optical absorption edge is a new result and was not evident at the beginning. Because of its energy position below the absorption edge and our PL measurements, we believe that the origin of this resonant Raman peak must be defect related. To support this hypothesis, further PL measurements with the goal to confirm the transition energy of the defects states are recommended. Another possibility to confirm this hypothesis would be with the help of DFT calculations. An ideal crystal without any defects states should not show any resonance effects at energies below the band gap in the calculation.

The energy of the second maximum matches the energy of the optical absorption edge measured by UV/Vis spectroscopy. For polarization direction of the incident and scattered light along the principal axis, we found 2.5 eV and 2.42 eV for the high-intensity A_g^8 mode and the A_g^4 mode, respectively. For the polarization direction perpendicular to the principal axis, the second maximum is at lower energies. We found a difference of 100 meV for the A_g^8 and 150 meV for the A_g^4 mode. From this we conclude that the optical anisotropy is reflected in the energy position of the second maximum that strongly depends on the polarization direction of the incident and scattered light. These findings suggests that the origin of the second resonant Raman peak must be a band-to-band transition.

Further, we observed that the ratio of the second and first resonant Raman peak is different for the A_g^8 mode and the A_g^4 and the A_g^5 modes. This observation suggests that the different phonons couple with varying strength to the electronic transitions in the resonant Raman profiles.

6.4 CONCLUSIONS

In this section, we will first summarize our experience of the measurement protocols from the three different resonant Raman studies. It could be used as a guidance to perform further resonant Raman studies on $BiVO_4$ or on related semiconductor oxides. Finally, we will compare the main findings and discuss the underlying physics.

6.4.1 *Comparison of the different measurement protocols*

For the comparison, we combined representative resonant Raman profiles measured in the three different resonant Raman studies in one figure. Here, we show the resonant Raman profiles of the high-intensity A_g^8 mode only. We believe that the estimation of the Raman cross section for the A_g^8 mode is most robust against errors introduced by the fitting with a Lorentzian function because of the strong Raman intensity of this mode. For all three profiles, the polarization direction of the incident and the scattered light was perpendicular to the principal axis. The resonant Raman peaks are indicated by solid lines as a guide to the eyes which were calculated from the Equation 2.55. The data points indicated in red have not been considered here.

Figure 6.13(a) shows the resonant Raman profile obtained from study 1. The resonant Raman profile shows a strong resonant Raman peak at 2.31 eV that matches the energy of the optical absorption edge. In this study, we observed very high data scattering that might have been caused by a rough sample surface leading to differences in the focal point from one laser wavelength to another. The main learning from this study is that a resonant Raman study using a confocal microscope requires a polished sample surface.

To reduce the sensitivity to the focal point, we performed further measurements (study 2) in the macro compartment of the Horiba spectrometer on a $BiVO_4$ single crystal substrate that was purchased for this purpose. The resonant Raman profile from study 2 is shown in Figure 6.13(b). Here, we observed one strong resonant Raman peak at 2.0 eV which is clearly below the absorption edge. We believe it originates from resonances with a mid-gap defect level. The shoulder in the resonant Raman profile indicates a second resonant Raman peak that might be the resonant Raman peak observed in study 1. In the macro mode, we measure an average Raman intensity coming from several domains. Although the sample was not moved during the whole study, the domain structure seems to introduce intensity variations that do not average out and therefore the intensity variations result in large data scattering in the resonant Raman profiles.

Figure 6.13(c) shows the resonant Raman profile measured in study 3. This study confirms the presence of both resonant Raman peaks observed in the previous studies. Here, both resonant Raman peaks are clearly visible. Further, we showed that the Raman intensity varies strongly from one domain to the other, especially if the light polarization of incident and scattered light is perpendicular to the principal axis. By measuring the Raman cross section

of single domains, we could reduce significantly the data scattering in the resonant Raman profiles.

An important aspect of the measurement protocol is the intensity calibration by a transparent scatterer. The laser power for the measurement of the sample and the scatterer must be constant. Therefore, it is advised to measure the scattered immediately after the sample. The optical components in the set-up should be identical for the measurement of the sample and the scatterer. In study 1 and study 3, we used a CaF_2 single crystal for the intensity calibrations while we use liquid benzonitrile in study 2. Liquid benzonitrile clearly has two advantages over CaF_2. First, benzonitrile has several Raman peaks in the frequency range from 400 cm^{-1} to 1700 cm^{-1} and second, its Raman signal is strong in the whole energy range of the laser excitation from infrared up to the UV. If the confocal microscope of the spectrometer is used, we have to use a solid material for the intensity calibration. The literature proposes the use of CaF_2, which has only one Raman mode at 322 cm^{-1}. Ideally, the Raman mode used for the intensity calibration should be at similar wavenumbers compared to the Raman mode of the material that you want to probe. In CaF_2 there is only one Raman mode at medium frequencies which means we might introduce an error for the high frequency modes, in our case the A_g^8 mode. In addition, the Raman signal of CaF_2 is relatively weak especially at wavelengths in the red light region. The estimation of the Raman cross section based on a weak signal strongly depends on the fitting constraints and on the experience of the person performing the fits. Therefore, we expect an error in the resonant Raman profiles in the energy region of the red visible light that comes from the calibration with CaF_2. An alternative candidate for the intensity calibrations could be Yttrium Aluminum Oxide $YAlO_3$ with a band gap of around 8 eV and many Raman modes in the frequency range from 100 cm^{-1} to 600 cm^{-1}. Yttrium Aluminum Oxide is commonly used as a substrate material and is therefore available at high crystal quality.

In summary, we successfully established a measurement protocol to study resonant Raman effects in $BiVO_4$. A successful experiment requires a precise measurement of the Raman intensity which demands a polished sample surface. A domain structure introduces a potential risk for intensity variations due to the domain structure. In this case, the laser spot size and the domain width has to be evaluated carefully. Our line-scan measurements showed that intensity variations are not just located at the domain walls but may extend much further into the domains.

6.4.2 *Physics of resonant Raman scattering in bismuth vanadate*

With all the experimental improvements, we clearly see two resonant Raman bands in the A_g Raman modes of $BiVO_4$. The enhancement with respect to the non-resonant background is on the order of 10 which is comparable to the enhancement observed for indirect band-to-band transitions in classical semiconductors such as germanium[18] or silicon[76]. We believe that the

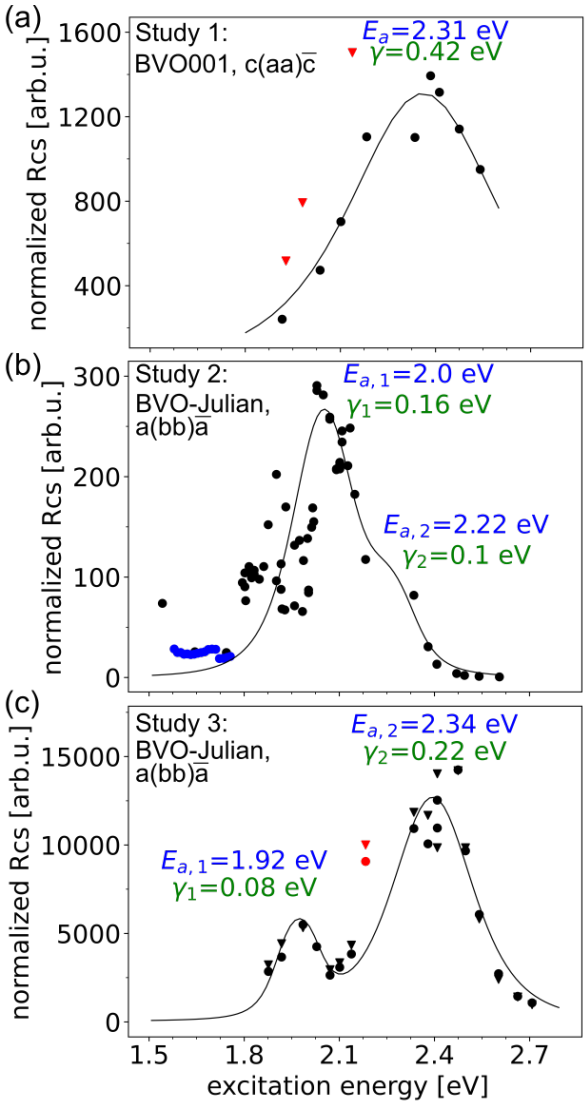

Figure 6.13: Resonant Raman profiles of the A_g^8 mode measured with a polarization direction perpendicular to the principal axis in the three different resonant Raman studies. The main resonant Raman peak is indicated by a solid line as a guide to the eyes which was calculated from the Equation 2.55. The transition energies E_a and the damping coefficients γ used in the calculation are provided in the corresponding plot.

height and the width of a resonant Raman band are directly related. Materials that show a very strong enhancement (several order of magnitude) such as GaAs[102] and zinc telluride ZnTe[17], exhibit typically a very narrow resonant Raman band. The width of the resonant Raman band is directly related to the lifetime of the excited carrier. We found a lifetime of ≈3 fs and ≈8 fs for the first and second resonant Raman band. Carrier lifetimes typically observed in transition metal oxides are typically in the range of ps.

The resonant Raman theory predicts two maxima due to the incoming and outgoing resonance. The two maxima are experimentally indistinguishable if the phonon energy in Equation 2.55 is small and the damping constant (corresponding to the linewidth) in the same equation is large. The phonon energy thereby defines the distance in energy between the two maxima. In the case of $BiVO_4$ we cannot resolve the two maxima for the same reasons. The phonon energy of all investigated Raman modes is still relatively small (≈40 meV for the A_g^4, ≈100 meV for the A_g^8 mode). Additionally, the linewidth of the second resonant Raman peaks is comparably large with ≈220 meV. In comparison, Gordeev et al.[40] could resolve the incoming and outgoing resonant Raman peak in carbon nanotubes for the high-energy G mode with phonon energy of 180 meV and narrow linewidth of 50 meV.

The second Raman band could be assigned to a band-to-band transition. We showed that by changing the polarization condition we can access different band-to-band transitions which was expected because of the strong optical anisotropy of $BiVO_4$.

To our knowledge, we observed for the first time a resonant Raman band that can be assigned to a defect level 0.42 eV below the fundamental band edge. This result was not expected from the beginning and was also not evident from the characterization by UV/Vis spectroscopy. In the literature, we found DFT calculations that suggest a polaronic defect level[19, 59] just below the absorption edge that matches the energy position of the Raman band. The polaronic defect state was experimentally observed in orthorombic $BiVO_4$ thin films[19] and in tungsten-doped $BiVO_4$ single crystals[82, 83] and thin films[22]. The DFT calculations show that the polaronic state results from an additional excess electron that localizes at the vanadium side and reduces the vanadium ion from V^{5+} to V^{4+}. The polaron causes a lattice distortion of the VO_4 tetrahedron.

Referring to the Figure 6.12 in the previous section, the different A_g modes couple with different strength to the defect level and the band-to-band transition. The A_g^8 mode seems to couple more strongly to the band-to-band transition which is visible in a stronger enhancement of the corresponding resonant Raman band. This mode corresponds to a breathing of the VO_4 tetrahedra. The bond length of the oxygen to the vanadium ion is thereby elongated. Indeed, the valence band maximum is mainly defined by the oxygen 2p orbital while the main contribution to the conduction band minimum comes from the vanadium 3d orbital.[19, 59, 109] With this knowledge, it is plausible to believe that the A_g^8 mode modulating the bond length of the V to O atom, strongly couples with the band-to-band transition.

In contrast, the A_g^4 mode seems to couple more strongly to the polaronic defect level compared to the A_g^8 mode measured at the same polarization condition, see Figure 6.12(a) versus (b) in the previous section. The A_g^4 mode corresponds to bending of the tetrahedron that results in a flattening of the VO_4 tetrahedra. The bond-length of the oxygen to the vanadium remains thereby unchanged. DFT calculations[19, 59] predict that the excess electron that forms the polaron, localizes at the vanadium site. This could be an explanation that especially these Raman modes, which affect the tetrahedra can couple to this defect state. This is true for the A_g^4, A_g^5 and the A_g^8 modes.

The coupling strength of the different vibration modes to the various electronic transitions via the resonant Raman process could be checked by DFT calculations. The research group of L. Wirtz and S. Reichardt developed a computational approach to calculate the resonant, one-phonon Raman intensities and applied this approach to various 2D materials such as monolayer MoS_2, hexagonal boron nitride[75] or single-layer and triple-layer $MoTe_2$[66].

In summary, we believe that resonant Raman scattering has the potential to reveal much more information on the electronic band structure than classical techniques such as UV/Vis spectroscopy or ellipsometry. By choosing appropriate excitation energies and polarization conditions, various electronic transitions can be distinguished and the electron-phonon coupling of each transition can be studied. We found for the first time experimental proof that defects states can couple to specific vibration modes via the resonant Raman process. Therefore, resonant Raman scattering provides us with a tool to go deeper in the analysis of defects states compared to UV/Vis spectroscopy for example.

Contributions

I would like to thank S. Reich from the Freie Universität Berlin in Germany and M. Guennou for establishing the collaboration on resonant Raman effects in $BiVO_4$. Thank you M. Guennou and G. Gordeev for performing parts of the measurements. Special thank you for G. Gordeev who prepared the measurement set-up, designed the measurement protocol and gave guidance to perform these measurements and for the data analysis.

7 SYNTHESIS

7.1 CONCLUSIONS ON THE RESEARCH QUESTIONS

***Research question 1**: Is the current understanding of the Raman spectrum sufficient to describe intensity variations by resonant Raman effects in $BiVO_4$?*

Even though the lattice vibrations across the structural phase transition are very well characterized in the literature, we discovered coupling effects in the optical phonons by Raman and inelastic neutron scattering that have not been reported yet. We found a nice example of phonon-phonon coupling of two Raman modes with the same symmetry that correspond to the vibrations of the VO_4 tetrahedron. We show that the coupling strength is strongly temperature and polarization dependent and demonstrate that the coupling diminishes at the structural phase transition where one of the phonon modes changes its symmetry. A better understanding of the phonon-phonon coupling allows for a deeper analysis of the lattice dynamics and the phonon instabilities across the ferroelastic phase transition. For this work, the main motivation to study the lattice vibrations in such detail was primarily to evaluate whether we can apply standard methods to extract the phonon characteristics from the measured spectra. The discovery of the coupling of the high-frequency Raman modes had direct implications on the calculation of the Raman cross section for the resonant Raman profiles. Whereas the coupling at room temperature is negligible in one polarization configuration, it is significant if the light polarized perpendicular to the principal axis. In this case, we had to use non-standard methods for fitting functions to estimate the Raman cross section for the Raman modes involved in the coupling.

***Research question 2**: What are the critical parameters in a resonant Raman experiment?*

In the introduction, we stated that the resonant Raman effects are very well studied for classical semiconductors and we questioned whether the methods used in the literature can directly be transferred to semiconducting oxides. The general approach in which the Raman intensity is calibrated to a transparent scatterer while sweeping through the excitation laser energies can be applied to semiconducting oxides. However, the enhancement of the Raman cross section at resonances is of the order of 10 in bismuth vanadate which is much smaller compared to the enhancement factor observed in classical semiconductors. Because of the relatively small enhancement, the resonant Raman effects are more difficult to observe experimentally and a precise measurement of the Raman intensity is key to a successful experiment. Prior to the experiment, the sample quality and morphology has to

be carefully evaluated and might be followed by sample preparation steps such as polishing or thermal treatments. The analysis is of higher complexity mainly because of the higher complexity in the crystal structure leading to a higher complexity in the Raman signal itself. In many cases, there is no reliable band structure calculation so that a direct assignment of resonant Raman bands to the electronic transitions in the band diagram is not possible. But in this discussion lies the potential of using resonant Raman scattering to probe for electronic transitions in semiconducting oxides. The higher complexity in the crystal structure very often comes with optical anisotropy and Raman selection rules that can be actively used to reveal details on the nature or the symmetry of the electronic transitions involved in the scattering process.

***Research question 3**: Can we access to different electronic transitions by varying the experimental conditions?*

In this work, we showed that the optical absorption edge is first of all strongly temperature-dependent and secondly, dependent on the polarization direction of the incident light. These material properties can indeed be used to probe for different electronic transitions. In this work, we demonstrated that by varying the polarization conditions we activated different resonant Raman bands. The strong temperature dependence provides us with another possibility to extract further details on the electronic transitions. While one transition might be strongly temperature-dependent, another might be not.

***Research question 4**: Do Raman modes of different symmetry couple to different electronic transitions?*

In the introduction, we wondered whether modes of different symmetry respond differently to resonance conditions. This research question cannot be fully answered by this work. In the monoclinic phase, we have Raman modes of A_g and B_g symmetry. While all tested A_g modes show two resonant Raman bands, we see no clear resonant Raman bands in the resonant Raman profiles of the B_g modes. We hoped to see resonant Raman bands in the response of the B_g modes that differ in energy from the Raman bands observed in the A_g modes. We speculated that these Raman bands could indicate electronic transitions that might be forbidden in an optical transition because of symmetry reasons. At this point, further measurements would be required to verify whether the B_g modes contribute or not in the resonant Raman process. The evaluation of the resonant Raman profiles of the B_g modes is particularly difficult because of their low Raman intensity and because it is difficult to measure them isolated from the A_g modes. However, we surprisingly identified differences in the coupling within the lattice modes of A_g symmetry.

***Research question 5**: Do defect states contribute to resonant Raman scattering?*

Because of the relatively high band gap, we expected defects states but it was unclear whether they contribute to a resonant Raman process or not. Our optical investigations by UV/Vis spectroscopy do not show evidence for defect levels within the band gap. The resonant Raman profiles of the A_g modes show a strong resonant Raman band at energies below the absorption edge that matches the energy of an polaronic defect state that has been reported in the literature. This result suggests that resonant Raman scattering provides us with a technique to go deeper in the analysis of defects levels than classical techniques such as UV/Vis spectroscopy or ellipsometry.

7.2 OPEN QUESTIONS AND PERSPECTIVES

Intensity calibration with a transparent scatterer

The intensity calibration to a transparent scatterer is essential to a resonant Raman experiment. If the Raman spectrometer uses a confocal microscope to focus the laser onto the sample, the transparent scatterer must be a solid wide band gap material that is available in a high quality and possesses Raman bands in the frequency range of the sample. In the literature, the single crystal CaF_2 has been used for many resonant Raman studies. Indeed, CaF_2 is sold for calibration purposes in high quality. But CaF_2 has clearly disadvantages: The main problem comes with the low Raman intensity, especially in the infrared, that introduces a large uncertainty in the resonant Raman profiles at these energies. In addition, CaF_2 has only one Raman mode in the medium-frequency range, so that an error for the high-frequency modes of the sample is expected. For future work, the identification of an alternative transparent scatterer is advised. A potential candidate could be Yttrium Aluminum Oxide with a band gap of around 8 eV and many Raman modes in the frequency range from 100 cm^{-1} to 600 cm^{-1}. Yttrium Aluminum Oxide is commonly used as a substrate for epitaxial growth and therefore available at high qualities.

Resonant Raman profiles of lattice vibrations involving the bismuth ion

We demonstrated that Raman modes corresponding to different lattice vibrations couple with different strength to the different electronic transitions involved in the scattering process. In this work, we focused on the Raman modes at medium- and high- frequency that correspond to the lattice vibrations of the VO_4 tetrahedron. DFT calculations predict that the polaronic defect is localized at the vanadium site which might be the reason why all tested Raman modes resonate with the defect level. If this hypothesis is correct, the Raman modes at low frequencies involving the bismuth ion in the lattice vibrations might not resonate with the defect level. To cross-check this hypothesis, the measurement protocol of resonant Raman study 3 could be

repeated with the small difference in measuring the low frequencies of the Raman spectrum.

Testing modes of different symmetry in a resonant Raman experiment

In monoclinic bismuth vanadate, the isolated measurement of the B_g modes is difficult from the experimental point of view. In the tetragonal phase, bismuth vanadate possesses modes of A_g, B_g and E_g symmetry. The use of an anvil pressure cell would allow us to bring the tetragonal phase down to room temperature and study the resonant Raman scattering in the tetragonal phase of bismuth vanadate. The use of an anvil pressure cell demands for a new experimental solution to perform the intensity calibration. To apply pressure, the sample is clamped between two diamonds. The Raman signal of these diamonds could be potentially used for the intensity calibration. If it can be confirmed that the B_g modes are non-resonant, the Raman cross section of the B_g modes could be used for the calibration as well. Another possibility could be to place the transparent reference scatterer on top of the anvil cell. In this case, the laser needs to be focused first on the sample and then on the reference scatterer by changing the focal point.

Reliable band structure calculations for direct assignment of resonant Raman bands

DFT calculations on bismuth vanadate are complicated because of the complexity in the crystal structure and the number of atoms per unit cell. It turned out that advanced tools are required to stabilize the correct crystal structure and that many experimental pieces of evidence are required to check the correctness of the calculations. Our collaborators D. Vincent and X. Rocquefelte have recently succeeded to calculate the phonon dispersion that is in good agreement with our Raman and inelastic neutron scattering data. From these calculations, the calculation of the band structure and the calculations of the resonant Raman intensities by first-principles methods could be anticipated and could help us to finally assign the experimental features that we observed.

Part II

APPENDIX

A

DEFINITION OF THE OPTICAL ABSORPTION EDGE

Parts of the work presented in the appendix have been published in APL Materials 8, 081108 (2020) under a Creative Commons Attribution (CC BY) license.[47] Major parts are identical in content and word with the supplementary information of the publication. The text that is identical in words with the supplementary information are placed in between the following symbols ★/..../★.

A.1 DEFINITIONS OF THE ABSORPTION EDGE

There are different analytical methods to determine the absorption edge from optical measurements. In this appendix we compare different methods and demonstrate that our conclusions expressed in the Section 5.1 do not depend on the choice of the method. Here, we neglect the small non-linearities in the evolution of the absorption edge in the monoclinic low-symmetry phase.

A.1.1 *Inflexion point of the transmittance curve*

In the section 5.1, we defined the absorption edge as the inflexion point of the transmittance curve. Figure A.1 shows the transmittance spectra and their first derivatives for (a) the (110)-oriented sample and (b) the (001)-oriented sample for two different light polarizations measured at room temperature.

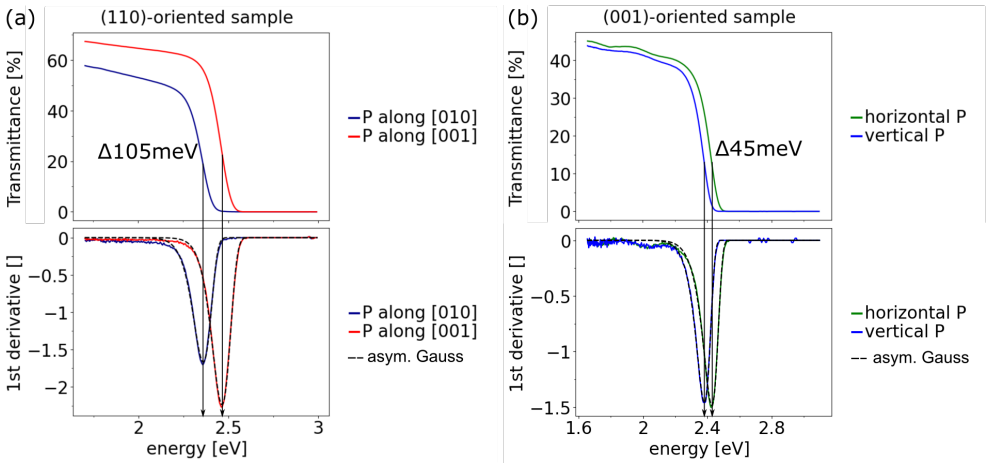

Figure A.1: Transmittance spectra and their first derivatives for (a) the (110)-oriented and (b) the (001)-oriented sample. The absorption edges are extracted by fitting the first derivatives with an asymmetric Gaussian.

The inflexion point have been extracted by fitting the first derivatives with a Gaussian function with asymmetric linewidth σ [95].

$$G(\hbar\omega) = \frac{I_0}{\sigma\sqrt{2\Pi}} exp\Big[- \frac{(\hbar\omega - \hbar\omega_0)^2}{2\sigma^2}\Big] \tag{A.1}$$

with I_0 being the amplitude and E_0 being the absorption edge or the centering of the Gaussian function. The non-constant linewidth is defined as

$$\sigma = \frac{\sigma_0}{1 + exp(a(\hbar\omega - \hbar\omega_0))} \tag{A.2}$$

in which a is a measure for the asymmetry. At room temperature, we found a maximum difference of 105 meV for the (110)-oriented sample and 45 meV for the (001)-oriented sample.

Figure A.2 shows the absorption edge versus the temperature for the (a) (110)-oriented and the (b) (001)-oriented sample. The solid line are linear fits through the data. We used separate fits below and above T_c, and extrapolated to 0 K.

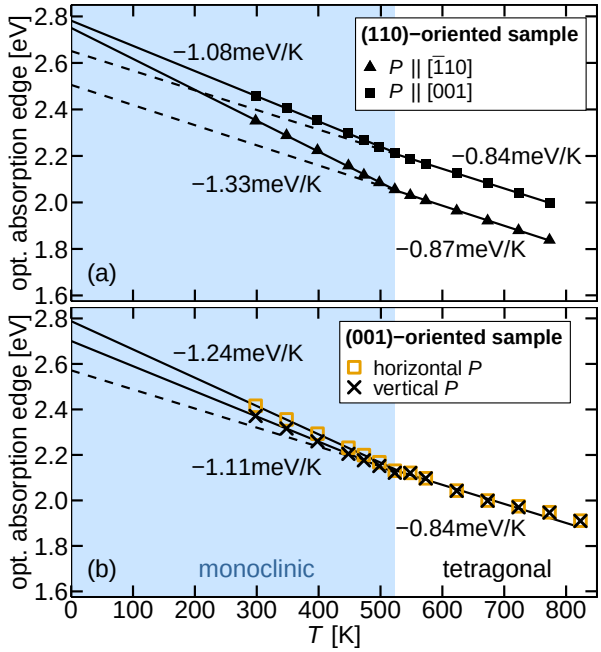

Figure A.2: Temperature dependence of the optical absorption edge for (a) the (110)-oriented and (b) the (001)-oriented sample. The absorption edges are extracted as the inflexion point of the transmittance spectra. The figure has been published in [47].

A.1.2 *Constant threshold*

★/ Another way to define an absorption edge is to use the energy corresponding to a fixed - and arbitrary - threshold in transmittance, as it is done for example in Ref. [46]. The drawback of this method is that the

extracted value depends on the sample thickness. Here, we show in Figure A.3 the absorption edge deduced at a transmittance value of 1 % for the a) (110)-oriented sample and the b) (001)-oriented sample as a function of temperature./★

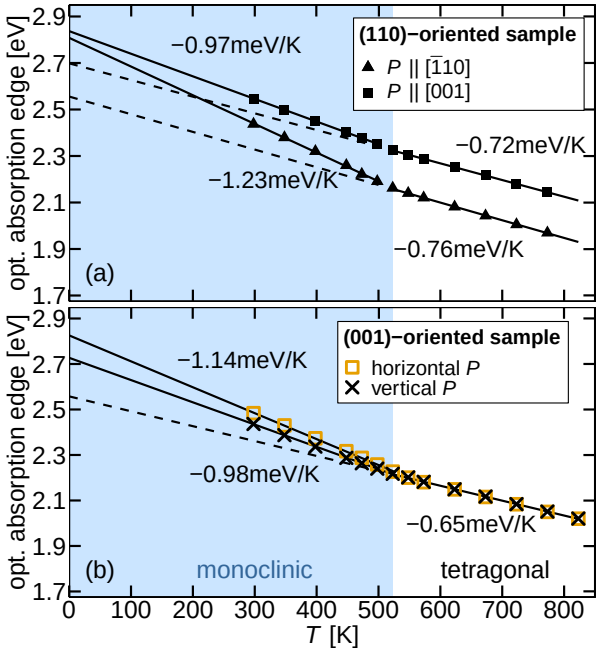

Figure A.3: Temperature dependence of the optical absorption edge for (a) the (110)-oriented and (b) the (001)-oriented sample: The absorption edge is deduced at a transmittance value of 1 %. The figure has been published in [47].

A.1.3 *Tauc plot*

In this section, we give the absorption edges deduced by the use of a so-called Tauc plot which is described in details in section 2.2.1.2. The drawback of this method is that it requires knowledge about the nature of the involved interband optical absorption. Figure A.4 shows the absorption edge extracted from the Tauc plot assuming an indirect band-to-band transition for both samples as a function of temperature.

★/ In all cases, the main conclusions are identical: the tetragonal phase exhibits the same anisotropy, the influence of the phase transition is clearly seen as a kink, and the fundamental absorption edge is found for light polarized perpendicular to the principal axis. The insignificant differences are an offset of the absolute values, and some changes in the values for the slopes. /★

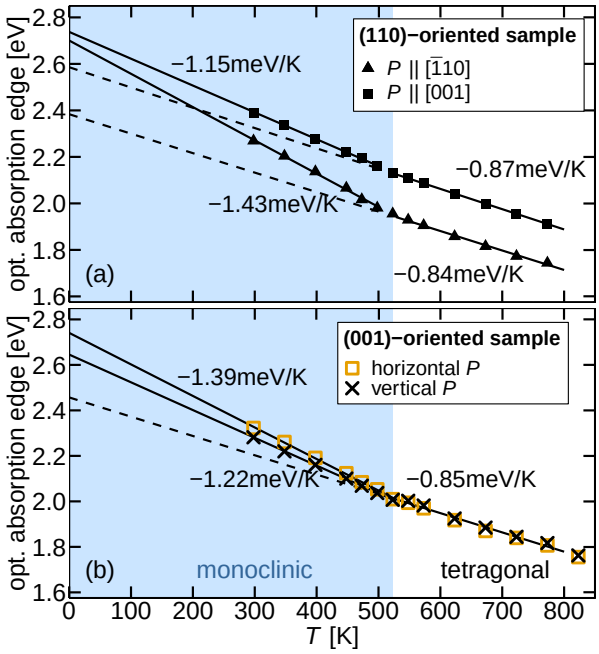

Figure A.4: Temperature-dependence of the optical absorption for (a) the (110)-oriented sample and (b) the (001)-oriented sample: The absorption edge is extracted from the Tauc plot assuming an indirect transition. The figure has been published in [47].

B

FIT OF LOW TEMPERATURE DATA AND EXTRAPOLATIONS TO 0 K

Parts of the work presented the appendix have been published in APL Materials 8, 081108 (2020) under a Creative Commons Attribution (CC BY) license.[47] Major parts are identical in content and word with the supplementary information of the publication. The text that is identical in words with the supplementary information are placed in between the following symbols ★/..../★.

B.1 EXTRAPOLATION TO LOW TEMPERATURES

★/ In the tetragonal high-temperature phase, the absorption edge as a function of temperature is well described by a linear fit. However, at low temperatures the evolution of the absorption edge is expected to deviate from linearity. A first cause of non-linearity is the dependence on spontaneous strain. As described in section 5.1, we describe this by a power-law

$$\Delta E_{\mathrm{opt}} = A(T_c - T)^{\beta}$$

derived from Landau theory, where T_c is the critical temperature and A, β are fitting constants. For the fitting, T_c has been fixed to 523 K corresponding to the phase transition temperature of $BiVO_4$.

In addition, other causes of non-linearly can be expected.[103] To describe the saturation at low temperatures T, we fitted the experimental data in the monoclinic phase with different functions. Since we lack data at low temperatures, we could not reasonably fit all parameters. Instead we use here physical arguments to estimate and fix some of the required parameters.

First, we consider the Varshni function, an empirical function often used for classical semiconductors

$$E_g(T) = E_g(0) - \alpha T^2/(T + T_0)$$

where E_g is the direct or indirect band gap, $E_g(0)$ the band gap at 0 K and α the Varshni coefficient.[104] The parameter T_0 defines the temperature range over which the function saturates at low temperatures, and is found to be of the order of the Debye temperature Θ_D.[70] Here, we simply assume that T_0 is equal to Θ_D. Considering the highest vibrational mode in $BiVO_4$ of 830 cm^{-1}, the Debye temperature is estimated to be 1200 K.

Second, we consider the Bose-Einstein function that takes into account the electron-phonon interaction

$$E_g(T) = E_g(0) - \frac{2a_B}{\exp(\Theta_E/T) - 1}$$

where a_B is a measure for the electron-phonon coupling in the crystal and Θ_E is the average temperature of the phonon interaction[70] and marks the temperature range where E_g saturates. Following the comparison shown in Ref. [70], we fixed Θ_E to 900 K from the following relation $\Theta_D = 4\Theta_E/3$.

Fig. B.1 shows the absorption edge deduced from the Tauc plot assuming an indirect band gap for $P \parallel [\bar{1}10]$ in the monoclinic phase, which is the fundamental absorption edge. The extrapolations are shown for each of the functions described above, and the values at 0 K are shown in Table B.1. We conclude that the low-temperature effects could lead to a lowering of the band-gap value by as much as 0.3 eV./★

Table B.1: Fundamental absorption edge at 0 K obtained by extrapolation with different fitting functions. The table has been published in [47].

Fitting function	E_{opt} [eV] @ $T = 0\,K$
linear fit	2.70
power-law fit	2.62
Varshni fit	2.47
Bose-Einstein fit	2.37

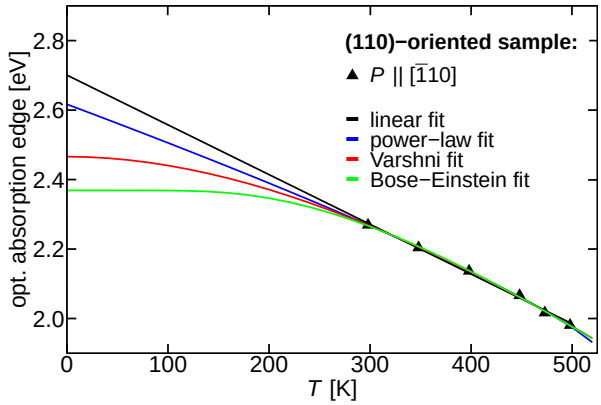

Figure B.1: Optical absorption edge in the monoclinic low-temperature phase measured on the (110)-oriented sample, with extrapolations down to 0 K. The figure has been published in [47].

C

RESONANT RAMAN STUDIES

C.1 FIRST RESONANT RAMAN STUDY ON THE SAMPLE BVO001-ANDREAS IN MICRO MODE

C.1.1 *Extraction of the Raman cross section*

The Raman cross section is extracted by fitting the data with multiple Lorentzian functions. Here, we show the Raman spectra measured on the single crystal sample *BVO001-Andreas* and on the transparent scatterer CaF_2 together with the best fits at multiple laser wavelengths.

C.1.1.1 *Raman cross section of A_g modes in bismuth vanadate*

Figure C.1 shows the $BiVO_4$ Raman spectra measured on the sample *BVO001-Andreas* at room temperature at different laser excitation wavelengths for parallel light polarization. For parallel polarization geometries only A_g modes are expected and observed. The Raman spectra are divided into three frequency ranges; (a) from 45 to 300 cm^{-1}, (b) from 300 to 600 cm^{-1} and (c) from 450 to 950 cm^{-1}. Each frequency range is fitted with multiple Lorentzian function. The background signal is modeled with a constant or in some cases with a linear baseline. The Raman cross section of an individual Raman mode is given by the integrated intensity below the corresponding Lorentzian function.

The Lorentzian function provides a sufficiently good fit to almost all A_g modes. Exceptions are the A_g^1 soft mode, the A_g^2 and the A_g^7 mode. The frequency position of the A_g^1 soft mode is relatively low at 60 cm^{-1}. The low intensity tail of the soft mode is not sufficiently resolved with the measurement configuration used in this experiment, leading to high error for the fitting of this particular mode for some laser wavelengths. In case of the A_g^2 and the A_g^7 mode, phonon-phonon coupling has been observed that is strongly temperature dependent, see discussion on section **??**. At room temperature, the Lorentzian function can only be seen as a first approximation because lineshape asymmetries are expected because of the phonon-phonon coupling.

C.1.1.2 *Raman cross section of B_g modes in bismuth vanadate*

Figure C.2 shows $BiVO_4$ Raman spectra measured on the sample *BVO001-Andreas* at room temperature at different laser wavelengths for cross polarisation. In cross polarisation only Raman modes of B_g symmetry are expected due to the selection rules. We observe the B_g^4 at 143 cm^{-1}, the B_g^6 at 279 cm^{-1}, the B_g^9 at 638 cm^{-1} and the B_g^{10} at 736 cm^{-1} together with A_g modes leaking

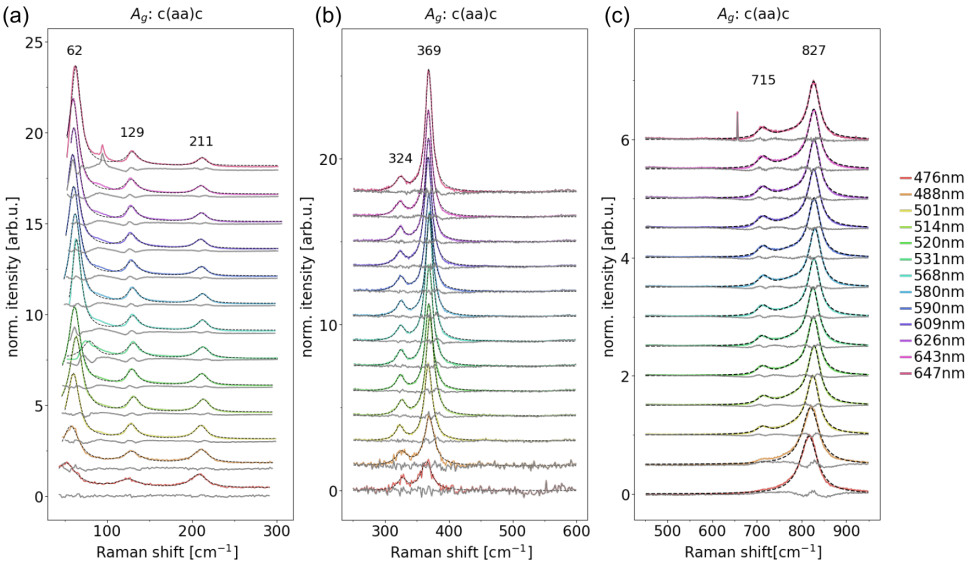

Figure C.1: $BiVO_4$ Raman spectra measured on the sample *BVO001-Andreas* for light polarization for light polarization $c(aa)c$ at room temperature at different laser excitation wavelengths. The dashed black line are fits consisting of multiple Lorentzian function and constant or linear baseline. The solid gray line is the error (data minus fit). All spectra are normalized to the A_g^2 mode at 129 cm^{-1} for the low frequency range (a), to the A_g^4 mode at 326 cm^{-1} for the medium frequency range (b) and to the A_g^8 mode at 828 cm^{-1} for the high frequency range (c). All spectra are calibrated with silicon for the correct frequency position.

into the spectra. The B_g^4 at 143 cm^{-1} and the B_g^9 at 638 cm^{-1} are well isolated and best suitable to study the resonant Raman effects for the Raman modes of B_g symmetry in $BiVO_4$. Raman cross section is given by the integrated intensity under the Lorentzian.

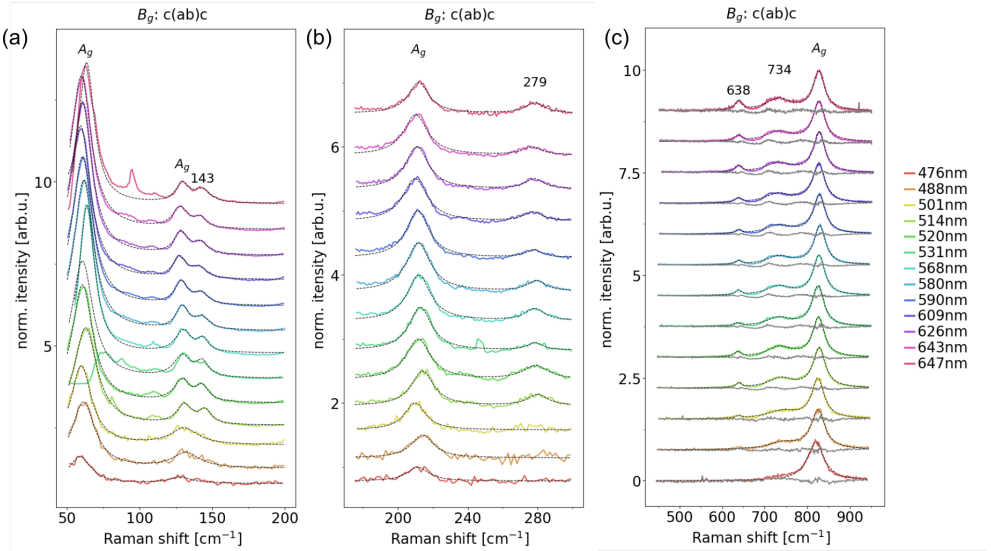

Figure C.2: $BiVO_4$ Raman spectra measured at room temperature on sample *BVO001-Andreas* with $c(ab)c$ at different laser excitation wavelengths. The dashed black line are fits consisting of multiple Lorentzian function and constant baseline. All spectra are normalized to the $A_{g,2}$ mode at 129 cm^{-1} for the low frequency range (a), to the $A_{g,3}$ mode at 212 cm^{-1} for the medium frequency range (b) and to the $A_{g,8}$ mode at 828 cm^{-1} for the high frequency range (c). All spectra are calibrated with silicon for the correct frequency position.

C.1.1.3 *Raman cross section of transparent scattered calcium fluoride*

Figure C.3 shows the Raman spectra of the transparent scatterer CaF_2 measured at room temperature at different laser wavelengths for (a) parallel and (b) cross polarisation. All spectra are calibrated with silicon for the correct frequency position and normalized to the Raman mode at 322 cm^{-1}. The data have been fitted with a single Lorentzian function and constant baseline for parallel and linear baseline for cross polarisation. The Raman intensity, especially for the cross polarisation and for the laser excitation in the UV, is relatively low despite long acquisition time (300 s or 600 s. For the laser excitation at 476 nm, the Raman mode at 322 cm^{-1} was not visible at all. Also, here the Raman cross section is given by the integrated intensity under the Lorentzian.

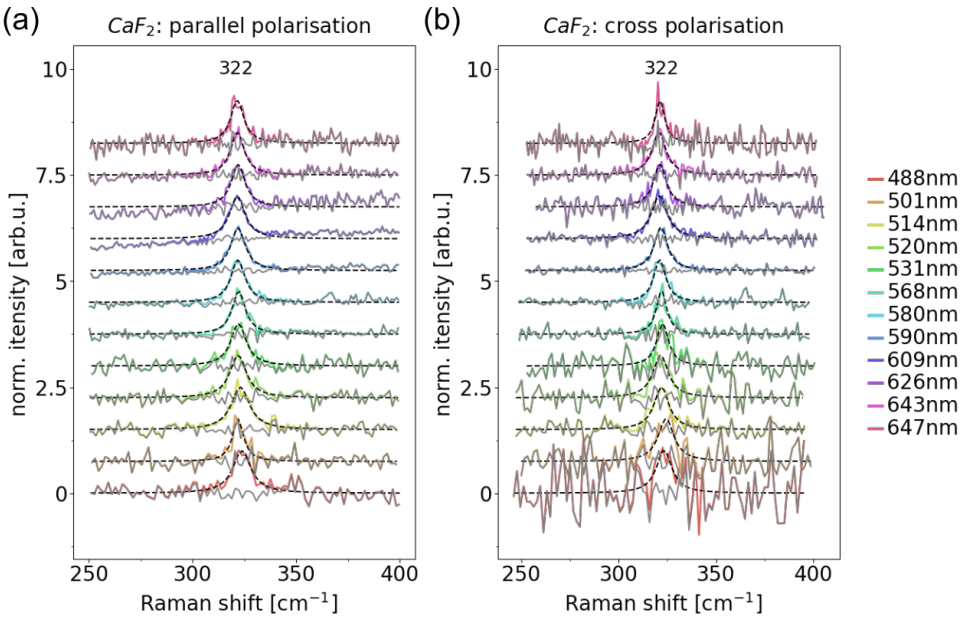

Figure C.3: Raman spectra of the transparent scatterer CaF_2 measured at room temperature at different laser excitation wavelengths for (a) parallel polarisation and (b) cross polarisation. All spectra are calibrated with silicon for the correct frequency position and normalized to the Raman mode at 322 cm^{-1}. The dashed black line is the best fit to the data using a single Lorentzian function and constant baseline for parallel and linear baseline for cross polarisation. Here, we subtracted the baseline from the data and the fit.

C.2 SECOND RESONANT RAMAN STUDY ON THE SAMPLE BVO100-JULIAN IN MACRO MODE

C.2.1 *Resonant Raman profiles*

C.2.1.1 *Resonant Raman profiles of A_g modes*

Figure C.4 shows the resonant Raman profiles of the Raman modes with A_g symmetry measured on the sample *BVO100-Julian* using the macro compartment of the Horiba Raman Spectrometer. Here, the Raman modes from the medium frequency range A_g^4, A_g^5 and A_g^6 are shown measured at two different light polarizations $a(bb)a$ and $a(cc)a$. All resonant Raman profiles show a resonant peak at energies ranging from 2.03 eV to 2.1 eV. At energies below the resonant peak, the data scattering is relatively large. The intensity of the Raman modes in the medium frequency range is much lower compared the intensity of the A_g^8 mode discussed in the main text. Because of the low intensity, these Raman bands at medium frequencies are not always visible, especially for excitations at high energy. That is why, we have a limited number of data at energies above the resonant peak. In the main test, we discussed an additional resonant peak at higher energies around 2.38 eV that is not visible on the resonant Raman profiles shown here.

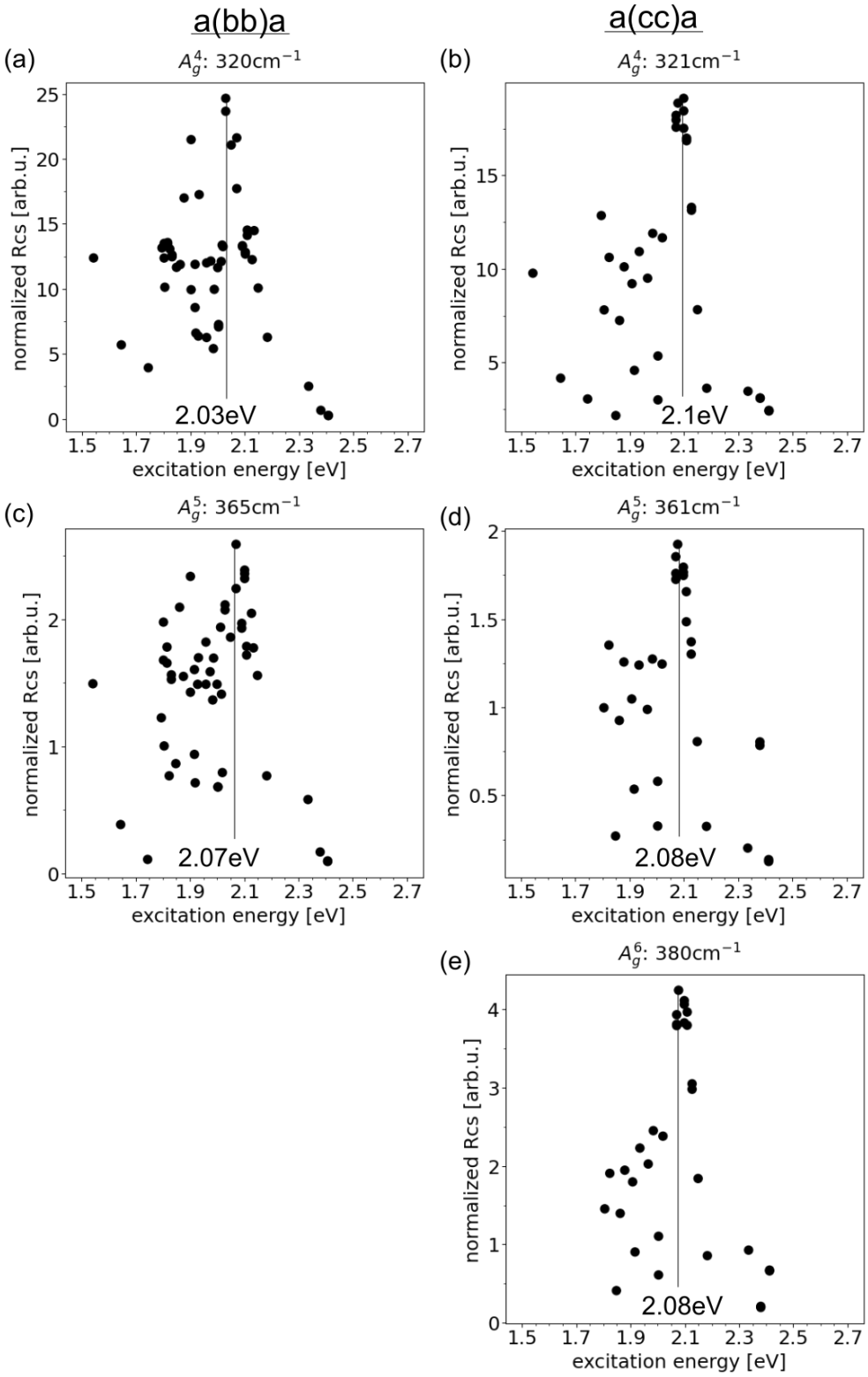

Figure C.4: Resonant Raman profiles of Raman modes with A_g symmetry measured on the sample *BVO100-Julian* for the light polarisation (a), (c) $a(bb)a$ and (b),(d),(e) $a(cc)a$.

BIBLIOGRAPHY

[1] Fatwa F. Abdi, Lihao Han, Arno H. M. Smets, Miro Zeman, Bernard Dam, and Roel van de Krol. "Efficient solar water splitting by enhanced charge separation in a bismuth vanadate-silicon tandem photoelectrode." In: *Nature Communications* 4.1 (Oct. 2013), p. 2195. ISSN: 2041-1723. DOI: 10.1038/ncomms3195.

[2] *Advanced characterization techniques for thin film solar cells /*. Second edition. Weinheim, Germany: Wiley-VCH Verlag GmbH Co. KGaA, 2016 - 2016. ISBN: 9783527699018.

[3] Kêitsiro Aizu. "Determination of the State Parameters and Formulation of Spontaneous Strain for Ferroelastic." In: *Journal of the Physical Society of Japan* 28.3 (Mar. 1970).

[4] Audrius Alkauskas, Matthew D. McCluskey, and Chris G. Van de Walle. "Tutorial: Defects in semiconductors—Combining experiment and theory." In: *Journal of Applied Physics* 119.18 (May 14, 2016), p. 181101. ISSN: 0021-8979, 1089-7550. DOI: 10.1063/1.4948245.

[5] Jakob Andreasson, Joakim Holmlund, Christopher S. Knee, Mikael Käll, Lars Börjesson, Stefan Naler, Joakim Bäckström, Michael Rübhausen, Abul Kalam Azad, and Sten-G. Eriksson. "Franck-Condon higher order lattice excitations in the $LaFe_{1x}Cr_xO_3$ (x=0, 0.1, 0.5, 0.9, 1.0) perovskites due to Fe-Cr charge transfer effects." In: *Physical Review B* 75.10 (Mar. 9, 2007), p. 104302. ISSN: 1098-0121, 1550-235X. DOI: 10.1103/PhysRevB.75.104302.

[6] Jakob Andreasson et al. "Electron-lattice interactions in the perovskite $LaFe_{0.5}Cr_{0.5}O_3$ characterized by optical spectroscopy and LDA+U calculations." In: *Physical Review B* 80.7 (Aug. 4, 2009), p. 075103. ISSN: 1098-0121, 1550-235X. DOI: 10.1103/PhysRevB.80.075103.

[7] L. P. Avakyants, A. V. Chervyakov, V. S. Gorelik, and P. P. Sverbil'. "Inelastic Light Scattering Near the Ferroelectric Phase-Transition Point in Bismuth Vanadate Crystals." In: *Journal of Russian Laser Research* 25.6 (Nov. 2004), pp. 535–580. ISSN: 1071-2836. DOI: 10.1023/B:JORR.0000049086.09037.b3.

[8] A. S. Barker and J. J. Hopfield. "Coupled-Optical-Phonon-Mode Theory of the Infrared Dispersion in $BaTiO_3$, $SrTiO_3$, and $KTaO_3$." In: *Physical Review* 135.6 (Sept. 14, 1964), A1732–A1737. ISSN: 0031-899X. DOI: 10.1103/PhysRev.135.A1732.

[9] Gu Benyuan, M. Copic, and H. Z. Cummins. "Soft acoustic mode in ferroelastic $BiVO_4$." In: *Phys. Rev. B* 24 (7 1981), pp. 4098–4100. DOI: 10.1103/PhysRevB.24.4098.

[10] J.D. Bierlein and A.W. Sleight. "Ferroelasticity in $BiVO_4$." In: *Solid State Communications* 16.1 (Jan. 1975), pp. 69–70. ISSN: 00381098. DOI: 10.1016/0038-1098(75)90791-7.

[11] Bilbao, ed. *Bilbao Crystallographic Server*. 1997. URL: https://www.cryst.ehu.es/ (visited on 03/17/2023).

[12] P H Borcherds, R L Hall, K Kunc, and G F Alfrey. "The lattice dynamics of gallium phosphide." In: *Journal of Physics C: Solid State Physics* 12.22 (Nov. 28, 1979), pp. 4699–4706. ISSN: 0022-3719. DOI: 10.1088/0022-3719/12/22/012.

[13] Pauline Bornoz, Fatwa F. Abdi, S. David Tilley, Bernard Dam, Roel van de Krol, Michael Graetzel, and Kevin Sivula. "A Bismuth Vanadate–Cuprous Oxide Tandem Cell for Overall Solar Water Splitting." In: *The Journal of Physical Chemistry C* 118.30 (July 2014), pp. 16959–16966. ISSN: 1932-7447, 1932-7455. DOI: 10.1021/jp500441h.

[14] S. D. M. Brown, P. Corio, A. Marucci, M. S. Dresselhaus, M. A. Pimenta, and K. Kneipp. "Anti-Stokes Raman spectra of single-walled carbon nanotubes." In: *Physical Review B* 61.8 (Feb. 15, 2000), R5137–R5140. ISSN: 0163-1829, 1095-3795. DOI: 10.1103/PhysRevB.61.R5137.

[15] J. M. Calleja and Manuel Cardona. "Resonant Raman scattering in ZnO." In: *Physical Review B* 16.8 (Oct. 15, 1977), pp. 3753–3761. ISSN: 0556-2805. DOI: 10.1103/PhysRevB.16.3753.

[16] J. M. Calleja, J. Kuhl, and M. Cardona. "Resonant Raman scattering in diamond." In: *Physical Review B* 17.2 (Jan. 15, 1978), pp. 876–883. ISSN: 0163-1829. DOI: 10.1103/PhysRevB.17.876.

[17] Manuel Cardona, ed. *Light scattering in solids II: Basic concepts and instrumentation*. Topics in applied physics 50. Berlin: Springer, 1982. 251 pp. ISBN: 978-3-540-11380-5 978-0-387-11380-7.

[18] F. Cerdeira, W. Dreybrodt, and Manuel Cardona. "Resonant Raman scattering in germanium." In: *Solid State Communications* 10.7 (Apr. 1972), pp. 591–595. ISSN: 00381098. DOI: 10.1016/0038-1098(72)90598-4.

[19] A. Chaudhuri et al. "Direct observation of anisotropic small-hole polarons in an orthorhombic structure of $BiVO_4$ films." In: *Physical Review B* 97.19 (May 25, 2018), p. 195150. ISSN: 2469-9950, 2469-9969. DOI: 10.1103/PhysRevB.97.195150.

[20] A. Chaves, R. S. Katiyar, and S. P. S. Porto. "Coupled modes with A1 symmetry in tetragonal $BaTiO_3$." In: *Physical Review B* 10.8 (Oct. 15, 1974), pp. 3522–3533.

[21] Le Chen, Esther Alarcón-Lladó, Mark Hettick, Ian D. Sharp, Yongjing Lin, Ali Javey, and Joel W. Ager. "Reactive Sputtering of Bismuth Vanadate Photoanodes for Solar Water Splitting." In: *The Journal of Physical Chemistry C* 117.42 (Oct. 2013), pp. 21635–21642. ISSN: 1932-7447, 1932-7455. DOI: 10.1021/jp406019r.

[22] Xiao Chi et al. "Unravelling a new many-body large-hole polaron in a transition metal oxide that promotes high photocatalytic activity." In: *NPG Asia Materials* 14.1 (Dec. 2022), p. 19. ISSN: 1884-4049, 1884-4057. DOI: 10.1038/s41427-022-00364-w.

[23] Sung Ho Choh and Min Su Jang. "Domain structure and magnetic resonance studies of ferroelastic $BiVO_4$ revisited." In: *Materials Research Express* 3.4 (Apr. 2016), p. 045021. ISSN: 2053-1591. DOI: 10.1088/2053-1591/3/4/045021.

[24] Jason K. Cooper, Sheraz Gul, Francesca M. Toma, Le Chen, Yi-Sheng Liu, Jinghua Guo, Joel W. Ager, Junko Yano, and Ian D. Sharp. "Indirect Bandgap and Optical Properties of Monoclinic Bismuth Vanadate." In: *The Journal of Physical Chemistry C* 119.6 (Feb. 2015), pp. 2969–2974. ISSN: 1932-7447, 1932-7455. DOI: 10.1021/jp512169w.

[25] Jason K. Cooper, Soren B. Scott, Yichuan Ling, Jinhui Yang, Sijie Hao, Yat Li, Francesca M. Toma, Martin Stutzmann, K. V. Lakshmi, and Ian D. Sharp. "Role of Hydrogen in Defining the n-Type Character of $BiVO_4$ Photoanodes." In: *Chemistry of Materials* 28.16 (Aug. 23, 2016), pp. 5761–5771. ISSN: 0897-4756, 1520-5002. DOI: 10.1021/acs.chemmater.6b01994.

[26] Tilak Das, Xavier Rocquefelte, Robert Laskowski, Luc Lajaunie, Stéphane Jobic, Peter Blaha, and Karlheinz Schwarz. "Investigation of the Optical and Excitonic Properties of the Visible Light-Driven Photocatalytic $BiVO_4$ Material." In: *Chemistry of Materials* 29.8 (Apr. 2017), pp. 3380–3386. ISSN: 0897-4756, 1520-5002. DOI: 10.1021/acs.chemmater.6b02261.

[27] W I F David. "Ferroelastic phase transition in $BiVO_4$: III. Thermodynamics." In: *Journal of Physics C: Solid State Physics* 16.26 (Sept. 1983), pp. 5093–5118. ISSN: 0022-3719. DOI: 10.1088/0022-3719/16/26/006.

[28] W I F David. "Ferroelastic phase transition in $BiVO_4$: IV. Relationships between spontaneous strain and acoustic properties." In: *Journal of Physics C: Solid State Physics* 16.26 (Sept. 1983), pp. 5119–5126. ISSN: 0022-3719. DOI: 10.1088/0022-3719/16/26/007.

[29] W. I. F. David, A. M. Glazer, and A. W. Hewat. "The structure and ferroelastic phase transition of $BiVO_4$." In: *Phase Transitions* 1.2 (Dec. 1979), pp. 155–169. ISSN: 0141-1594, 1029-0338. DOI: 10.1080/01411597908213198.

[30] W I F David and I G Wood. "Ferroelastic phase transition in $BiVO_4$: V. Temperature dependence of Bi^{3+} displacement and spontaneous strains." In: *Journal of Physics C: Solid State Physics* 16.26 (Sept. 1983), pp. 5127–5148. ISSN: 0022-3719. DOI: 10.1088/0022-3719/16/26/008.

[31] W I F David and I G Wood. "Ferroelastic phase transition in $BiVO_4$: VI. Some comments on the relationship between spontaneous deformation and domain walls in ferroelastics." In: *Journal of Physics C: Solid State Physics* 16.26 (Sept. 20, 1983), pp. 5149–5166. ISSN: 0022-3719. DOI: 10.1088/0022-3719/16/26/009.

[32] W I F David and I G Wood. "Ferroelastic phase transition in $BiVO_4$: V. Temperature dependence of Bi^{3+} displacement and spontaneous strains." In: *Journal of Physics C: Solid State Physics* 16.26 (Sept. 1983), pp. 5127–5148. ISSN: 0022-3719. DOI: 10.1088/0022-3719/16/26/008.

[33] E. A. Davis and N. F. Mott. "Conduction in non-crystalline systems V. Conductivity, optical absorption and photoconductivity in amorphous semiconductors." In: *Philosophical Magazine* 22.179 (Nov. 1970), pp. 0903–0922. ISSN: 0031-8086. DOI: 10.1080/14786437008221061.

[34] Kaining Ding, Bin Chen, Zhenxing Fang, and Yongfan Zhang. "Density functional theory study on the electronic and optical properties of three crystalline phases of $BiVO_4$." In: *Theoretical Chemistry Accounts* 132.5 (May 2013). ISSN: 1432-881X, 1432-2234. DOI: 10.1007/s00214-013-1352-x.

[35] Perkin Elmer. *LAMBDA UV/Vis and UV/Vis/NIR Spectrophotometers*. URL: https://laboaragon.com/docs/marcas/perkin-elmer/UV-VIS%20Lambda%20850%20&%20UV-VIS-NIR%20Lambda%20950%20-%20Lambda%201050%20.pdf (visited on 01/24/2023).

[36] Perkin Elmer. *Measuring Absorptance (k) and Refractive Index (n) of Thin Films with the PerkinElmer LAMBDA 1050+ High Performance UV/Vis/NIR Spectrometers*. URL: https://resources.perkinelmer.com/lab-solutions/resources/docs/APP_Thin-films.pdf?_ga=2.104357961.878401803.1674465641-2136496206.1674465641&_gac=1.242494134.1674465752.EAIaIQobChMItNzi6q7d_AIVhfZ3Ch2BZwYjEAAYBCAAEgLggfD_BwE (visited on 01/24/2023).

[37] U. Filges, H.M. Rønnow, and G. Zsigmond. "Monte Carlo simulations for instrumentation at SINQ." In: *Physica B: Condensed Matter* 385-386 (Nov. 2006), pp. 1346–1348. ISSN: 09214526. DOI: 10.1016/j.physb.2006.06.073.

[38] G. de la Flor, M. Wehber, A. Rohrbeck, M. I. Aroyo, U. Bismayer, and B. Mihailova. "Resonance Raman scattering of perovskite-type relaxor ferroelectrics under nonambient conditions." In: *Physical Review B* 90.6 (Aug. 12, 2014), p. 064107. ISSN: 1098-0121, 1550-235X. DOI: 10.1103/PhysRevB.90.064107.

[39] Mark Fox. *Optical properties of solids*. Oxford, England : Oxford University Press, 2010. ISBN: 9780199573363.

[40] Georgy Gordeev, Ado Jorio, Patryk Kusch, Bruno G. M. Vieira, Benjamin Flavel, Ralph Krupke, Eduardo B. Barros, and Stephanie Reich. "Resonant anti-Stokes Raman scattering in single-walled carbon nanotubes." In: *Physical Review B* 96.24 (Dec. 18, 2017), p. 245415. ISSN: 2469-9950, 2469-9969. DOI: 10.1103/PhysRevB.96.245415.

[41] M. Grimsditch, M. Cardona, J. M. Calleja, and F. Meseguer. "Resonance in the Raman scattering of CaF_2, SrF_2, BaF_2 and diamond." In: *Journal of Raman Spectroscopy* 10.1 (Jan. 1981), pp. 77–81. ISSN: 03770486. DOI: 10.1002/jrs.1250100113.

[42] Marius Grundmann. *The Physics of Semiconductors: An Introduction Including Nanophysics and Applications*. Graduate Texts in Physics. Cham: Springer International Publishing, 2016. ISBN: 978-3-319-23879-1 978-3-319-23880-7. DOI: 10.1007/978-3-319-23880-7.

[43] Lihao Han, Fatwa F. Abdi, Roel vandeKrol, Rui Liu, Zhuangqun Huang, Hans-Joachim Lewerenz, Bernard Dam, Miro Zeman, and Arno H. M. Smets. "Efficient Water-Splitting Device Based on a Bismuth Vanadate Photoanode and Thin-Film Silicon Solar Cells." In: *ChemSusChem* 7.10 (Oct. 2014), pp. 2832–2838. ISSN: 18645631. DOI: 10.1002/cssc.201402456.

[44] William Hayes and Rodney Loudon. *Scattering of Light by Crystals*. Mineola, New York: Dover Publications, Inc, 1978. ISBN: 0-486-43866-X.

[45] R. M. Hazen and J. W. E. Mariathasan. "Bismuth Vanadate: A High-Pressure, High-Temperature Crystallographic Study of the Ferroelastic-Paraelastic Transition." In: *Science* 216.4549 (May 28, 1982), pp. 991–993. ISSN: 0036-8075, 1095-9203. DOI: 10.1126/science.216.4549.991.

[46] W. Heiss, R. Kirchschlager, G. Springholz, Z. Chen, M. Debnath, and Y. Oka. "Magnetic polaron induced near-band-gap luminescence in epitaxial EuTe." In: *Physical Review B* 70.3 (July 2004), p. 035209. ISSN: 1098-0121, 1550-235X. DOI: 10.1103/PhysRevB.70.035209.

[47] Christina Hill, Mads C. Weber, Jannis Lehmann, Tariq Leinen, Manfred Fiebig, Jens Kreisel, and Mael Guennou. "Role of the ferroelastic strain in the optical absorption of $BiVO_4$." In: *APL Materials* 8.8 (Aug. 1, 2020), p. 081108. ISSN: 2166-532X. DOI: 10.1063/5.0011507.

[48] Philip Hofmann. *Solid State Physics, An Introduction*. Wiley$_V$*CH*, 2015. ISBN: 978-3-527-41282-2.

[49] Didier Hutsebaut, Peter Vandenabeele, and Luc Moens. "Evaluation of an accurate calibration and spectral standardization procedure for Raman spectroscopy." In: *The Analyst* 130.8 (2005), p. 1204. ISSN: 0003-2654, 1364-5528. DOI: 10.1039/b503624k.

[50] Harald Ibach and Hans Lüth. *Solid-State Physics: An Introduction to Principles of Materials Science*. Berlin, Heidelberg: Springer Berlin Heidelberg, 2009. ISBN: 978-3-540-93803-3 978-3-540-93804-0. DOI: 10.1007/978-3-540-93804-0.

[51] *International tables for crystallography*. Chichester, 1983.

[52] A. Jorio, ed. *Raman spectroscopy in graphene related systems*. Weinheim, Germany: Wiley-VCH, 2011. 354 pp. ISBN: 978-3-527-40811-5.

[53] R. S. Katiyar, J. F. Ryan, and J. F. Scott. "Proton-Phonon Coupling in CsH_2AsO_4 and KH_2AsO_4." In: *Physical Review B* 4.8 (Oct. 15, 1971), pp. 2635–2638. ISSN: 0556-2805. DOI: 10.1103/PhysRevB.4.2635.

[54] Yoshiaki Kato and Hiroshi Takuma. "Absolute Measurement of Raman-Scattering Cross Sections of Liquids." In: *Journal of the Optical Society of America* 61.3 (Mar. 1, 1971), p. 347. ISSN: 0030-3941. DOI: 10.1364/JOSA.61.000347.

[55] Bernt Ketterer, Martin Heiss, Emanuele Uccelli, Jordi Arbiol, and Anna Fontcuberta i Morral. "Untangling the Electronic Band Structure of Wurtzite GaAs Nanowires by Resonant Raman Spectroscopy." In: *ACS Nano* 5.9 (Sept. 27, 2011), pp. 7585–7592. ISSN: 1936-0851, 1936-086X. DOI: 10.1021/nn202585j.

[56] P. Klar, E. Lidorikis, A. Eckmann, I. A. Verzhbitskiy, A. C. Ferrari, and C. Casiraghi. "Raman scattering efficiency of graphene." In: *Physical Review B* 87.20 (May 24, 2013), p. 205435. ISSN: 1098-0121, 1550-235X. DOI: 10.1103/PhysRevB.87.205435.

[57] Patryk Kusch, Steffen Breuer, Manfred Ramsteiner, Lutz Geelhaar, Henning Riechert, and Stephanie Reich. "Band gap of wurtzite GaAs: A resonant Raman study." In: *Physical Review B* 86.7 (Aug. 24, 2012), p. 075317. ISSN: 1098-0121, 1550-235X. DOI: 10.1103/PhysRevB.86.075317.

[58] Hans Kuzmany. *Solid-State Spectroscopy: An Introduction*. Berlin, Heidelberg: Springer Berlin Heidelberg, 2009. ISBN: 978-3-642-01478-9 978-3-642-01479-6. DOI: 10.1007/978-3-642-01479-6.

[59] Kyoung E. Kweon, Gyeong S. Hwang, Jinhan Kim, Sungjin Kim, and SeongMin Kim. "Electron small polarons and their transport in bismuth vanadate: a first principles study." In: *Physical Chemistry Chemical Physics* 17.1 (2015), pp. 256–260. ISSN: 1463-9076, 1463-9084. DOI: 10.1039/C4CP03666B.

[60] L. Lindsay, D. A. Broido, and T. L. Reinecke. "*Ab initio* thermal transport in compound semiconductors." In: *Physical Review B* 87.16 (Apr. 2, 2013), p. 165201. ISSN: 1098-0121, 1550-235X. DOI: 10.1103/PhysRevB.87.165201.

[61] Ming S. Liu, Les A. Bursill, S. Prawer, and R. Beserman. "Temperature dependence of the first-order Raman phonon line of diamond." In: *Physical Review B* 61.5 (Feb. 1, 2000), pp. 3391–3395. ISSN: 0163-1829, 1095-3795. DOI: 10.1103/PhysRevB.61.3391.

[62] R. P. Lowndes, N. E. Tornberg, and R. C. Leung. "Ferroelectric mode and molecular structure in the hydrogen-bonded ferroelectric arsenates and their deuterated isomorphs." In: *Physical Review B* 10.3 (Aug. 1, 1974), pp. 911–931. ISSN: 0556-2805. DOI: 10.1103/PhysRevB.10.911.

[63] Hongmei Luo, Alex H. Mueller, T. Mark McCleskey, Anthony K. Burrell, Eve Bauer, and Q. X. Jia. "Structural and Photoelectrochemical Properties of $BiVO_4$ Thin Films." In: *The Journal of Physical Chemistry C* 112.15 (Apr. 2008), pp. 6099–6102. ISSN: 1932-7447, 1932-7455. DOI: 10.1021/jp7113187.

[64] G. G. Macfarlane and V. Roberts. "Infrared Absorption of Germanium near the Lattice Edge." In: *Physical Review* 97.6 (Mar. 1955), pp. 1714–1716. ISSN: 0031-899X. DOI: 10.1103/PhysRev.97.1714.2.

[65] V. Mazzacurati, G. Signorelli, and M. Sampoli. "Indirect coupling of the soft optic phonon in KH_2PO_4." In: *Journal of Raman Spectroscopy* 4.4 (Apr. 1976), pp. 339–352. ISSN: 03770486. DOI: 10.1002/jrs.1250040402.

[66] Henrique P. C. Miranda, Sven Reichardt, Guillaume Froehlicher, Alejandro Molina-Sánchez, Stéphane Berciaud, and Ludger Wirtz. "Quantum interference effects in resonant Raman spectroscopy of single- and triple-layer $MoTe_2$ from first principles." In: *Nano Letters* 17.4 (Apr. 12, 2017), pp. 2381–2388. ISSN: 1530-6984, 1530-6992. DOI: 10.1021/acs.nanolett.6b05345. arXiv: 1702.05461[cond-mat].

[67] N.F. Mott and E.A. Davis. *Electronic processes in non-crystalline materials*. Oxford University Press, 2012. ISBN: 9780191023286.

[68] Donald A. Neamen. *Semiconductor physics and devices : basic principles*. 4th ed. New York: McGraw-Hill Education, 2012. ISBN: 978-0-07-108902-9.

[69] Jacques I. Pankove. *Optical Processes in Semiconductors*. Dover Publications, 2012. ISBN: 1306351936.

[70] Biljana Pejova, Bahattin Abay, and Irina Bineva. "Temperature Dependence of the Band-Gap Energy and Sub-Band-Gap Absorption Tails in Strongly Quantized ZnSe Nanocrystals Deposited as Thin Films." In: *The Journal of Physical Chemistry C* 114.36 (Sept. 16, 2010), pp. 15280–15291. ISSN: 1932-7447, 1932-7455. DOI: 10.1021/jp102773z.

[71] J. Pellicer-Porres, D. Vázquez-Socorro, S. López-Moreno, A. Muñoz, P. Rodríguez-Hernández, D. Martínez-García, S. N. Achary, A. J. E. Rettie, and C. Buddie Mullins. "Phase transition systematics in $BiVO_4$ by means of high-pressure–high-temperature Raman experiments." In: *Physical Review B* 98.21 (Dec. 2018), p. 214109. ISSN: 2469-9950, 2469-9969. DOI: 10.1103/PhysRevB.98.214109.

[72] M. A. Pimenta, A. Marucci, S. A. Empedocles, M. G. Bawendi, E. B. Hanlon, A. M. Rao, P. C. Eklund, R. E. Smalley, G. Dresselhaus, and M. S. Dresselhaus. "Raman modes of metallic carbon nanotubes." In: *Physical Review B* 58.24 (Dec. 15, 1998), R16016–R16019. ISSN: 0163-1829, 1095-3795. DOI: 10.1103/PhysRevB.58.R16016.

[73] A. Pinczuk, Gerald Burns, and F.H. Dacol. "Soft optical phonon in ferroelastic $BiVO_4$." In: *Solid State Communications* 24.2 (Oct. 1977), pp. 163–165. ISSN: 00381098. DOI: 10.1016/0038-1098(77)90598-1.

[74] A. M. Rao et al. "Diameter-Selective Raman Scattering from Vibrational Modes in Carbon Nanotubes." In: *Science* 275.5297 (Jan. 10, 1997), pp. 187–191. ISSN: 0036-8075, 1095-9203. DOI: 10.1126/science.275.5297.187.

[75] Sven Reichardt and Ludger Wirtz. "Nonadiabatic exciton-phonon coupling in Raman spectroscopy of layered materials." In: *Science Advances* 6.32 (Aug. 7, 2020), eabb5915. ISSN: 2375-2548. DOI: 10.1126/sciadv.abb5915.

[76] J. B. Renucci, R. N. Tyte, and M. Cardona. "Resonant Raman scattering in silicon." In: *Physical Review B* 11.10 (May 15, 1975), pp. 3885–3895. ISSN: 0556-2805. DOI: 10.1103/PhysRevB.11.3885.

[77] M. A. Renucci, J. B. Renucci, R. Zeyher, and M. Cardona. "Second-order Raman scattering in germanium in the vicinity of the E_1 , E_1 + $_1$ edges." In: *Physical Review B* 10.10 (Nov. 15, 1974), pp. 4309–4323. ISSN: 0556-2805. DOI: 10.1103/PhysRevB.10.4309.

[78] M. A. Reshchikov, D. O. Demchenko, J. D. McNamara, S. Fernández-Garrido, and R. Calarco. "Green luminescence in Mg-doped GaN." In: *Physical Review B* 90.3 (July 21, 2014), p. 035207. ISSN: 1098-0121, 1550-235X. DOI: 10.1103/PhysRevB.90.035207.

[79] M. A. Reshchikov, J. D. McNamara, F. Zhang, M. Monavarian, A. Usikov, H. Helava, Yu. Makarov, and H. Morkoç. "Zero-phonon line and fine structure of the yellow luminescence band in GaN." In: *Physical Review B* 94.3 (July 5, 2016), p. 035201. ISSN: 2469-9950, 2469-9969. DOI: 10.1103/PhysRevB.94.035201.

[80] Michael A. Reshchikov and Hadis Morkoç. "Luminescence properties of defects in GaN." In: *Journal of Applied Physics* 97.6 (Mar. 15, 2005), p. 061301. ISSN: 0021-8979, 1089-7550. DOI: 10.1063/1.1868059.

[81] Alexander J. E. Rettie, William D. Chemelewski, David Emin, and C. Buddie Mullins. "Unravelling Small-Polaron Transport in Metal Oxide Photoelectrodes." In: *The Journal of Physical Chemistry Letters* 7.3 (Feb. 4, 2016), pp. 471–479. ISSN: 1948-7185, 1948-7185. DOI: 10.1021/acs.jpclett.5b02143.

[82] Alexander J. E. Rettie, William D. Chemelewski, Jeffrey Lindemuth, John S. McCloy, Luke G. Marshall, Jianshi Zhou, David Emin, and C. Buddie Mullins. "Anisotropic small-polaron hopping in W:$BiVO_4$ single crystals." In: *Applied Physics Letters* 106.2 (Jan. 12, 2015), p. 022106. ISSN: 0003-6951, 1077-3118. DOI: 10.1063/1.4905786.

[83] Alexander J. E. Rettie, Heung Chan Lee, Luke G. Marshall, Jung-Fu Lin, Cigdem Capan, Jeffrey Lindemuth, John S. McCloy, Jianshi Zhou, Allen J. Bard, and C. Buddie Mullins. "Combined Charge Carrier Transport and Photoelectrochemical Characterization of BiVO $_4$ Single Crystals: Intrinsic Behavior of a Complex Metal Oxide." In: *Journal of the American Chemical Society* 135.30 (July 31, 2013), pp. 11389–11396. ISSN: 0002-7863, 1520-5126. DOI: 10.1021/ja405550k.

[84] Ulrich Rössler. *Solid State Theory: An Introduction*. Berlin, Heidelberg: Springer Berlin Heidelberg, 2009. ISBN: 978-3-540-93785-2 978-3-540-92762-4. DOI: 10.1007/978-3-540-92762-4.

[85] E. K. H. Salje, B. Wruck, and H. Thomas. "Order-parameter saturation and low-temperature extension of Landau theory." In: *Zeitschrift für Physik B Condensed Matter* 82.3 (Oct. 1991), pp. 399–404. ISSN: 0722-3277, 1434-6036. DOI: 10.1007/BF01357186.

[86] A. Scalabrin, A. S. Chaves, D. S. Shim, and S. P. S. Porto. "Temperature dependence of the A1 and E optical phonons in $BaTiO_3$." In: *Physica Status Solidi (b)* 79.2 (Feb. 1, 1977), pp. 731–742. ISSN: 03701972, 15213951. DOI: 10.1002/pssb.2220790240.

[87] M. A. F. Scarparo, R. S. Katiyar, R. Srivastava, and S. P. S. Porto. "Evidence of non-linear behaviour of soft modes in crystals with KDP structure." In: *Physica Status Solidi (b)* 90.2 (Dec. 1, 1978), pp. 543–556. ISSN: 03701972, 15213951. DOI: 10.1002/pssb.2220900213.

[88] C. Y. She, T. W. Broberg, L. S. Wall, and David F. Edwards. "Effect of Proton-Phonon Coupling on the Ferroelectric Mode in KH_2PO_4." In: *Physical Review B* 6.5 (Sept. 1, 1972), pp. 1847–1850. ISSN: 0556-2805. DOI: 10.1103/PhysRevB.6.1847.

[89] Susanne Siebentritt. "Shallow Defects in the Wide Gap Chalcopyrite $CuGaSe_2$." In: *Wide-Gap Chalcopyrites*. Ed. by Susanne Siebentritt and Uwe Rau. Red. by R. Hull, R.M Osgood, J. Parisi, and H. Warlimont. Vol. 86. Berlin, Heidelberg: Springer Berlin Heidelberg, 2006, pp. 113–156. ISBN: 978-3-540-24497-4 978-3-540-31293-2. DOI: 10.1007/3-540-31293-5_7.

[90] K. Sinha and J. Menéndez. "First- and second-order resonant Raman scattering in graphite." In: *Physical Review B* 41.15 (May 15, 1990), pp. 10845–10847. ISSN: 0163-1829, 1095-3795. DOI: 10.1103/PhysRevB.41.10845.

[91] J. G. Skinner and W. G. Nilsen. "Absolute Raman Scattering Cross-Section Measurement of the 992 cm^1 Line of Benzene*." In: *Journal of the Optical Society of America* 58.1 (Jan. 1, 1968), p. 113. ISSN: 0030-3941. DOI: 10.1364/JOSA.58.000113.

[92] A.W. Sleight, H.-y. Chen, A. Ferretti, and D.E. Cox. "Crystal growth and structure of $BiVO_4$." In: *Materials Research Bulletin* 14.12 (Dec. 1979), pp. 1571–1581. ISSN: 00255408. DOI: 10.1016/0025-5408(72)90227-9.

[93] S.A. Smee, J.D. Orndorff, G.A. Scharfstein, Y. Qiu, P.C. Brand, C.L. Broholm, and D.K. Anand. "MACS low-background doubly focusing neutron monochromator." In: *Applied Physics A: Materials Science & Processing* 74.0 (Dec. 1, 2002), s255–s257. ISSN: 0947-8396, 1432-0630. DOI: 10.1007/s003390201658.

[94] Conrad Spindler. "Optical Detection pf Deep Defects in $Cu(In,Ga)Se_2$." Dissertation. University Luxembourg, June 7, 2018.

[95] Aaron L. Stancik and Eric B. Brauns. "A simple asymmetric lineshape for fitting infrared absorption spectra." In: *Vibrational Spectroscopy* 47.1 (May 2008), pp. 66–69. ISSN: 09242031. DOI: 10.1016/j.vibspec.2008.02.009.

[96] S. Stoughton et al. "Adsorption-controlled growth of $BiVO_4$ by molecular-beam epitaxy." In: *APL Materials* 1.4 (Oct. 2013), p. 042112. ISSN: 2166-532X. DOI: 10.1063/1.4824041.

[97] U. Stuhr et al. "The thermal triple-axis-spectrometer EIGER at the continuous spallation source SINQ." In: *Nuclear Instruments and Methods in Physics Research Section A: Accelerators, Spectrometers, Detectors and Associated Equipment* 853 (May 2017), pp. 16–19. ISSN: 01689002. DOI: 10.1016/j.nima.2017.02.003.

[98] Yasunari Takagi. "Coupled modes analysis of raman spectra: Application to the case of a KH_2PO_4 crystal in the paraelectric phase." In: *Ferroelectrics* 46.1 (Feb. 1983), pp. 245–259. ISSN: 0015-0193, 1563-5112. DOI: 10.1080/00150198308225271.

[99] J. Tauc, R. Grigorovici, and A. Vancu. "Optical Properties and Electronic Structure of Amorphous Germanium." In: *physica status solidi (b)* 15.2 (1966), pp. 627–637. ISSN: 03701972, 15213951. DOI: 10.1002/pssb.19660150224.

[100] Saimi Tokunaga, Hideki Kato, and Akihiko Kudo. "Selective Preparation of Monoclinic and Tetragonal $BiVO_4$ with Scheelite Structure and Their Photocatalytic Properties." In: *Chemistry of Materials* 13.12 (Dec. 2001), pp. 4624–4628. ISSN: 0897-4756, 1520-5002. DOI: 10.1021/cm0103390.

[101] Izumi Tomeno, Naomi Sato, Yoshinosuke Sato, Kunihiko Oka, and Yorihiko Tsunoda. "Neutron scattering study of acoustic phonon softening in $BiVO_4$." In: *Physical Review B* 84.1 (July 12, 2011), p. 014302. ISSN: 1098-0121, 1550-235X. DOI: 10.1103/PhysRevB.84.014302.

[102] R. Trommer and M. Cardona. "Resonant Raman scattering in GaAs." In: *Physical Review B* 17.4 (Feb. 15, 1978), pp. 1865–1876. ISSN: 0163-1829. DOI: 10.1103/PhysRevB.17.1865.

[103] I. A. Vainshtein, A. F. Zatsepin, and V. S. Kortov. "Applicability of the empirical Varshni relation for the temperature dependence of the width of the band gap." In: *Physics of the Solid State* 41.6 (June 1999), pp. 905–908. ISSN: 1063-7834, 1090-6460. DOI: 10.1134/1.1130901.

[104] Y. P. Varshni. "TEMPERATURE DEPENDENCE OF THE ENERGY GAP IN SEMICONDUCTORS." In: *Physica* 34.1 (1967), pp. 149–154. ISSN: 0031-8914. DOI: https://doi.org/10.1016/0031-8914(67)90062-6.

[105] Michael James Ventura. "Fabrication and characterisation of three-dimensional passive and active photonic crystals." dissertation. Swinburne University of Technology, 2008. URL: http://hdl.handle.net/1959.3/35914 (visited on 03/10/2023).

[106] D. Vincent. *DFT Calculation of lattice vibrations in $BiVO_4$ using hybrid functions*. unpublished work. University Rennes. 2023.

[107] N. Wada and S.A. Solin. "Raman efficiency measurements of graphite." In: *Physica B+C* 105.1 (May 1981), pp. 353–356. ISSN: 03784363. DOI: 10.1016/0378-4363(81)90274-6.

[108] Nitin Wadnerkar and Niall J. English. "Density functional theory investigations of bismuth vanadate: Effect of hybrid functionals." In: *Computational Materials Science* 74 (June 2013), pp. 33–39. ISSN: 09270256. DOI: 10.1016/j.commatsci.2013.03.015.

[109] Aron Walsh, Yanfa Yan, Muhammad N. Huda, Mowafak M. Al-Jassim, and Su-Huai Wei. "Band Edge Electronic Structure of $BiVO_4$: Elucidating the Role of the Bi s and V d Orbitals." In: *Chemistry of Materials* 21.3 (Feb. 2009), pp. 547–551. ISSN: 0897-4756, 1520-5002. DOI: 10.1021/cm802894z.

[110] Mads Christof Weber, Mael Guennou, Constance Toulouse, Maximilien Cazayous, Yannick Gillet, Xavier Gonze, and Jens Kreisel. "Temperature evolution of the band gap in $BiFeO_3$ traced by resonant Raman scattering." In: *Physical Review B* 93.12 (Mar. 7, 2016). ISSN: 2469-9950, 2469-9969. DOI: 10.1103/PhysRevB.93.125204.

[111] B. A. Weinstein and Manuel Cardona. "Resonant First- and Second-Order Raman Scattering in GaP." In: *Physical Review B* 8.6 (Sept. 15, 1973), pp. 2795–2809. ISSN: 0556-2805. DOI: 10.1103/PhysRevB.8.2795.

[112] I G Wood. "Spontaneous birefringence of ferroelastic $BiVO_4$ and $LaNBO_4$ between 10K and T_c." In: *Journal of Physics C: Solid State Physics* 17.21 (July 30, 1984), pp. L539–L543. ISSN: 0022-3719. DOI: 10.1088/0022-3719/17/21/003.

[113] I. G. Wood, B. Welber, W. I. F. David, and A. M. Glazer. "Ferroelastic phase transition in $BiVO_4$ II. Birefringence at simultaneous high pressure and temperature." In: *Journal of Applied Crystallography* 13.3 (June 1980), pp. 224–229. ISSN: 0021-8898. DOI: 10.1107/S0021889880011971.

[114] H. Yokota, N. Hasegawa, M. Glazer, E. K. H. Salje, and Y. Uesu. "Direct evidence of polar ferroelastic domain boundaries in semiconductor $BiVO_4$." In: *Applied Physics Letters* 116.23 (June 8, 2020), p. 232901. ISSN: 0003-6951, 1077-3118. DOI: 10.1063/5.0010414.

[115] Peter Y. Yu and Manuel Cardona. *Fundamentals of semiconductors: physics and materials properties ; with 52 tables and 116 problems*. 3., rev. and enl. ed., 3., corr. print. Berlin: Springer, 2005. 639 pp. ISBN: 978-3-540-25470-6.

[116] Xi Zhang, Zhihui Ai, Falong Jia, Lizhi Zhang, Xiaoxing Fan, and Zhigang Zou. "Selective synthesis and visible-light photocatalytic activities of $BiVO_4$ with different crystalline phases." In: *Materials Chemistry and Physics* 103.1 (May 2007), pp. 162–167. ISSN: 02540584. DOI: 10.1016/j.matchemphys.2007.02.008.

[117] Zongyan Zhao, Zhaosheng Li, and Zhigang Zou. "Electronic structure and optical properties of monoclinic clinobisvanite $BiVO_4$." In: *Physical Chemistry Chemical Physics* 13.10 (2011), p. 4746. ISSN: 1463-9076, 1463-9084. DOI: 10.1039/c0cp01871f.

[118] Bin Zhou, Jiuhui Qu, Xu Zhao, and Huijuan Liu. "Fabrication and photoelectrocatalytic properties of nanocrystalline monoclinic $BiVO_4$ thin-film electrode." In: *Journal of Environmental Sciences* 23.1 (Jan. 2011), pp. 151–159. ISSN: 10010742. DOI: 10.1016/S1001-0742(10)60387-7.

[119] Ke-Rong Zhu, Ming-Sheng Zhang, Qiang Chen, and Zhen Yin. "Size and phonon-confinement effects on low-frequency Raman mode of anatase TiO_2 nanocrystal." In: *Physics Letters A* 340.1 (June 2005), pp. 220–227. ISSN: 03759601. DOI: 10.1016/j.physleta.2005.04.008.